

**DEVELOPMENT OF  ${}^7\text{Li}(p,n){}^7\text{Be}$  NEUTRON ENERGY SPECTRUM  
CODE AND MEASUREMENT OF NEUTRON RADIATIVE CAPTURE  
CROSS-SECTION ON FEW STRUCTURAL ELEMENTS IN THE keV  
NEUTRON ENERGY REGION**

**A Thesis submitted  
in fulfillment for the requirements of the  
Degree of Doctor of Philosophy in Physics  
under Mizoram University, Aizawl**

**By**

**Rebecca Lalnuntluangi**

**Reg. No.: MZU/Ph.D./691 of 20.10.2014**

**To**



**SCHOOL OF PHYSICAL SCIENCES  
DEPARTMENT OF PHYSICS**

**MIZORAM UNIVERSITY**

**TANHRIL-796004**

Dr. LalremruataBawitlung  
Assistant Professor  
Department of Physics  
Mizoram University  
Tanhril-796004  
Aizawl, Mizoram



**MIZORAM UNIVERSITY**  
**DEPARTMENT OF PHYSICS**  
**AIZAWL 796 004 MIZORAM**  
Phones: 0389 - 2330522  
FAX : 0389 - 2330522  
Mobile: +919436779952  
E-mail: [marema08@gmail.com](mailto:marema08@gmail.com)

(A Central University Established by an Act of Parliament)

Date: 3<sup>rd</sup> December, 2018

## Certificate

This is to certify that the thesis entitled “*Development of  ${}^7\text{Li}(p,n){}^7\text{Be}$  neutron energy spectrum code and measurement of neutron radiative capture cross-section on few structural elements in the keV neutron energy region*” submitted by Ms. Rebecca Lalnuntluangi, for the degree of Doctor of Philosophy in Physics, of the Mizoram University: Aizawl, India, embodies the record of original investigations carried out by her under my supervision. She has been duly registered and the thesis presented is worthy of being considered for the award of Ph.D. degree. This research work has not been submitted for any degree of any other university.

(Dr. B. LALREMRUATA)

Supervisor

**Declaration**  
**Mizoram University**  
**December 2018**

*I, Rebecca Lalnuntluangi, a Ph.D scholar in Physics Department, Mizoram University, do hereby solemnly declare that the subject matter of this thesis is the record of work done by me, that the contents of this thesis did not form basis of the award of any previous degree to me or to the best of my knowledge to anybody else, and that the thesis has not been submitted by me for any research degree in any other University/Institute.*

*This thesis is being submitted to Mizoram University for the degree of Doctor of Philosophy in Physics.*

**(REBECCA LALNUNTLUANGI)**

**Candidate**

**(Prof. SUMAN RAI)**

**Head**

**(Dr. B. LALREMRUATA)**

**Supervisor**

## Acknowledgement

After an intensive study of more than four and a half years, I finally reached the finishing touch of my Ph.D dissertation. I would like to express my sincere gratitude to all those who helped me throughout the whole period of my research.

First of all, I would like to thank my supervisor **Dr. B. Lalremruata** for giving me the opportunity to complete my Ph.D research work under his supervision; without which I would not have completed this challenging research work. Thank you for giving me an opportunity to explore the world of Nuclear Physics and meet people I would have never come across in my life; I treasure the experience and discussions in the forum. I also appreciate his devotion, ever helping hand, technical inputs and knowledge shared with me, which will always have a big impact in my future career.

I also would like to extend my special thanks to the faculty of the Department of Physics, Mizoram University for their kind valuable help at various phases of my research. I express my sincere thanks to **Prof. Zaithanzauva Pachuau** (DEAN, SPS), **Prof. R.C. Tiwari**, **Prof. Suman Rai** (Head, Department of Physics), **Prof. R.K. Thapa**, **Dr. Hranghmingthanga** and **Dr. Lalthakimi Zadeng** for their encouraging words and support extended towards me. My heartfelt thanks also go to all the non-teaching staff of the Department of Physics, **U Nunpuui**, **U Mala**, **Pu Ngaia** and **U Luri**.

My acknowledgement will never be completed without special mention to my lab mates, **U Mamawia**, **Remruata** and **J-i** for their kind support. We were not only able to support each other by deliberating over our problems and findings, but also happily talking about things other than just our works. Indeed, we have created one new family in our

department. I would also like to thank the new members of our **NHERG** family, **Samuela, BT-a** and **Ramnghaka**. I cherish each and every moment I spent with them. My sincere gratitude also goes to **Dr. Sangtea, Tluangi, Rindiki, Maruati, Matlani, Biaka, Chhana, Chda** and **Matluanga** for their kind support and prayers.

I am extremely thankful to my family, who meant the world to me. I treasured the support, prayers, endless love, encouragement and help rendered to me in every phase of my personal and academic life without which the completion of my work would not have been possible. I give thanks to my dearest **Granny, Mom** and **Dad**, who were always there for me. I would also like to thank my sisters, **Mary** and **Ruth**, and my one and only brother **Joseph** for all the love and supports he had shown upon me. I consider myself the luckiest to have such an understanding and supportive family.

Most importantly, I would like to thank **Almighty God** for giving me good health and strength to be able to complete my research work on time.

Dated: 3<sup>rd</sup> December, 2018

Mizoram University

(Rebecca Lalnuntluangi)

Department of Physics

Mizoram University

Aizawl, Mizoram

# Contents

Title of the Thesis	i
Certificate	ii
Declaration	iii
Acknowledgement	iv-v
Contents	vi-viii
List of Figures	x-xii
List of Tables	xiii-xiv
Dedication	xv
CHAPTER 1: INTRODUCTION	1-22
1.1. Nuclear Data	1-3
1.1.1. Nuclear Structure and Decay Data	1-2
1.1.2. Nuclear Reaction Data	2-3
1.2. Nuclear Data Libraries	3-6
1.2.1. Experimental Data	4
1.2.2. Model Calculations	4
1.2.3. Nuclear Data Evaluation	5
1.2.4. Simulation Codes	5
1.2.5. Sensitivity Analysis	5-6
1.3. Covariance and its Significance in Nuclear Data Measurement	7
1.5. Neutron Energy Spectrum Code-Energy of Proton	
Energy of Neutron (EPEN)	7-8
1.4. Scope of Present Research Work	8-11

1.6. Neutron Activation Analysis	11-17
1.6.1. Fundamental Equations in Neutron Activation Analysis	14-17
1.7. Review of Literature	17-22
CHAPTER 2: NEUTRON ENERGY SPECTRUM CODE-EPEN	23-51
2.1. ${}^7\text{Li}(p,n){}^7\text{Be}$ reaction as neutron source	23-24
2.2. Importance of the work	25-26
2.3. Formalism for Calculating the Neutron Energy Spectrum	26-38
2.3.1. Nuclear Reaction Kinematics	27-31
2.3.2. Laboratory Differential Cross Sections for Proton Energies Above 1.95 MeV	31-32
2.3.3. Near Threshold Kinematics	32-35
2.3.4. Angular Differential Cross Section	35-36
2.3.5. Angular Integration	36
2.3.6. Weighting Function $w_1(\theta)$	36-37
2.3.7. Weighting Function $w_2(E_p(\theta, E_n))$	37-38
2.4. Result and Discussion	38-51
2.4.1. Comparison with Experimental Neutron Spectra	38-45
2.4.2. Comparison with SimLiT and PINO	45-51
CHAPTER 3: EXPERIMENTAL DETAILS	52-68
3.1. Neutron Source	52-55
3.2. Sample Preparation	55-56
3.3. Measurement of $\gamma$ -ray Activity	57-58
3.4. Calibration of HPGe Detector	59-63
3.4.1. Intrinsic Efficiency	61-62
3.4.2. Geometric efficiency	62-63

3.5. Coincidence Summing Effect	63-68
3.5.1. Software for Correction of TCS (EFFTRAN)	67-68
CHAPTER 4: DATA ANALYSIS PROCEDURE	69-94
4.1. Estimation of Measured Cross Section	69
4.2. Reference Cross Section	69-70
4.3. Correction Factors	70-75
4.3.1. Neutron Flux Fluctuation Correction Factor	70-71
4.3.2. Low-Energy Neutron Backgrounds Correction Factor	71-72
4.3.3. Scattered Neutron Background Correction Factor	72-73
4.3.4. Gamma-Ray Self Attenuation Correction Factor	73-75
4.4. Uncertainty Propagation	76-87
4.4.1. Uncertainty in Detector Efficiency	76-79
4.4.2. Uncertainty in Standard Gold Monitor Cross Section	79-82
4.4.3. Uncertainty in Timing Factor $\Delta f_x/f_x$	82-86
4.4.4. Correlation Between Measured Cross Sections	86-87
4.5. Nuclear Models	87-94
4.5.1. Level Densities	87-93
4.5.2. Gamma-Ray Transmission Coefficients	93-94
CHAPTER 5: RESULTS AND DISCUSSIONS	95-100
CHAPTER 6: SUMMARY AND CONCLUSIONS	101-106
REFERENCES	107-116
APPENDIX	117-134
BIODATA	135
LIST OF RESEARCH PUBLICATIONS	136-137
CONFERENCES/WORKSHOPS ATTENDED	138
REPRINTS OF PUBLISHED PAPERS	



## List of Figures

Figure No.	Figure Captions	Page No.
1	Graphical representation of a nuclear data cycle.	6
2	Schematic diagram of s, r and p – processes nuclear reaction flow.	10
3	Diagram illustrating the process of neutron capture by a target nucleus followed by the emission of gamma rays.	13
4	Graph showing the activity build-up as the sample is irradiated.	16
5	Proton energy contours for the ${}^7\text{Li}(p,n_0){}^7\text{Be}$ reaction.	27
6	Schematic diagram of a nuclear reaction.	27
7	Comparison of EPEN ${}^7\text{Li}(p,n_0){}^7\text{Be}$ neutron energy spectrum at $E_p=1912 \pm 0$ keV with experimental results (Lederer et al., 2012; Ratynski et al., 1988; Feinberg et al., 2012) for a thick natural lithium target.	39
8	Comparison of EPEN ${}^7\text{Li}(p,n_0){}^7\text{Be}$ neutron $0^\circ$ double differential energy spectrum at $E_p=1940$ keV with experimental result (Kononov et al., 1977; Kononov, 2016) for a thick natural lithium target.	40
9	Comparison of EPEN ${}^7\text{Li}(p,n_0){}^7\text{Be}$ double differential neutron energy spectrum at $E_p=1940$ keV for various angular range with experimental result (Kononov et al., 1977; Kononov, 2016).	41
10	Comparison of EPEN ${}^7\text{Li}(p,n_0){}^7\text{Be}$ double differential neutron	42

	energy spectrum with experimental result (Feinberg, 2012) at $E_p=1912\pm 1.5$ keV at $0\pm 2.9^\circ$ for a thick natural lithium target.	
<b>11</b>	Comparison of differential neutron spectra of EPEN with experimental results of Lefevre and Din for (a) $E_p = 3450$ keV and (b) $E_p = 2520$ keV at $0 \pm 6$ deg for a thick LiF target. For comparison, the neutron spectra are normalized such that they have a common maximum 1.	<b>43-44</b>
<b>12</b>	Comparison of angle-integrated neutron spectrum of EPEN with theoretical results of Ritchie at (a) $E_p = 2400$ keV and (b) $E_p = 2800$ keV for a thick natural lithium target. In (a), the $(p,n_1)$ neutron spectra of Ritchie and EPEN are multiplied by 30 for better visibility.	<b>44-45</b>
<b>13</b>	Comparison between EPEN, SimLiT and PINO neutron energy spectra for thin lithium target thickness $38 \mu\text{m}$ at (a) $E_p = 2800\pm 20$ keV and (b) $E_p = 3500\pm 20$ keV.	<b>47</b>
<b>14</b>	Comparison between EPEN, SimLiT and PINO neutron energy spectra for thin lithium target thickness $60 \mu\text{m}$ at (a) $E_p = 2800\pm 20$ keV and (b) $E_p = 3500\pm 20$ keV.	<b>48-49</b>
<b>15</b>	Comparison between EPEN, SimLiT and PINO $(p,n_0)$ neutron energy spectra for zero proton beam energy spread at (a) $E_p = 2800$ keV and thin lithium target thickness $38 \mu\text{m}$ , (b) $E_p = 3500$ keV and thin lithium target thickness $38 \mu\text{m}$ , (c) $E_p = 2800$ keV and thin lithium target thickness $60 \mu\text{m}$ (d) $E_p = 3500$ keV and thin lithium target thickness $60 \mu\text{m}$ . SimLiT always requires	<b>49-51</b>

	finite proton energy spread, and we set it to 0.1 keV instead of 0 keV.	
<b>16</b>	The schematic diagram of the Experimental Setup.	<b>53</b>
<b>17</b>	NE213 neutron detector at zero degree kept at 1 m distance from the lithium target.	<b>53</b>
<b>18</b>	Neutron flux energy spectrum $\phi(E)$ from the ${}^7\text{Li}(p,n_0){}^7\text{Be}$ reaction at $E_p = 2.25 \pm 0.02\text{MeV}$ obtained from the code EPEN.	<b>54</b>
<b>19</b>	Neutron flux energy spectrum $\phi(E)$ from the ${}^7\text{Li}(p,n_0){}^7\text{Be}$ and ${}^7\text{Li}(p,n_1){}^7\text{Be}$ reaction at $E_p = 2.60 \pm 0.02\text{keV}$ obtained from the code EPEN.	<b>55</b>
<b>20</b>	Typical $\gamma$ -ray spectrum of radioactive nuclides ${}^{115}\text{In}^m$ , ${}^{71}\text{Zn}^m$ and ${}^{198}\text{Au}$ at $\langle E_n \rangle = 2.6\text{ MeV}$ .	<b>58</b>
<b>21</b>	Geometric arrangement of ${}^{152}\text{Eu}$ point source.	<b>62</b>
<b>22</b>	Simplified decay scheme for ${}^{152}\text{Eu}$ .	<b>64</b>
<b>23</b>	Sum peaks in the ${}^{152}\text{Eu}$ standard source spectrum due to coincidence summing.	<b>65</b>
<b>24</b>	Example of cascade decay scheme. Coincident emission of the photons (i-j), (k-m), (k-j) and (m-j).	<b>66</b>
<b>25</b>	Detection efficiency calibration curve of the HPGe detector for the $(1 \times 1)\text{-cm}^2$ source placed at a distance of 1 cm from the detector. The error bar for the uncertainty due to counting statistics is within the symbol.	<b>77</b>
<b>26</b>	Excitation functions of the ${}^{70}\text{Zn}(n,\gamma){}^{71}\text{Zn}^m$ cross sections measured in this paper, evaluated in TENDL-2015 (solid line) as well as	<b>96-98</b>

	<p>calculated by TALYS-1.8 with eight different Photon Strength Functions (PSF-1 to PSF-8) with the Level Density Models: (a) LDM-1 (b) LDM-2, (c) LDM-3, (d) LDM-4, (e) LDM-5 and (f) LDM-6. The experimental cross sections are (p,n<sub>0</sub>) neutron flux energy spectrum averaged, whereas the evaluated and calculated cross sections are for monoenergetic neutrons.</p>	
27	<p>Comparison between predictions of <math>^{70}\text{Zn}(n,\gamma)^{71}\text{Zn}^m</math> reaction cross sections at neutron energies 0.40, 0.70, 0.96 and 1.69 MeV by TALYS-1.6 and TALYS-1.8 with two different Photon Strength Functions (PSF-3 and PSF-4) and the Level Density Model 3 (LDM-3) respectively.</p>	100

## List of Tables

<b>Table No.</b>	<b>Table Captions</b>	<b>Page No.</b>
<b>1</b>	Representation of ${}^7\text{Li}(p,n){}^7\text{Be}$ reaction Q-value and Threshold.	<b>24</b>
<b>2</b>	Details of foils used in the present experiment.	<b>56</b>
<b>3</b>	Decay data adopted in the present work taken from the ENSDF library.	<b>57</b>
<b>4</b>	Irradiation, cooling and counting times.	<b>58</b>
<b>5</b>	Characteristics of the ${}^{152}\text{Eu}$ point source.	<b>60</b>
<b>6</b>	Combinations of gamma-ray energies (keV) of the ${}^{152}\text{Eu}$ standard source that undergo coincidence summing. The yellow boxes indicate those peaks that undergo summing in and those blue boxes, summing out.	<b>66</b>
<b>7</b>	Detection efficiencies for the point source geometry $\varepsilon_p$ and for the foil stack geometry $\varepsilon$ at the characteristic $\gamma$ energies of ${}^{152}\text{Eu}$ with their $\gamma$ intensities $I_\gamma$ (Martin, 2013) adopted for efficiency determination, counts C and coincidence summing effect correction factors $K_c$ . The 444.0 keV $\gamma$ -line consists of 443.96 keV ( $I_\gamma = 2.827 \pm 0.014\%$ ) and 444.01 keV ( $I_\gamma = 0.298 \pm 0.011\%$ ) unresolved by our detector. The uncertainty in $\varepsilon$ is propagated from the uncertainties in C and $I_\gamma$ .	<b>68</b>
<b>8</b>	Correction factors applied to the measured cross sections.	<b>75</b>
<b>9</b>	The efficiency curve fitting parameter values.	<b>77</b>
<b>10</b>	The uncertainties $\Delta\varepsilon$ propagated from the C, $\Delta C$ , $I_\gamma$ , $\Delta I_\gamma$ , $\varepsilon_p$ , and $\varepsilon$ .	<b>78</b>

<b>11</b>	Spectrum averaged monitor cross section, its uncertainty and correlation coefficients.	<b>82</b>
<b>12</b>	Decay data adopted for calculation of timing factor taken from the ENSDF library.	<b>84</b>
<b>13</b>	(a): Calculation of timing factor for $^{71}\text{Zn}^m$ at $E_p = 2.6$ MeV. (b): Calculation of timing factor for $^{198}\text{Au}$ at $E_p = 2.6$ MeV.	<b>84-85</b>
<b>14</b>	(a): Calculation of timing factor for $^{71}\text{Zn}^m$ at $E_p = 2.25$ MeV. (b): Calculation of timing factor for $^{198}\text{Au}$ at $E_p = 2.25$ MeV.	<b>85-86</b>
<b>15</b>	Fractional uncertainties (%) in various parameters to obtain the $^{70}\text{Zn}(n,\gamma)^{71}\text{Zn}^m$ cross section.	<b>87</b>
<b>16</b>	The $^{70}\text{Zn}(n,\gamma)^{71}\text{Zn}^m$ cross sections measured in the present experiment with their total uncertainties and their correlation coefficients.	<b>95</b>

# *Dedication*

*This work is dedicated to my Granny, Dad, Mom,  
Brother and Sisters.*

**CHAPTER – 1**  
**INTRODUCTION**



## 1.1. Nuclear Data

The term ‘nuclear data’ has a broad meaning which represents the quantitative results of scientific investigations of the nuclear properties of matter. It includes all data which describe either the properties of nuclei or their interactions. It involves production and description of the properties of atomic nuclei and the fundamental physical relationships thereby characterizing the physical processes underlying all nuclear technologies. In all branches of nuclear science and technology, nuclear data finds widespread use covering energy applications such as fission reactor design, nuclear safety, reactor monitoring, nuclear fuel cycles, accelerator driven systems etc. It also includes non-energy applications such as production of radioisotopes for medical and industrial applications, personnel dosimetry and radiation safety, cancer radiotherapy, radiation damage studies etc. along with basic research (e.g. nuclear astrophysics) and education. Generally, all the nuclear data can be grouped under three headings: nuclear structure data, nuclear decay data and nuclear reaction data.

### 1.1.1. Nuclear structure and decay data

The numerical data related to the nuclear structure and nuclear decay data are well documented by the major database Evaluated Nuclear Structure Data File (ENSDF) while related bibliographic data are contained in Nuclear Science References (NSR). Atomic and nuclear decay data encompass the information on half-life, total decay energies (Q-value), branching fractions (if more than one known decay mode),  $\alpha$ -particle energies and emission probabilities,  $\beta$ -particle energies, emission probabilities and transition types, gamma ray energies, emission probabilities and internal conversion coefficients, electron-capture and  $\beta^+$ -particle energies, transition/emission probabilities and transition type etc. Radioactive nuclides are generally prepared by means of either reactor irradiation or charged particle accelerator and controlled bombardment of carefully prepared targets. The radioactive decay

data find many practical applications in the calculation of total radioactivity, heat generation, transmutation products, etc. The recent enhancing application of radioactivity in medicine, especially in vivo diagnostic and therapeutic studies results in rising demands on accurate decay data obtained from accurate internal radiation dose calculation.

The nuclear structure data contains information on the properties of the excited states of the nuclei. Detail information on nuclear structure which covers all the discrete levels up to the continuum of the nucleus, and even beyond, is obtained through spectral studies on nuclear processes. Most of the decaying nuclei have energies about 3 MeV or somewhat higher as a result of which the nuclear levels populated in the decay product are mostly characterized up to excitation energies of 2–3 MeV. The in-beam gamma-ray spectroscopy following an  $(n,\gamma)$  reaction which can provide information on the level structure of the product nucleus up to about 8 MeV (Qaim, 2010).

#### 1.1.2. Nuclear reaction data

Nuclear reaction data have been a crucial resource in nuclear technology such as fission and fusion energy, safeguards, environmental monitoring, activation analysis of materials, dosimetry, radiation safety, radioisotope production, medicine, radiotherapy and medical diagnostics. It also finds tremendous applications in basic science such as nuclear physics, astrophysics, nuclear chemistry and earth science. Based on nuclear theory and phenomenology, various reaction models have been developed and they have been verified by experimental nuclear reaction data which are further utilized for the revision of evaluated nuclear reaction data (Ref. JKPS from phone). Various types of nuclear reaction data information are stored in EXFOR, CINDA and ENDF.

In contrast to nuclear structure and radioactive decay data, whose scope is generally limited up to excitation energies of  $\sim 10$  MeV, the nuclear reaction data cover a very broad

span of energies, extending from a few MeV up to the region of several GeV. The lower side of the energy scale is typical of neutrons encompassing cold, thermal and epithermal regions whose major applications are related to structural analysis of solids, quantitative determination of elements via activation analysis, and fission reactor technology. The neutron capture cross sections and fission yields are useful for production of radionuclides, especially for medical applications. The energy region from about 10 keV to a few MeV can be reached both by neutrons and charged particles, and it is particularly interesting for astrophysics and fusion research, especially with respect to the interactions of light charged particles. Neutrons up to 20 MeV have been extensively utilized in the development of work related to fast reactors and future fusion technology. With increasing energies, monoenergetic neutrons become rarer, so that work above 30 MeV is done mostly using charged particles or spectral neutrons (Qaim, 2010).

## 1.2. Nuclear data libraries

The importance of nuclear data in vast areas has direct impact in the development of standard nuclear data libraries for the collection and distribution of nuclear data on a world-wide scale. The issue has been identified and addressed by the International Network of Nuclear Reaction Data Centres (NRDC) under the coordination of IAEA Nuclear Data Section (NDS) at Vienna. NDS carries out IAEA activities concerning the development and dissemination of nuclear and atomic data for applications. NDS provides more than 100 data libraries which are freely available to all users all over the world. The development of nuclear database is a tedious task involving the following steps (Alhassan, 2015):

### 1.2.1. Experimental data

Experimental nuclear data are needed to validate and make necessary update in the existing theoretical nuclear reaction models. They are also required for nuclear data assimilation. Experimental data can be divided into differential and integral data.

i) Differential data measurement: These include the measurement of microscopic quantities such as cross sections, fission yields and angular distributions as a function of the energy of the incoming particle, e.g., neutron. They are measured at a large number of experimental facilities, such as accelerators, world-wide. These data are collected, compiled and stored in the EXFOR database. Very often, the measurements are compared with the theoretical model calculations (Koning and Mengoni, 2009).

ii) Integral data measurement (benchmarks): Integral data measurement includes the use of integral data obtained from microscopic quantities such as cross-sections, for testing and validating nuclear data libraries. They are used to measure macroscopic quantities such as flux or  $k_{\text{eff}}$ . The experiments are often referred to as benchmarking experiments and the data are usually copyrighted and are accessible to the organizations working with them.

### 1.2.2. Model calculations

Since it is impossible to construct nuclear database from experimental data alone, nuclear reaction codes such as TALYS (Koning *et al.*, 2008) and EMPIRE (Herman *et al.*, 2007) were implemented. They are used for providing data where experimental data are scarce or unavailable. The main advantage of using nuclear reaction models is that various partial cross sections can be automatically summed up to the total cross section leading to internal consistency within evaluated files.

### 1.2.3. Nuclear data evaluation

Nuclear data is a generic notion which comprises the physical properties related to nuclear structure and nuclear reactions. Sometimes the experimental data show discrepancy and often fail to cover wide range of energies for the various nuclear processes including the different nuclides. On the other hand, the theoretical models are evolving to generate completely reliable data. Thus, the inconsistent and incomplete experimental data are combined with the optimum theoretical data illustrating the experimental data for the complicated process of evaluation. The evaluated nuclear reaction data are complete providing a reliable set of data. They contain all reactions and cover all energy regions, even where experimental data are missing, insufficient or inconsistent with some other experimental data sets. However, the process of evaluation itself is a complicated and tedious process, resulting from a careful analysis of the available existing data. It includes interpretation and comparison of experimental and theoretical data, validation against the benchmark experiments, evaluation of statistical and systematic errors, analysis for internal consistency and uniformity with monitor cross-sections, etc. The output of the evaluation process is a single output file referred to as recommended data set for a particular nuclear process corresponding to an isotope (Gunsing *et al.*, 2015).

### 1.2.4. Simulation Codes

The evaluations which are used worldwide are approved by safety authority and nuclear industries and finally used in simulation codes for reactor design and safety assessment (Rochman and Koning, 2011).

### 1.2.5. Sensitivity Analysis

The sensitivity or uncertainty analysis of the evaluated data is the process of quantifying the relative importance of input variables to the system response. They are

extremely important as they serve as input for various applications. They usually mean determination of the fraction of variance in the response due to the variance in a particular input variable. There are a number of different approaches to this problem, varying in mathematical complexity and required computational effort, depending upon the type of information the analyst is attempting to generate. The sensitivity analysis of the nuclear data increases their quality and thus making them more reliable and efficient for further use. The sensitivity analysis of the nuclear data gives a measure of how the nuclear system parameters, especially in the case of reactors the parameters like  $k_{\text{eff}}$ , are sensitive to the data uncertainty (Salvatores *et al.*, 2007). The data thus generated after sensitivity analysis are highly recommended for the use for the integral measurements and reactor designs. The graphical representation of a nuclear data cycle is shown in Figure 1.

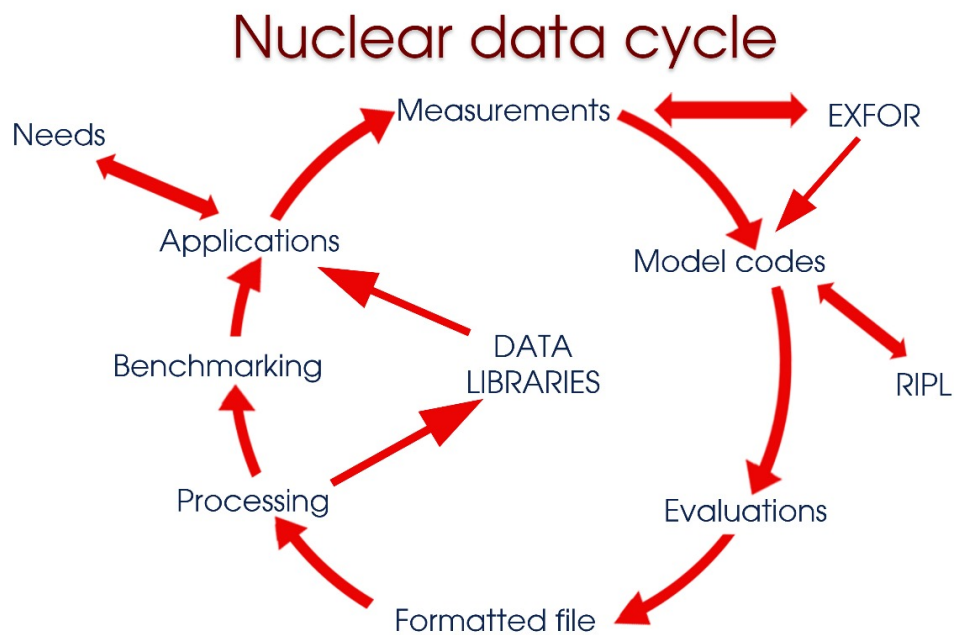


Figure 1: Graphical representation of a nuclear data cycle.

### 1.3. Covariance and its significance in nuclear data measurement

One of the major objectives in basic science is to provide reliable uncertainties on physical quantities which play an important part in the applied technology. The uncertainties of the experimental and evaluated nuclear data are found to be useful in the applications of nuclear data, e.g. for sensitivity and uncertainty analysis of reactor performance parameters in nuclear reactor physics. In fact, the evaluation of nuclear data highly improves after the introduction of the concept of covariance analysis. Therefore, in contemporary simulations, a major role is played by the uncertainty of nuclear data (Stanga and Muntele, 2000). The Nuclear Data Section of IAEA is also encouraging experimentalists to perform appropriate uncertainty propagation and its well documentation.

Furthermore, nuclear data are always inter-correlated to a certain degree, for instance cross section between different energies, different reactions, and even different materials. The uncertainties as a “sum of squares” is only true if the quantities involved are uncorrelated. Therefore, in order to propagate the uncertainty data correctly, the covariance matrix is required. The form of covariance depends on how it was produced. It is not measurable; so long as it’s mathematical form is correct, many versions of a covariance matrix are possible. To ensure consistent reactor calculations, it is of utmost importance to correctly estimate uncertainties and correlations of nuclear data (Gasper Zerovnik, 2012).

### 1.4. Neutron energy spectrum code-Energy of Proton Energy of Neutron (EPEN)

The  ${}^7\text{Li}(p,n){}^7\text{Be}$  reaction is widely used as quasi-monoenergetic neutron source because it can produce large amount of relatively low energy neutrons. In India, the 14 UD Pelletron Accelerator at the Tata Institute of Fundamental Research, Mumbai (BARC-TIFR Pelletron) and Folded Tandem Ion Accelerator at the Bhabha Atomic Research Centre (BARC-FOTIA) are currently the main accelerators serving as  ${}^7\text{Li}(p,n){}^7\text{Be}$  neutron sources

for neutron induced reaction cross-section measurements, and various activation cross-section measurements have been performed for neutron captures up to  $E_n \sim 17$  MeV with these neutron sources. The time-of-flight and multiple foil activation techniques cannot be applied at these accelerators due to the continuous beam structure and weak neutron flux. Therefore, experimentalists using these accelerators have to rely on calculated neutron energy spectra for subtraction of the  ${}^7\text{Li}(p,n){}^7\text{Be}$  contribution whose cross sections can be very pronounced as they have lower neutron energies. Therefore, we developed the nuclear reaction code-Energy of Proton Energy of Neutron (EPEN). The code was developed by using the  ${}^7\text{Li}(p,n){}^7\text{Be}$  reaction as neutron source. The code was initially designed up to 4 MeV but recently it had been extended to 7 MeV.

For proton energy greater than 7 MeV, the contribution due to three-body break up has become so pronounced that we do not find any evaluated data above this energy. For proton energies greater than 1.95 MeV, the evaluated data compiled by Liskien and Paulsen was adopted. For proton energies below 1.92 MeV, the neutron production is double valued i.e. for each angle of emission, there are two neutron energies. At these near threshold regions, we adopted the formulation prescribed by Macklin and Gibbons (Macklin *et al.*, 1958). The differential cross section between 1.92 and 1.95 MeV were obtained by using spline fitting interpolation.

### 1.5. Scope of present research work

The neutron-induced reactions on zinc isotope have many practical applications in biology and medicines, nuclear reactors and astrophysics. Stable zinc isotopes (atomic number  $Z = 30$  and mass numbers  $A = 64, 66, 67, 68,$  and  $70$ ) are located at the lower end of the distribution of fission products. At thermal neutron energy, the fractions of Zn isotopes to total fission yields are estimated to be less than 0.001%.



The cross sections for some neutron-induced reactions on zinc isotopes have a significant influence on various applications and basic science fields. The neutron cross sections of Zinc isotopes are needed for the design of fusion reactor and the evaluation of radiation damage in the structural materials of reactors. In various nuclear power plant systems, the radiation doses are increasing due to the accumulation of radioactive materials. Therefore, the necessity of reducing the operators' exposure to radiation has been increased. To reduce the radiation fields and corrosion in the primary system, zinc is injected into the reactor coolants. It has the characteristic of changing the ingredients of the corrosion oxide layers of the primary systems to a stable state by causing a discharge of the radioactive products such as Ni, Fe, Co, etc. that exist in the oxide layers. These radioactive products are substituted by zinc due to its high substitution energy. Therefore, the injection of a very small quantity of zinc not only reduces the radioactivity by removing the radioactive materials and formation of stable oxide layers, but also enhances the anti-corrosion properties of materials. To obtain such definite characteristics, a high concentration of zinc is applied for corrosion reduction and low concentration for radioactive reduction (EPRI, 2011).

$^{70}\text{Zn}$  is also one of the signatures of the s-process during shell carbon burning in massive stars. In the solar system, about half of the nuclei beyond iron are produced by the slow neutron capture process (s-process), the other half by the rapid neutron capture process (r-process), and a marginal contribution is provided by the so-called p-process (Burbidge *et al.*, 1957). The s-process path in the region around zinc starting from  $^{64}\text{Zn}$  is completely bypassing the r-only nucleus  $^{70}\text{Zn}$  which is produced when the  $^{69}\text{Zn}$  branching is open during the initial high neutron-density phase and during the final neutron burst (Reifarth *et al.*, 2012; Pignatari *et al.*, 2010). The s-process starting from  $^{70}\text{Zn}$  has contribution for the formation of  $^{71}\text{Ga}$  via  $^{71}\text{Zn}$  and hence,  $^{70}\text{Zn}(n,\gamma)$  reaction has linked the s-process path through  $^{71}\text{Ga}$ . Its

overabundance can also be used as an indicator of the strength of the nuclear reaction flow through the branchings along the s-process path (The L.S. *et al.*, 2007).

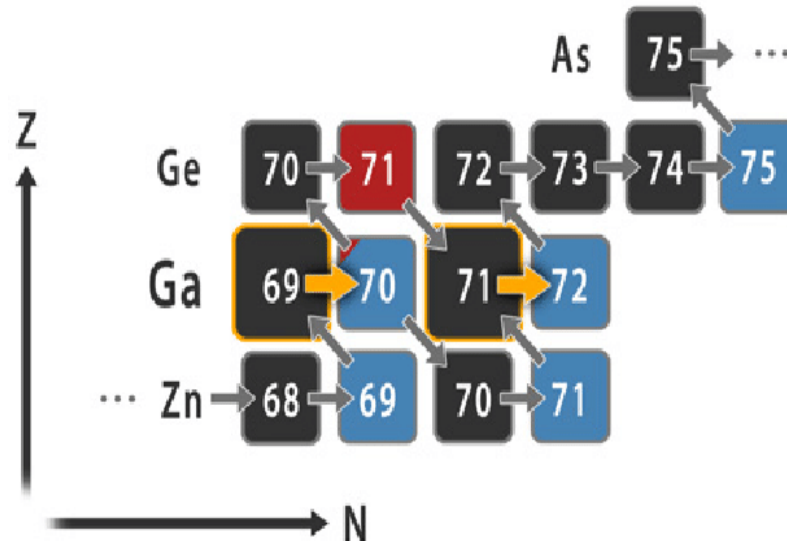


Figure 2: Schematic diagram of s, r and p – processes nuclear reaction flow.

When the incident neutron energy crosses the inelastic threshold energy (884.92 keV), the cross section decreases very rapidly. This is due to the  $^{70}\text{Zn}(n,n')^{70}\text{Zn}$  inelastic scattering channel. When the incident neutron energy crosses the inelastic threshold energy, the compound inelastic contribution rises rapidly and predominates, whereas the direct component increases more gradually. The decrease in the cross section is also predicted by TALYS-1.8 (Koning *et al.*, 2008) with different level-density models and gamma-ray strength functions. Therefore, the importance of nuclear data at this region motivated us to perform an experiment at neutron energies lower than the inelastic threshold energy.

Although the neutron induced reactions on  $^{70}\text{Zn}$  have many applications, the cross sections of  $^{70}\text{Zn}(n,\gamma)^{71}\text{Zn}^m$  at neutron energies 0.96 MeV and 1.69 MeV (Punte *et al.*, 2017; Otuka *et al.*, 2017) are the only available cross sections of the reaction in the MeV regions compiled in the EXFOR (Otuka *et al.*, 2014). Certain data are found at thermal neutron energy and at  $kT \sim 25$  keV performed by Reifarh *et al.* (2012). The small fraction of  $^{70}\text{Zn}$  abundance relative to other Zinc isotopes also makes it difficult to detect in the spectra of

stellar atmosphere or interstellar medium (The L. S. *et al.*, 2007). Hence, the present work aims at reporting new  $^{70}\text{Zn}(n,\gamma)^{71}\text{Zn}^m$  ( $3.96 \pm 0.05$  hrs) cross sections experimentally determined at incident neutron spectrum averaged energies of 0.40 MeV and 0.70 MeV. This will help in improving high quality nuclear data libraries required for computations and experimental support.

Modern evaluation tries to provide not only the best estimate of the cross section but also its uncertainty and covariance describing correlation among cross sections of the same reaction or even different reactions (cross correlation). In order to provide the uncertainty and covariance in addition to the best estimate of the cross section based on the experimental knowledge, data evaluators need detailed documentation of the uncertainties in each experiment. However evaluators often face difficulty due to lack of sufficient documentation of the experiment (Otuka *et al.*, 2017). Therefore, besides reporting new experimental value, the purpose of this paper is to give a detail report in the uncertainty propagation and presentation of covariance analysis between the cross sections determined at present work along with the earlier reported values at incident neutron spectrum averaged energies of 0.96 MeV and 1.69 MeV.

## 1.6. Neutron Activation Analysis

In neutron activation method, the sample is bombarded with neutrons, causing the elements to form radioactive isotopes. The radioactive emissions and radioactive decay paths for each element are well known. Using this information, it is possible to study spectra of the emissions of the radioactive sample, and determine the concentrations of the elements within it. Georg Hevesy and Hilde Levi first reported this method in the year 1936. They observed that some elements became highly radioactive when irradiated with neutrons. At that time,

element discrimination was based on the half-life rather than the energy of the emitted radiation.

A particular advantage of neutron activation technique is that it does not destroy the sample, and thus has been used for analysis of works of art and historical artifacts. Its high sensitivity makes it possible to use in analysis of minor elements which are present in low concentrations. The method is especially useful for trace element analysis, e.g. in high-purity substances, and is therefore important in semiconductor techniques. It can also be used to detect trace element in water, biological NAA material and minerals. In archaeology, NAA can give useful information about the origin of the findings according to the so-called “fingerprint” of the individual element composition in their raw materials. It is usually used as an important reference for other analysis methods.

Neutron activation analysis (NAA) is a method for element determination based on the measurement of characteristic gamma energies from artificially produced radionuclides. These radionuclides are formed by bombarding stable elements with neutrons. NAA is performed using a nuclear reactor that produces thermal neutrons. Based on the nuclear reaction between neutrons and target nuclei, it is a useful method for the simultaneous determination of about 25-30 major, minor and trace elements of geological, environmental, biological samples without or with chemical separation (Glascock, 2003).

In NAA, samples are activated by neutrons. During irradiation the naturally occurring stable isotopes of most elements that constitute the given are transformed into radioactive isotopes by neutron capture. Then the activated nucleus decays according to a characteristic half-life; some nuclide emit beta particles and gamma-quanta, too, with specific energies. As the irradiated samples contain radionuclide of different half-lives different isotopes can be determined at various time intervals (Knoll Glenn F, 1989, 1999).

The advantage of the method is its sensitivity and accuracy especially in respect of some trace elements. The method is of a multi-element character, i.e. it enables the simultaneous determination of many elements without chemical separation. In the case of instrumental determination, (INAA), the preparation of samples involves only the preparation of representative samples, and this reduces the danger of contamination to a minimum and accelerates the whole analytical process. If the determination of some special elements or groups of elements can be carried out only through chemical separation, it is possible to carry out after irradiation. The development of the method has contributed to the elaboration of some very simple and accurate methods of standardization, which lead to a surpassingly accurate analysis.

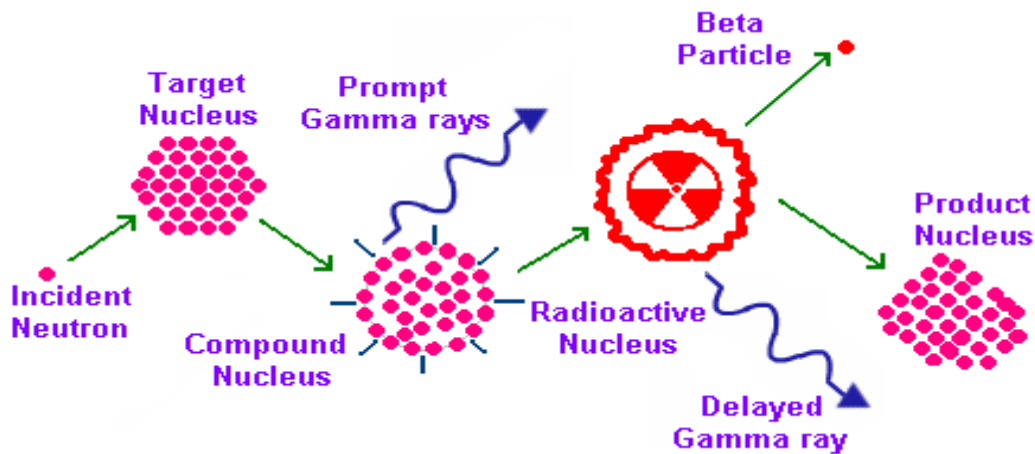


Figure 3: Diagram illustrating the process of neutron capture by a target nucleus followed by the emission of gamma rays.

Depending on the time of measurement, NAA can be divided in two categories:

(a) Prompt gamma ray neutron activation analysis (PGNAA): In PGNAA, the measurements should be taking place during irradiation. This technique is usually performed by using a beam of neutrons extracted through a reactor beam port. Fluxes on samples irradiated in beams are on the order of one million times lower than on samples inside a reactor, but

detectors can be placed very close to the sample compensating for much of the loss in sensitivity due to flux. The PGNAA technique is most applicable to elements with extremely high neutron capture cross section elements which decay too rapidly to be measured by DGNAA; elements that produce only stable isotopes after the emission of prompt gamma ray; or elements with weak gamma ray intensities (Michael D.Glascock, 2004).

(b) Delayed gamma ray neutron activation analysis (DGNAA): The gamma ray measurement takes place after sample irradiation. This technique is used for the most majority of elements that produce radioactive nuclides. The DGNAA technique is flexible with respect to time such that the sensitivity for a Long-lived radionuclide that suffers from the shorter-lived radionuclide to decay (Michael D.Glascock, 2004).

### 1.6.1. Fundamental Equations in Neutron Activation Analysis

Consider an isotope X; in the nuclear reaction, it absorbs a neutron (n).



Where  $\gamma$  is a prompt gamma ray,  $X^*$  designates excited radioactive nucleus.  $X^*$  nucleus decays via beta minus decay which converts a neutron to a proton thereby creating a stable isotope Y, a negative electron, an antineutrino  $\bar{\nu}$  and gamma rays.



So in the nuclear reaction we form  $X^*$  and it decays. Hence, the number of  $X^*$  a radioactive isotope formed with time is given by an equation:

accumulation = production in reaction - disappearance by decay

That is, 
$$\frac{dN}{dt} = \phi\sigma N_0 - \lambda N \quad (3)$$

where  $\phi$  = thermal neutron flux in neutrons/cm<sup>2</sup> sec

$\sigma$  = capture cross section, i.e., probability of absorbing neutrons in  $\text{cm}^2$

$\lambda$  = decay constant

$N_0$  = original number of X nuclei in the neutron source. Multiplying Eqn.3 by  $\lambda$  and rearranging, we get,

$$\frac{d[\lambda N]}{[\lambda N - N_0\sigma\phi]} = -\lambda dt \quad (4)$$

Integrating Eqn. (4), we get,

$$\ln(\lambda N - N_0\sigma\phi)\Big|_0^N = -\lambda t\Big|_0^t \quad (5)$$

$$\frac{[\lambda N - N_0\sigma\phi]}{-N_0\sigma\phi} = e^{-\lambda t} \quad (6)$$

Therefore, Eqn. (3) becomes,

$$N = \frac{N_0\sigma\phi}{\lambda}(1 - e^{-\lambda t}) \quad (7)$$

The activity of the product nuclei,  $A_\gamma$  at the end of irradiation is given by,

$$A_\gamma = N_0\sigma\phi(1 - e^{-\lambda t}) \quad (8)$$

The activity  $A_\gamma$  of a reaction product at any time is related to counting rate  $A_c$  in one of its characteristic photo-peaks which is given by,

$$A_\gamma = \frac{A_c \lambda}{\varepsilon_p f_s f_d} \quad (9)$$

where  $\varepsilon_p$  is the photopeak detection efficiency of the detector,  $f_s$  is the source self-absorption correction and  $f_d$  is the photon disintegration probability.

Let  $t_1$  be the time elapsed during irradiation of the sample (irradiation time),  $t_2$  is the time elapsed between the end of irradiation and the start of counting (cooling or delay time), and  $t_3$  be the length of counting time. During irradiation, there is a build-up in activity and it is shown in Figure 4.

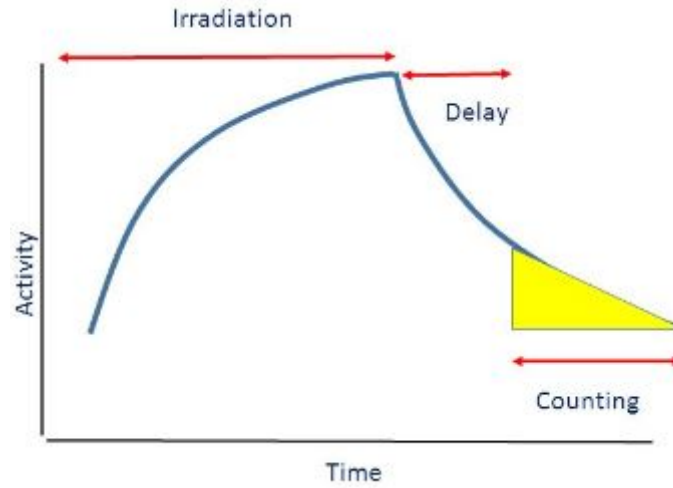


Figure 4: Graph showing the activity build-up as the sample is irradiated.

Considering correction for decay during counting interval  $t_3$ , the number of counts (count rate) detected is,

$$A_c = \frac{[N_0 \sigma \phi \epsilon_p f_s f_d (1 - e^{-\lambda t_1}) e^{-\lambda t_2} (1 - e^{-\lambda t_3})]}{\lambda} \quad (10)$$

Eqn. (10) is the activation formula used to estimate the cross sections of the activated samples. The count rates were corrected for coincidence effects, for  $\gamma$ -ray abundance,  $\gamma$ -ray self-absorption, efficiency of the detector, and measurement geometry, neutron flux fluctuations during the irradiations, and the background neutrons.

The cross-section  $\sigma$  of a neutron induced nuclear reaction can be estimated relative to the reaction monitor cross-section  $\sigma$  using the following relation:



$$\sigma = \sigma_m \frac{A_c N_m \phi \varepsilon_m f_{s,m} f_{d,m} (1 - e^{-\lambda_m t_1}) e^{-\lambda_m t_2} (1 - e^{-\lambda_m t_3})}{A_{c,m} N \phi \varepsilon f_s f_d (1 - e^{-\lambda t_1}) e^{-\lambda t_2} (1 - e^{-\lambda t_3})} \quad (11)$$

where,  $A_c$  is the number of counts under the photo peak and quantities with the subscript ‘m’ are for the monitor reaction.

## 1.7. Review of Literature

Reifarth *et al.* (2009) developed a Monte-Carlo based program **PINO** – Protons In Neutrons Out, which allows the simulation of neutron spectra considering the geometry of the setup and the proton-energy distribution. It provided a user-friendly web interface with which users can calculate neutron spectra up to 4 MeV proton energy without installation. It has been applied for analysis of cross-section measurements at the Karlsruhe Van de Graaff accelerator. The  ${}^7\text{Li}(p,n){}^7\text{Be}$  reaction in combination with a 3.7 MV Van de Graaff accelerator was routinely used at FZK to perform activation as well as time-of-flight measurements with neutrons in the keV-region. However, the input nuclear data (e.g., energy-dependent cross sections near threshold) adopted in the system are not clear, and also, users cannot change them. They compared the resulting simulated neutron spectra with the available experimentally determined neutron spectrum at the Forschungs-zentrum Karlsruhe by Ratynski and Kappeler at proton energies 1910, 1912 and 1914 keV. It predicted neutron spectra near threshold (below 1.95 MeV proton energy) reasonably well, as validated by experimental results. On the other hand, their predicted neutron spectra are not well studied in the higher-energy region. PINO is available as a web-application at the URL <http://exp-astro.physik.uni-frankfurt.de/pino>.

Birgersson and Lovestam (2009) also developed a code, NeuSDesc (Neutron Source Description) for calculation of the  ${}^7\text{Li}(p,n){}^7\text{Be}$  neutron source spectra. The program was developed at JRC-IRMM as a tool for calculating the neutron fluence spectra generated by

nuclear ion beams and binary nuclear reactions. It was developed on the Energy Set platform. Here, the Energy Set real-time style presenting of calculated neutron fluence and spectrum have been kept, but also intrinsic and parasitic peak broadening effects such as energy and angular straggling of the ions in the beam, energy spread of incident ion beam, and possible non-homogeneity of the entrance foil for gas targets had been included. The main objective for the development of NeuSDesc was simulation of the neutron spectrum for a complete neutron beam facility. The program does not require any installation routine; however, a number of input data text files are required to be located in the same directory as the executable file. If an input file is changed, the program has to be re-started.

Friedman et al. (2013) developed a tool (SimLiT) for calculating the neutron spectrum from the  ${}^7\text{Li}(p,n){}^7\text{Be}$  reaction with proton energy close to the reaction threshold (1.88 - 2 MeV). It is a Monte Carlo simulation. The principal was to sample single protons with an energy randomly chosen within the energy distribution of the beam. It calculated the spectrum and yield at various beam energies, energy spread and lithium target chemical compositions. It was designed as a C++ object, in order to allow advanced computational analysis, especially as a neutron source for the Geant4 code. It is freely available from its web page including its source code though its installation is necessary. Originally, it was designed up to 2 MeV of proton energy. Recently, it had been upgraded to higher proton energies.

Herrera et al. (2015) presented a new method based on center-of-mass and relative coordinates to describe the  ${}^7\text{Li}(p,n){}^7\text{Be}$  reaction near threshold. The resulting numerical scheme was implemented in a C++ code that allows the calculation of any kinematical quantity in the process by simple function calls. Using the method, they analyzed most of the available measurements to obtain a consistent description of the double differential neutron yield for accelerator based neutron sources. In the energy dependence of the neutron to proton width ratio, the value of the constant parameter adopted was C. After a careful study,

Herrera et al. reported that the best fit to the experimental excitation functions was obtained with  $C = 3.60 \pm 0.25$ , but they concluded that  $C = 6$  was more suitable for neutron source applications. They compared their result with the experimental data of Kononov *et al.* (1977) and Feinberg *et al.* (2012). They reported that the differential yield of neutrons presented by Kononov *et al.* was the most sensitive part when a Breit-Wigner formula was assumed to describe the threshold process in the proton energy range of threshold energy to 1.93 MeV.

Mangal *et al.* (1962) measured thermal neutron capture cross-sections for the  $^{70}\text{Zn}(n,\gamma)^{71}\text{Zn}^m$  and  $^{70}\text{Zn}(n,\gamma)^{71}\text{Zn}$  using activation technique by making irradiation with the "Swimming pool" reactor at Trombay, Bombay. Zinc oxide film was irradiated near the core, because 14 h irradiation in the thermal column failed to give 3 h activity. In such cases, the flux of neutrons at the point of irradiation was of the order of  $10^{11}$  neutrons per  $\text{cm}^2 \cdot \text{sec}^{-1}$ . An end window  $\beta$ -counter was used for nuclei which decay through  $\beta$ -particle emission. The  $^{55}\text{Mn}(n,\gamma)^{56}\text{Mn}$  reaction was taken as the standard, with cross-section as  $13.4 \pm 0.3$  b. The measured thermal neutron capture cross-sections for the  $^{70}\text{Zn}(n,\gamma)^{71}\text{Zn}^m$  and  $^{70}\text{Zn}(n,\gamma)^{71}\text{Zn}$  are  $9 \pm 20$  % mb and  $111 \pm 20$  % mb, and isomeric cross-section ratios for target nuclei of spin 0 i.e.,  $^{71}\text{Zn}^m / ^{70}\text{Zn}^{71}$  is  $0.041 \pm 0.017$  with competing levels of  $\frac{9}{2} / \frac{1}{2}$ .

Mannhart *et al.* (1968) determined thermal capture cross sections and isomeric cross section ratios in thermal neutron capture for even-even nuclei in the region of the  $2P_{1/2} - 1g_{9/2}$  neutron shell. Capture cross sections for formation of  $^{71}\text{Zn}^m$  and  $\text{Zn}^{71}$  were measured by the activation method using  $^{197}\text{Au}(n,\gamma)^{198}\text{Au}$  as monitor with cross section as  $98.5 \pm 0.4$  b. From these data and additional measurements of cross section ratios the isomeric ratios for thermal capture in  $^{70}\text{Zn}$  was determined. The isomer ratios were compared with calculations based on the statistical model of HUIZENGA and VANOENBOSCH. The measured thermal neutron capture cross sections for the  $^{70}\text{Zn}(n,\gamma)^{71}\text{Zn}^m$  and  $^{70}\text{Zn}(n,\gamma)^{71}\text{Zn}$  are  $0.0081 \pm 0.0005$  % b and  $0.083 \pm 0.005$  % b.

Cohen *et al.* (2005) measured the reactor thermal neutron capture cross section for the resonance integrals of the reactions  $^{70}\text{Zn}(n,\gamma)^{71}\text{Zn}$  and  $^{70}\text{Zn}(n,\gamma)^{71}\text{Zn}^m$ , referred to the tabulated value for the resonance integral of the  $^{68}\text{Zn}(n,\gamma)^{69}\text{Zn}^m$  reaction with cross section as  $0.24 \pm 0.03$  b. No previous data were found on the discriminated resonance integrals for the capture reactions on  $^{70}\text{Zn}$ . The present results are  $0.1350 \pm 0.0093$  b, for the  $^{70}\text{Zn}(n,\gamma)^{71}\text{Zn}$  reaction (average of four measurements) and  $0.157 \pm 0.029$  b for the  $^{70}\text{Zn}(n,\gamma)^{71}\text{Zn}^m$  reaction, the latter corresponding to a single measurement of the resonance integral. As it was mentioned, no corrections for the departures from the ideal behavior of the epithermal flux were performed, and literature data on the mean effective resonance energy are lacking for these reactions. Therefore, these results should be considered as informative or working values, only. The mean values of the epithermal flux per unit  $\ln E$ , as measured the reaction  $^{68}\text{Zn}(n,\gamma)^{69}\text{Zn}^m$ , which was used as internal standard, was  $8.4 \times 10^{10} \text{ n cm}^{-2} \text{ s}^{-1}$  respectively.

Reifarth *et al.* (2012) measured the neutron-capture cross sections of  $^{64}\text{Zn}$ ,  $^{68}\text{Zn}$ , and  $^{70}\text{Zn}$  with the activation technique in a quasi-stellar neutron spectrum via the  $^7\text{Li}(p,n)^7\text{Be}$  reaction corresponding to a thermal energy of  $kT = 25$  keV. By a series of repeated irradiations with different experimental conditions, an uncertainty of 3% could be achieved for the  $^{64}\text{Zn}(n,\gamma)^{65}\text{Zn}$  cross section and for the partial cross section  $^{68}\text{Zn}(n,\gamma)^{69}\text{Zn}^m$  feeding the isomeric state in  $^{69}\text{Zn}$ . For the partial cross sections  $^{70}\text{Zn}(n,\gamma)^{71}\text{Zn}^m$  and  $^{70}\text{Zn}(n,\gamma)^{71}\text{Zn}^g$ , which had not been measured so far, uncertainties of only 16% and 6% could be reached because of limited counting statistics and decay intensities. Compared to previous measurements on  $^{64,68}\text{Zn}$ , the uncertainties could be significantly improved, while the  $^{70}\text{Zn}$  cross section was found to be two times smaller than the existing model calculations. From these results Maxwellian average cross sections were determined between 5 and 100 keV. Additionally, the  $\beta$ -decay half-life of  $^{71}\text{Zn}^m$  could be determined with significantly improved accuracy. The

consequences of these data have been studied by network calculations for convective core He burning and convective shell C burning in massive stars.

Krane (2017) measured the radiative thermal neutron capture cross sections  $^{70}\text{Zn}(n,\gamma)^{71\text{m,g}}\text{Zn}$  reaction. Irradiations were done in the TRIGA reactor of the Oregon State University Radiation Center. Several different irradiation sites were used: one in the central core, which also featured a Cd-lined facility to absorb thermal neutrons (nominal thermal and epithermal fluxes of  $9.0 \times 10^{12}$  and  $1.2 \times 10^{12}$  neutrons  $\text{cm}^{-2} \text{s}^{-1}$ ); a fast pneumatic transfer facility (rabbit) located in the outer ring of the core ( $4.4 \times 10^{12}$  and  $3.4 \times 10^{11}$  neutrons  $\text{cm}^{-2} \text{s}^{-1}$ ); and a thermal column located behind graphite shielding about 2 m from the core ( $7.8 \times 10^{10}$  and  $2.0 \times 10^8$  neutrons  $\text{cm}^{-2} \text{s}^{-1}$ ). All of the irradiations for the cross-section measurements were accompanied by Au and Co as dilute impurities in aluminum foils which served as flux monitors.

The resonance integrals were also measured to facilitate corrections for the epithermal neutron component. In addition, cross sections for the  $^{64}\text{Zn}(n,\gamma)^{65}\text{Zn}$  and  $^{68}\text{Zn}(n,\gamma)^{69\text{m}}\text{Zn}$  reactions were determined. The  $\gamma$  rays from the irradiated samples were observed with high resolution Ge detectors (efficiency 35–40% compared with NaI at 1332 keV, resolution 1.7–1.8 keV at 1332 keV). Through high-resolution  $\gamma$ -ray spectrometry in the  $^{71\text{m}}\text{Zn}$  decay, a new set of  $\gamma$ -ray energies and intensities was obtained of roughly an order of magnitude greater precision than the previous set, and several transitions new to the decay scheme are proposed. The implications for the properties of the levels of  $^{71}\text{Ga}$  are discussed. More precise values of the decay half-lives for  $^{69\text{m}}\text{Zn}$ ,  $^{71\text{g}}\text{Zn}$ , and  $^{71\text{m}}\text{Zn}$  were determined.

Punte *et al.* (2017) measured the cross sections of the  $^{70}\text{Zn}(n,\gamma)^{71}\text{Zn}^{\text{m}}$  ( $T_{1/2} = 3.96 \pm 0.05\text{-h}$ ) reaction relative to the  $^{197}\text{Au}(n,\gamma)^{198}\text{Au}$  cross sections at 0.96 and 1.69 MeV using a  $^7\text{Li}(p,n)^7\text{Be}$  neutron source and activation technique. The cross section of this reaction had been measured for the first time in the MeV region. The new experimental cross sections had

been compared with the theoretical prediction by TALYS-1.6 with various Level Density Models and Photon Strength Functions as well as the TENDL-2015 library. The TALYS-1.6 calculation with the generalized superfluid Level Density Model and Kopecky-Uhl generalized Lorentzian Photon Strength Function predicted the new experimental cross sections at both incident energies. The  $^{70}\text{Zn}(n,\gamma)^{71}\text{Zn}^{\text{g+m}}$  total capture cross sections had also been derived by applying the evaluated isomeric ratios in the TENDL-2015 library to the measured partial capture cross sections. The derived spectrum averaged total capture cross sections agree well with the JENDL-4.0 library at 0.96 MeV, whereas it lies between the TENDL-2015 and the JENDL-4.0 libraries at 1.69 MeV.

**CHAPTER – 2**

**NEUTRON ENERGY SPECTRUM**

**CODE-ENERGY OF PROTON ENERGY OF**

**NEUTRON (EPEN)**

### 2.1. ${}^7\text{Li}(p,n){}^7\text{Be}$ reaction as a neutron source

Conventional quasi-mono-energetic neutron sources produce neutrons isotropically via direct reactions on light nuclei, e.g.  $d(d,p)n$  or  ${}^7\text{Li}(p,n){}^7\text{Be}$  (Lebois *et al.*, 2014). It has been suggested by M.A. Chaudhri *et al.* (1974) that the  ${}^7\text{Li}(p,n){}^7\text{Be}$  reaction would be more suitable for cyclotron production of therapy neutrons than the commonly used  $\text{Be}(d,n)$  reaction, especially for smaller cyclotrons which cannot produce medically useful beams from a Be target. They also pointed out that a "moderately thick" target would produce higher mean neutron energies than an "infinitely-thick" target (stopping the incident beam completely). Although the  ${}^7\text{Li}(p,n){}^7\text{Be}$  reaction is truly monoenergetic only below 0.65 MeV neutron energy (Drosg, 1981), it has been most widely used as a quasi-monoenergetic neutron source reaction because of (1) the rapid rise of the cross section in the near threshold region that provides a large amount of relatively low-energy neutrons and (2) the large level spacing of  ${}^7\text{Be}$  between the first (429 keV) and second (4570 keV) excitation levels that is suitable to produce quasi-monoenergetic neutrons. The following table presents the reaction Q-values and thresholds.



**Table 1:** Representation of  ${}^7\text{Li}(p,n){}^7\text{Be}$  reaction Q-value and Threshold.

Reaction	${}^7\text{Be}$ Excitation Energy (MeV)	Q-Value (MeV)	Threshold (MeV)
${}^7\text{Li}(p,n){}^7\text{Be}$	0	-1.644	1.881 forward 1.920 backward
${}^7\text{Li}(p,n){}^7\text{Be}^*$	0.431	-2.075	2.373 forward 2.423 backward
${}^7\text{Li}(p,n{}^3\text{He}){}^4\text{He}$	break-up	-3.229	3.692
${}^7\text{Li}(p,n){}^7\text{Be}^{**}$	4.55	-6.19	7.08

This neutron source reaction has been utilized for experimental studies of several neutron-induced reactions. It is also a strong candidate as small accelerator-based neutron sources for Boron neutron capture therapy (BNCT) which is a cancer treatment modality. BNCT accelerator-based neutron sources are considered to be more suitable neutron sources than reactor-based neutron sources because they offer the following features: ease of operation, low cost, and small space occupation.

The neutrons produced using the reaction in inverse kinematics combines the best features of white neutron sources (collimated beams) and conventional quasi-monoenergetic neutron sources (high neutron fluxes at short distances). But it involves the use of reactions such as  $p({}^7\text{Li},n){}^7\text{Be}$  in the 13-17 MeV energy range and thus requires a 9 MV tandem accelerator or 115 MeV cyclotron in order to accelerate  ${}^7\text{Li}^{3+}$  ions up to these energies. Unfortunately, due to the worldwide closure of many accelerator laboratories over the last few decades, there are only a handful of accelerators left capable of producing focused neutrons via this method (Lebois *et al.*, 2014).

## 2.2. Importance of the work

In the experimental determination of neutron-induced reaction cross section, subtractions of the  $(p, n_1)$  and breakup neutron contributions are always an essential part, but they have not always been done in a proper manner. If the proton energy is above  $E_p = 2.37$  MeV, a second neutron production channel  ${}^7\text{Li}(p, n_1){}^7\text{Be}$  opens in addition to  ${}^7\text{Li}(p, n_0){}^7\text{Be}$ , which leads to a second neutron group at lower energies. The neutron group due to the  ${}^7\text{Li}(p, n_2){}^7\text{Be}$  reaction does not appear until  $E_p = 7.07$  MeV, but the  ${}^7\text{Li}(p, n+{}^3\text{He}+\alpha)$  three-body breakup channel also opens at proton energies above  $E_p = 3.70$  MeV and shows a broad neutron spectrum.

Neutron capture cross sections decrease as the neutron energy increases in general, and therefore, the contribution of the low-energy background neutrons has to be carefully determined and subtracted. However, it has been done in the previous experimental works assuming experimental  ${}^7\text{Li}(p, n+x)$  double-differential cross sections at similar proton energies in the literature as the neutron source spectra.

We measured the  ${}^{70}\text{Zn}(n, \gamma){}^{71}\text{Zn}^m$  ( $T_{1/2} = 3.96$  h) activation cross sections using the  ${}^7\text{Li}(p, n){}^7\text{Be}$  reaction as neutron source at proton energies 2.25, 2.60, 2.80, and 3.50 MeV with a proton beam spread of 20 keV at BARC-FOTIA. These proton energies are below the  ${}^7\text{Li}(p, n+{}^3\text{He}+\alpha)$  reaction threshold but above the  ${}^7\text{Li}(p, n_1){}^7\text{Be}$  reaction threshold except the lowest one. Since the time-of-flight and multiple foil activation techniques cannot be applied at BARC-FOTIA due to the continuous beam structure and weak neutron flux, we have to rely on calculated neutron energy spectra for subtraction of the  ${}^7\text{Li}(p, n_1){}^7\text{Be}$  contribution to  ${}^{71}\text{Zn}^m$  production.

There are some codes for calculation of  ${}^7\text{Li}(p, n){}^7\text{Be}$  neutron source spectra (Reifarth *et al.*, 2009; Birgersson and Lövestam, 2009; Friedman *et al.*, 2016; Herrera *et al.*, 2015). All

these codes predicted neutron spectra near threshold reasonably well, which are well validated by experimental results. Moreover, some of them can predict neutron spectra up to  $E_p = 4$  MeV. However, their predicted neutron spectra are not well studied in the higher-energy region. There are discrepancies between the neutron spectra predicted by PINO (Reifarth *et al.*, 2009) and SimLiT (Friedman *et al.*, 2016) in the higher proton energies, which will be discussed in Section 2.5.2. It is difficult to understand which one is correct and to be adopted for neutron-induced experimental data reduction procedure. Under this situation, we decided to study the thick and thin target  ${}^7\text{Li}(p,n_{0,1}){}^7\text{Be}$  neutron spectra by developing the new deterministic code, **EPEN** - **E**nergy of **P**roton **E**nergy of **N**eutron. The code is available at Mizoram University website (<http://www.epen.nhergmzu.com/epen/>). Initially, the code was designed up to 4 MeV but recently, it had been extended up to 7 MeV.

### 2.3. Formalism for Calculating the Neutron Energy Spectrum

Below the threshold of the three-body break-up reaction, the neutron production is described by the two-body kinematics for  ${}^7\text{Li}(p,n_0){}^7\text{Be}$  and  ${}^7\text{Li}(p,n_1){}^7\text{Be}$ . Any combination of the outgoing angle and energy of a neutron ( $\theta$ ,  $E_n$ ) uniquely specifies the incident energy of protons at the interaction point  $E_p = E_p(\theta, E_n)$  (Figure 5):

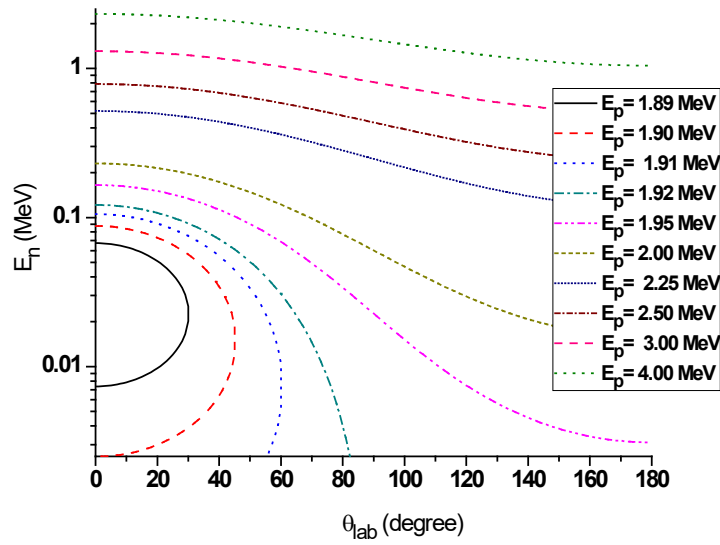


Figure 5: Proton energy contours for the  ${}^7\text{Li}(p,n){}^7\text{Be}$  reaction.

### 2.3.1. Nuclear Reaction Kinematics

The conservation of energy and momentum imposes certain restrictions on the reactions. These reactions are called kinematic restrictions and this mathematical method is known as kinematics. For the nuclear reaction as shown in Figure 6,

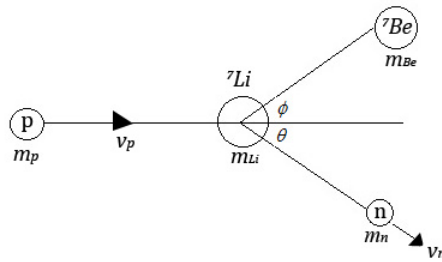


Figure 6: Schematic diagram of a nuclear reaction.

The lithium target nucleus is at rest and it has no kinetic energy. Since the total energy is conserved in a nuclear reaction, we get,

$$m_{Li}c^2 + (E_p + m_p c^2) = (E_{Be} + m_{Be}c^2) + (E_n + m_n c^2) \quad (13)$$

where,

$m_p(1.00727645119u)$  = proton nuclear mass

$m_n(1.00866491585u)$  = neutron nuclear mass

$m_{Li}(7.01435769347u)$  =  ${}^7\text{Li}$  nuclear mass (Tilley *et al.*, 2004)

$m_{Be}$  =  ${}^7\text{Be}$  nuclear mass

Introducing a quantity  $Q$ , which represents the difference between the kinetic energy of the products of reaction and that of the incident particle, we have,

$$Q = E_{Be} + E_n - E_p \quad (14)$$

It is called the energy balance of the reaction or commonly  $Q$  – value of the reaction and it can have either positive or negative values. From Eqn. (13) and (14), we have,

$$(m_{Li} + m_p - m_{Be} - m_n)c^2 = Q \quad (15)$$

Applying the laws of conservation of momentum, we have,

$$m_p v_p = m_{Be} v_{Be} \cos \phi + m_n v_n \cos \theta \quad (16)$$

$$m_{Be} v_{Be} \sin \phi = m_n v_n \sin \theta \quad (17)$$

where  $v_p$ ,  $v_n$  and  $v_{Be}$  are velocities of proton, neutron and  ${}^7\text{Be}$  respectively.

Eliminating  $\phi$ , we get,

$$m_{Be}^2 v_{Be}^2 = m_p^2 v_p^2 + m_n^2 v_n^2 - 2m_p m_n v_p v_n \cos \theta \quad (18)$$

Since  $E = \frac{1}{2} m v^2$ , Eqn. (18) can be rewritten as,

$$2E_{Be}m_{Be} = 2E_p m_p + 2E_n m_n - 4\sqrt{m_p m_n E_p E_n} \cos \theta$$

$$E_{Be} = E_p \frac{m_p}{m_{Be}} + E_n \frac{m_n}{m_{Be}} - \frac{2}{m_{Be}} \sqrt{m_p m_n E_p E_n} \cos \theta \quad (19)$$

Now, substituting Eqn.(19) in Eqn.(14), we obtain,

$$Q = \frac{(m_p - m_{Be})}{m_{Be}} E_p + \frac{(m_n + m_{Be})}{m_{Be}} E_n - \frac{2}{m_{Be}} \sqrt{m_p m_n E_p E_n} \cos \theta$$

Solving, we get,

$$E_p^2 (m_p - m_{Be})^2 + E_p (2Qm_{Be}^2 - 2Qm_{Be}m_p + 2m_p m_n E_n + 2m_p m_{Be} E_n - 2m_{Be} m_n E_n - 2m_{Be}^2 E_n^2 - 4m_p m_n \cos^2 \theta) + (Q^2 m_{Be}^2 - 2Qm_n m_{Be} E_n - 2Qm_{Be}^2 E_n + m_n^2 E_n^2 + 2m_n E_n^2 m_{Be} + m_{Be}^2 E_n^2) = 0$$

Using quadratic equation,

$$E_p = \frac{-b \pm \sqrt{b^2 - 4ac}}{2a}$$

where,

$$a = (m_p - m_{Be})^2$$

$$b = 2 \left[ (m_p - m_{Be}) \left\{ (m_n + m_{Be}) E_n - Qm_{Be} \right\} - 2m_p m_n E_n \cos^2 \theta \right]$$

$$c = Q^2 m_{Be}^2 - 2Q(m_n + m_{Be}) m_{Be} E_n + (m_n + m_{Be})^2 E_n^2$$

Now,

$$\begin{aligned}
-\frac{b}{2a} &= -\frac{\left[ (m_p - m_{Be}) \left\{ (m_n + m_{Be}) E_n - Q m_{Be} \right\} - 2 m_p m_n E_n \cos^2 \theta \right]}{(m_p - m_{Be})^2} \\
&= E_n \left[ 2 \cos^2 \theta \frac{m_p m_n}{(m_{Be} - m_p)^2} + (m_n + m_{Be}) \right] + E_{th} \frac{(m_n + m_{Be} - m_p) m_{Be}}{(m_n + m_{Be})(m_{Be} - m_p)} \quad (20)
\end{aligned}$$

And

$$\begin{aligned}
\frac{\sqrt{b^2 - 4ac}}{2a} &= \frac{\sqrt{16 \cos^2 \theta \left[ E_n^2 \left\{ m_p m_n (m_{Be} - m_p)(m_{Be} + m_n) + m_p^2 m_n^2 \cos^2 \theta \right\} + E_n Q m_p m_n m_{Be} (m_p - m_{Be}) \right]}}{2(m_p - m_{Be})^2} \\
&= \frac{4 \cos \theta}{2(m_p - m_{Be})^2} \sqrt{E_n^2 \left\{ m_p m_n (m_{Be} - m_p)(m_{Be} + m_n) + m_p^2 m_n^2 \cos^2 \theta \right\} + E_n \left\{ -E_{th} \frac{m_2}{(m_p + m_{Li})} \right\} m_p m_n m_{Be} (m_p - m_{Be})} \\
&= \frac{2 \cos \theta}{(m_{Be} - m_p)^2} \sqrt{E_n^2 \left\{ m_p m_n (m_{Be} - m_p)(m_{Be} + m_n) + m_p^2 m_n^2 \mu^2 \right\} + E_n E_{th} m_p m_n m_{Be} \frac{(m_n + m_{Be} - m_p)(m_{Be} - m_p)}{(m_n + m_{Be})}} \quad (21)
\end{aligned}$$

Now, substituting Eqn. (20) and (21) in the quadratic equation, we get,

$$\begin{aligned}
E_p &= E_n \left[ \frac{m_{Be} + m_n}{(m_{Be} - m_p)} + 2 \cos^2 \theta \frac{m_p m_n}{(m_{Be} - m_p)^2} \right] + \frac{(m_n + m_{Be} - m_p) m_{Be}}{(m_n + m_{Be})(m_{Be} - m_p)} E_{th} \\
&\pm \frac{2 \cos \theta}{(m_{Be} - m_p)^2} \sqrt{E_n^2 \left\{ (m_{Be} - m_p)(m_{Be} + m_n) m_p m_n + m_p^2 m_n^2 \mu^2 \right\} + E_n E_{th} \frac{m_p m_n m_{Be} (m_{Be} + m_n - m_p)(m_{Be} - m_p)}{(m_{Be} + m_n)}}
\end{aligned}$$

Rearranging, we obtain the equation for the incident proton energy,

$$\begin{aligned}
E_p = E_n \left[ \frac{(m_{Li} + m_p)}{(m_{Li} - m_n)} + \frac{2m_p m_n \cos^2 \theta}{(m_{Li} - m_n)^2} \right] + E_{th} \left[ \frac{m_{Li} (m_{Li} + m_p - m_n)}{(m_{Li} + m_p)(m_{Li} - m_n)} \right] \\
- \frac{2 \cos \theta}{(m_{Li} - m_n)^2} \left[ E_n^2 \left\{ m_p m_n (m_{Li} + m_p)(m_{Li} - m_n) + m_p^2 m_n^2 \cos^2 \theta \right\} + \frac{E_n E_{th} m_p m_n m_{Li} (m_{Li} + m_p - m_n)(m_{Li} - m_n)}{(m_{Li} + m_p)} \right]^{1/2}
\end{aligned} \tag{22}$$

### 2.3.2. Laboratory differential cross sections for proton energies above 1.95 MeV

Liskien and Paulsen (1975) compiled extensive experimental cross section measurements from the existing literature and generated best fits to the data over the proton energy range from 1.95 to 7.0 MeV for both the reaction leading to the ground state of  ${}^7\text{Be}$  and the first excited state, which has a threshold at 2.37 MeV. The angular differential cross section for  ${}^7\text{Li}(p,n_0){}^7\text{Be}$  and  ${}^7\text{Li}(p,n_1){}^7\text{Be}$  reactions for  $E_p \geq 1.95$  MeV and  $E_p \geq 2.50$  MeV respectively was adopted. We also adopted their recommended zero degree differential cross sections and Legendre coefficients in the center of mass system. These center of mass cross sections for the first neutron groups are given as Legendre polynomial expansions as:

$$\frac{d\sigma}{d\Omega_{cm}}(\theta) = \frac{d\sigma}{d\Omega_{cm}}(0^\circ) \sum_{i=0}^3 A_i(E_p) P_i(\cos \theta) \tag{23}$$

And for the second group of neutrons,

$$\frac{d\sigma^*}{d\Omega_{cm}}(\theta) = \frac{d\sigma}{d\Omega_{cm}}(0^\circ) R \sum_{i=0}^3 A_i(E_p)^* P_i(\cos \theta) \tag{24}$$

where,

$$R = \frac{d\sigma^*/d\Omega(0^\circ)}{d\sigma/d\Omega(0^\circ)}$$

The proton energy-dependent parameters  $A_0$ ,  $A_1$ ,  $A_2$ ,  $A_3$ , and  $d\sigma_{pn}/d\Omega'(0)$  are tabulated, making it extremely simple to use their fits for calculating reaction cross sections.



The Legendre coefficients and 0 degree cross sections between two proton energies were then interpolated by a straight line on the logarithmic-logarithmic scale.

In order to obtain the  ${}^7\text{Li}(p,n_0){}^7\text{Be}$  differential cross section between 1.92 MeV and 1.95 MeV, cubic splines were fitted through the data points given in Liskien and Paulsen's paper for smooth variation of the cross section parameters with proton energy.

### 2.3.3. Near threshold non-relativistic two body kinematics

The threshold energy of the ground state neutrons for the  ${}^7\text{Li}(p,n){}^7\text{Be}$  reaction is at 1.881 MeV. Operation of the proton energy in the near threshold region will produce thick target neutron yields. But the neutrons produced in this region will have relatively low energy neutrons which require very low moderation for BNCT. For proton energies below 1.92 MeV, i.e. in the near threshold region, the neutron production is double-valued, giving two neutron energies for each angle of emission. Besides this, the neutrons are produced in the forward direction only ( $\theta < 90^\circ$ ). The neutron energy at threshold is determined using the relation

$$E_n(E_{th}) = \frac{m_p m_n E_{th}}{(m_{Be} + m_n)^2} \quad (25)$$

where the notations are similar as in Section 2.3.1.

Lee and Zhou (1999) gave a report on the detailed description of the method developed for determining the thick target neutron yields from the  ${}^7\text{Li}(p,n){}^7\text{Be}$  reaction in the near threshold region. The neutron yields are calculated for the lithium metal as well as for several lithium compounds of low molecular weight. They also demonstrated a method for calculating the neutron yields for targets that are not sufficiently thick to slow protons past the reaction threshold. The formalism adopted in the present work for the near threshold

region is very similar to the formalism adopted by them. However, there are two main differences:

(1) The kinematic equations are written in terms of  ${}^7\text{Li}$  mass instead of  ${}^7\text{Be}$  mass everywhere due to the fact that the  ${}^7\text{Li}$  mass is more accurately known by an order of two (n.b. at the non-relativistic limit  $m_p + m_{Li} = m_n + m_{Be}$  where  $m_p$  and  $m_n$  are the masses of proton and neutron,  $m_{Li}$  is the ground state mass of  ${}^7\text{Li}$ , and  $m_{Be}$  is the ground or first excitation state mass of  ${}^7\text{Be}$ ).

(2) It was impossible to reproduce the results presented by Lee and Zhou (see Figure 4 Lee and Zhou, 1999) using their adopted kinematic equations and the “ $\pm$ ” selection criteria prescribed by them in the double-valued region. Their formalism always yield a dip around 30 keV in the differential neutron energy spectrum near threshold. We therefore prescribed our own “ $\pm$ ” selection criteria in the double-valued region that is described below.

Ritchie (1976) evaluated the angle-dependent spectra of neutrons, emitted by a thick lithium target when bombarded with protons in the energy range 1.881-3 MeV, from experimental and theoretical values of the angular distribution of neutrons emitted in the  ${}^7\text{Li}(p,n){}^7\text{Be}$  reaction. For the ground and excited state reactions, the variation of  $d^2N/dE_n d\Omega$  with proton energy at different angles of emission and with angle of emissions for different neutron energies was presented. It is worth mentioning that our formalism and Ritchie’s formalism are very similar except for the treatment of “ $M_y$ ” which is treated as the mass of  ${}^7\text{Li}$  by Ritchie (Ritchie, 1976) but treated as the mass of  ${}^7\text{Be}$  by us.

The double differential neutron yield for one incident proton is

$$\frac{d^2Y(\theta, E_n)}{dE_n d\Omega} = \left(\frac{dE_p}{dE_n}\right) \left(-\frac{dx}{dE_p}\right) \rho \left(\frac{d\Omega_{cm}}{d\Omega}\right) \frac{d\sigma(E_p, \theta)}{d\Omega_{cm}} \quad (26)$$

where  $\rho$  is the volume number density of  ${}^7\text{Li}$  nuclei,  $x$  is the thickness of the lithium target,  $\Omega$  and  $\Omega_{cm}$  are the solid angles of outgoing neutrons in the laboratory and centre-of-mass system,  $d\sigma(E_p, \theta)/d\Omega_{cm}$  is the angular differential cross section of the neutron in the centre-of-

mass system. The quantity  $(-1/\rho)(dE_p/dx)$  is known as the stopping power and we obtained it by SRIM (Ziegler and Biersack, 2013). By solving the non-relativistic two body kinematic equations (Winter, 1968) the product of the Jacobians  $(dE_p/dE_n) (d\Omega_{cm}/d\Omega)$  is

$$\left(\frac{dE_p}{dE_n}\right) \left(\frac{d\Omega_{cm}}{d\Omega}\right) = \pm \frac{(m_{Li}+m_p)^2 (\cos\theta \pm \xi) \gamma E_p}{[m_p m_n E_p \xi (\cos\theta \pm \xi) \pm m_{Li} (m_{Li}+m_p-m_n) E_{th}]}, \quad (27)$$

where, following earlier workers (Lee and Zhou, 1999; Ritchie, 1976; Winter, 1968; Theobald *et al.*, 1971), the two variables  $\xi$  and  $\gamma$  are defined by

$$\xi^2 = \frac{1}{\gamma^2} - \sin^2 \theta \quad (28)$$

$$\gamma = \left\{ \left[ \frac{m_p m_n}{m_{Li} (m_{Li} + m_p - m_n)} \right] \left[ \frac{E_p}{(E_p - E_{th})} \right] \right\}^{\frac{1}{2}}$$

where

$$\begin{aligned} E_{th} &= 1880.36 \text{ keV} = {}^7\text{Li}(p,n_0){}^7\text{Be} \text{ reaction threshold} \\ &= 2371.05 \text{ keV} = {}^7\text{Li}(p,n_1){}^7\text{Be} \text{ reaction threshold.} \end{aligned}$$

The  $\pm$  sign is corresponding to the two neutron energies for a given  $E_p$  and  $\theta$  in the double-valued region ( $E_p < 1.92$  MeV; see Figure 5):

$$E_{n\pm} = \left[ \frac{m_p m_n}{(m_{Li}+m_p)^2} \right] (\cos\theta \pm \xi)^2 E_p \quad (29)$$

where  $E_{n+}$  and  $E_{n-}$  are a larger and smaller value of  $E_n$ , respectively, for a given  $\theta$  and  $E_p$  in a double-valued region. Therefore, the signs + and - in kinematic equations are selected for a set of  $(E_{n+}, \theta, E_p)$  and  $(E_{n-}, \theta, E_p)$ , respectively, for calculation of differential cross section in the double-valued region  $E_p < 1.92$  MeV, and only the + sign is considered for  $E_p > 1.92$  MeV. In order to calculate the neutron spectrum for given initial proton energy, Li foil thickness and geometry (shape and size of the neutron activation sample as well as its distance from the Li foil), we prepare tables from threshold to 7 MeV of  $E_p$  and  $d^2Y(\theta, E_n)/dE_n d\Omega$  at various  $E_n$  (in 1 keV step) and  $\theta$  (in 1 deg step) for  $(p,n_0)$  and  $(p,n_1)$  neutrons according to Eqn. (26), and

integrate them over the angular range corresponding to the proton energy range and also covered by the neutron activation sample.

In the following subsections, we introduce the details of the angular differential cross sections and angular integration.

### 2.3.4. Angular differential cross section

The  ${}^7\text{Li}(p,n_0){}^7\text{Be}$  reaction cross section between  $E_{\text{th}}$  to 1.920 MeV is strongly affected by the resonance near the threshold ( $E_x({}^8\text{Be})=18.910$  MeV,  $\Gamma_{\text{cm}}=122$  keV,  $J^\pi=2^-$ ) (Tilley, 2004) for which the following functional form proposed by Macklin and Gibbons (Macklin and Gibbons, 1958) was adopted (See also Newson *et al.*, 1957):

$$\frac{d\sigma}{d\Omega_{\text{cm}}} = \left(\frac{1}{k^2}\right) \frac{g\Gamma_p\Gamma_n}{[4(E_p - E_r)^2 + \Gamma_{\text{tot}}]^2} \sim \left(\frac{g}{k^2}\right) \frac{\Gamma_n/\Gamma_p}{\left(1 + \frac{\Gamma_n}{\Gamma_p}\right)^2} \quad (30)$$

where  $A = \frac{g}{k^2} = \left[ \frac{(2J+1)/(2J_p+1)}{(2J_{\text{Li}}+1)} \right] \frac{\hbar^2(m_p+m_{\text{Li}})^2}{(2m_p m_{\text{Li}}^2 E_p)} \sim 169.53$  MeV·mb/sr,

$g$  is the spin statistical factor and  $k$  is the center-of-mass proton wavelength on the resonance;  $J=2$ ,  $J_p=1/2$  and  $J_{\text{Li}}=3/2$  are the spins of the  ${}^8\text{Be}$  resonance, proton and  ${}^7\text{Li}$ (g.s.). This parameter (169.53 MeV·mb/sr) is slightly higher than the value 164.913 MeV·mb/sr chosen by Lee and Zhou (Lee and Zhou, 1999). The energy dependence of the width ratio is expressed by

$$x = \frac{\Gamma_n(E_p)}{\Gamma_p(E_p)} = C \left(1 - \frac{E_{\text{th}}}{E_p}\right)^{\frac{1}{2}} \quad (31)$$

With  $C=4.72$  by Ritchie (1976) or  $C=6$  by Lee and Zhou (1999). Herrera *et al.* (2015) reported that the best fit to experimental excitation functions by Macklin *et al.* (1958), Newson *et al.* (1957) and Gibbons *et al.* (1959) is obtained with  $C = 3.60 \pm 0.25$ , but finally concluded that Lee and Zhou's parametrization ( $C=6$ ) is more suitable for neutron source applications, and we also adopted  $C=6$  in this study.

The differential cross section in the laboratory system near threshold are then calculated by

$$\left(\frac{d\sigma}{d\Omega_{cm}}\right)\left(\frac{d\Omega_{cm}}{d\Omega}\right)\left(\frac{dE_p}{dE_n}\right) = \pm \frac{AC(m_{Li}+m_p)^2(\cos\theta \pm \xi)\sqrt{m_p m_n/m_{Li}(m_{Li}+m_p-m_n)}}{(1+x)^2[m_p m_n E_p \xi(\cos\theta \pm \xi) \pm m_{Li}(m_{Li}+m_p-m_n)E_{th}]} \quad (32)$$

which is then converted into the double differential yield by Eqn. (26).

### 2.3.5. Angular integration

Figure 5 shows that the range for angular integration corresponds to the proton energy range. For example, this figure shows that we need to integrate  $d^2Y(\theta, E_n)/dE_n d\Omega$  from  $\sim 50^\circ$  to  $\sim 70^\circ$  for  $E_n = 0.1$  MeV neutrons if incident proton energy range is from 1.95 to 2.00 MeV and the angular range is also covered by the neutron activation sample. This integration can be written as

$$\frac{dY(E_n)}{dE_n} = \int d\Omega (d^2Y(\theta, E_n)/dE_n d\Omega) w_1(\theta) w_2(E_p(\theta, E_n)) \quad (33)$$

where  $w_1(\theta)$  is the weighting function originating from the solid angle covered by the neutron activation sample, while  $w_2(E_p(\theta, E_n))$  is the weighting function originating from the proton energy spread which are explained in following sub sections. Note that  $d^2Y(\theta, E_n)/dE_n d\Omega = 0$  for  $E_p(\theta, E_n) < E_{th}$ .

### 2.3.6. Weighting function $w_1(\theta)$

For a circular sample (radius R),  $w_1(\theta) = 1$  for  $\theta < \tan^{-1}(R/d)$ , otherwise =0. For a square sample (dimension L×L),

$$\begin{aligned} w_1(\theta) &= 1 \text{ for } \theta < \tan^{-1}\left[\frac{L}{2d}\right], \\ &= 1 - \left(\frac{4}{\pi}\right) \cos^{-1}\left[\frac{L}{2d \tan \theta}\right] \text{ for } \tan^{-1}\left[\frac{L}{2d}\right] < \theta < \tan^{-1}\left[\frac{L}{\sqrt{2}d}\right] \end{aligned} \quad (34)$$

= 0, otherwise.

### 2.3.7. Weighting function $w_2(E_p(\theta, E_n))$

When the spread of the proton energy extracted from the accelerator is negligible,  $w_2(E_p(\theta, E_n))=1$  for  $E_{px} < E_p < E_{p0}$ , otherwise it is equal to 0, where  $E_{p0}$  is the initial proton energy and  $E_{px}$  is the final proton energy. When the proton stops or slows down beyond the reaction threshold inside the lithium sample (thickness  $t$ ),  $E_{px}=E_{th}$ . Otherwise EPEN determines  $E_{px}$  by solving the equation  $t = R(E_{p0}) - R(E_{px})$ . The range was obtained by SRIM (Ziegler and Biersack, 2013).

This weighting function should be modified when the proton energy spread is not negligible. If the initial proton energy  $E_{p0}$  normally distributes with the mean value  $\langle E_{p0} \rangle$  and standard deviation  $\Delta E_{p0}$  according to

$$p(E_{p0}) = \frac{1}{\sqrt{2\pi\Delta E_{p0}^2}} \exp\left[-\frac{(E_{p0}-\langle E_{p0} \rangle)^2}{2\Delta E_{p0}^2}\right] \quad (35)$$

The probability to find a proton with its initial energy  $E_p$  in the lithium sample is

$$w_2(E_p(\theta, E_n)) = \int_{E_p}^{+\infty} dE_{p0} p(E_{p0}) = \left(\frac{1}{2}\right) \left[1 - \operatorname{erf}\left\{\frac{(E_p - \langle E_{p0} \rangle)}{\sqrt{2\Delta E_p^2}}\right\}\right] \quad (36)$$

In its numerical implementation, we set  $w_2(E_p(\theta, E_n)) = 0$  for  $E_p \geq E_{p0+}$  and  $=1$  for  $E_p = E_{p0-}$ , with  $E_{p0\pm} = \langle E_{p0} \rangle \pm 5\Delta E_{p0}$ . For  $E_p < E_{p0-}$ ,

1. When all protons stop in the lithium sample (i.e.  $t > R(E_{p0+})$ ,  $w_2(E_p(\theta, E_n))=1$  for  $E_{thr} < E_p < E_{p0-}$ .
2. When all protons penetrate the lithium sample (i.e.  $t < R(E_{p0-})$ ), we assume that the exit protons also distribute normally between  $E_{px+}$  and  $E_{px-}$  around  $\langle E_{px0} \rangle = (E_{px+} + E_{px-})/2$ . Therefore,

$$\begin{aligned}
w_2(E_p(\theta, E_n)) &= 1 \text{ for } E_{px+} < E_p < E_{p0-} \\
&= 1 - \left(\frac{1}{2}\right) \left[ 1 - \operatorname{erf} \left[ \frac{E_p - \langle E_{px0} \rangle}{\sqrt{2\Delta E_p^2}} \right] \right] \text{ for } E_{px-} < E_p < E_{px+} \\
&= 0 \text{ for } E_{thr} < E_p < E_{px-}
\end{aligned} \tag{37}$$

3. When a part of protons penetrate the lithium sample,  $\langle E_{px0} \rangle =$

$$\begin{aligned}
(E_{thr} + E_{px+})/2; w_2(E_p(\theta, E_n)) &= 1 \text{ for } E_{px+} < E_p < E_{p0-} \\
&= 1 - \left(\frac{1}{2}\right) \left[ 1 - \operatorname{erf} \left[ \frac{E_p - \langle E_{px0} \rangle}{\sqrt{2\Delta E_p^2}} \right] \right] \text{ for } E_{thr} < E_p < E_{px+}
\end{aligned} \tag{38}$$

where  $E_{px\pm}$  satisfies  $t = R(E_{p0\pm}) - R(E_{px\pm})$ .

## 2.4. Results and Discussion

### 2.4.1. Comparison with experimental neutron spectra

A typical application of the  ${}^7\text{Li}(p,n){}^7\text{Be}$  neutron source reaction near the threshold is imitation of stellar neutrons thermally equilibrated to  $kT \sim 25$  keV. In order to examine our approach near threshold, we compare our thick target  ${}^7\text{Li}(p,n_0){}^7\text{Be}$  neutron spectrum ( $E_p = 1912 \pm 0$  keV) for the lithium sample (100  $\mu\text{m}$  thick, i.e., thicker than the full stopping length) with those measured by Lederer *et al.*, 2012 ( $E_p = 1912 \pm 1.2$  keV), Ratynski *et al.*, 1988 ( $E_p = 1912$  keV), and Feinberg *et al.*, 2012 ( $E_p = 1912 \pm 1.5$  keV) in Figure 7 (The values following  $\pm$  give energy spread hereafter). We refer the lithium target as thick (thin) if the lithium thickness is thicker (thinner) than the full stopping length of the incident protons. These experimental data sets were retrieved from the EXFOR library (Otuka *et al.*, 2014).

Our results as well as the experimental results are the angular integrated neutron spectra up to the laboratory maximum neutron emission angle of 63 degrees determined by the two-body kinematics (c.f. Figure 5). For comparison, the neutron spectra are normalized such that the total neutron yield is 1.0. Our result agrees with the measured spectra except for broader low- and high- energy tail observed by Feinberg *et al.*, 2012 which explain the deviation is due to the relatively thick  ${}^6\text{Li}$ -glass detector and its effects on the time-of-flight resolution.

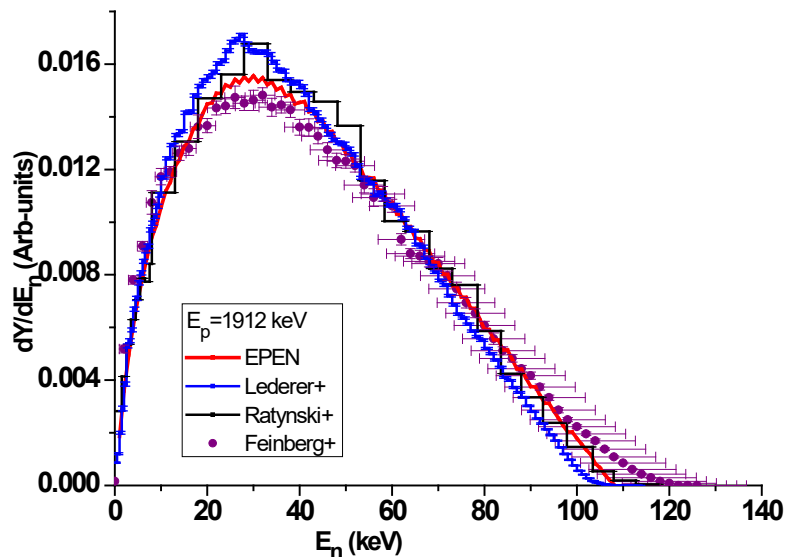


Figure 7: Comparison of EPEN  ${}^7\text{Li}(p,n){}^7\text{Be}$  neutron energy spectrum at  $E_p=1912 \pm 0$  keV with experimental results (Lederer *et al.*, 2012; Ratynski *et al.*, 1988; Feinberg *et al.*, 2012) for a thick natural lithium target.

Figure 8 shows comparison between our result and Kononov *et al.*'s experimental result (Kononov *et al.*, 1977) of zero degree neutron yield for  ${}^7\text{Li}(p,n){}^7\text{Be}$  reaction near threshold, for a thick lithium target. The incident proton energy of the experimental result is not explicitly written in the article, but we assume  $E_p=1940$  keV in our calculation following private communication with the author (Kononov, 2016). Figure 8 show that there is a



mismatch of the peak position by 5 keV between EPEN and Kononov *et al.* experimental zero degree neutron yield. Furthermore, EPEN underestimates the experimental result throughout the whole energy range as long as we do not consider the finite detector solid angle, which is not reported by Kononov *et al.* (Kononov *et al.*, 1977).

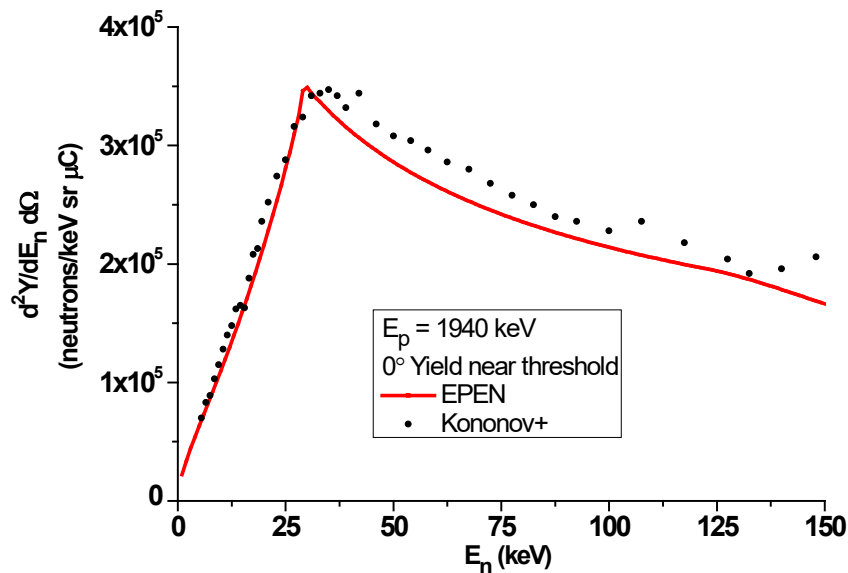


Figure 8: Comparison of EPEN  ${}^7\text{Li}(p,n_0){}^7\text{Be}$  neutron  $0^\circ$  double differential energy spectrum at  $E_p=1940$  keV with experimental result (Kononov *et al.*, 1977; Kononov, 2016) for a thick natural lithium target.

To identify the cause of this disagreement, we calculated neutron energy spectra with various angular range covered by the detector. Figure 9 shows comparison of the results for four angular ranges ( $\pm 0$ , 3, 5, 7 and  $9^\circ$ ) with Kononov *et al.*'s experimental data. The spectra are normalized such that they have a common maximum 1 for better indication of the peak change and spectrum shape around the peak position with different angular coverage. The figure shows that the best agreement with experimental spectrum is observed when  $\pm 5^\circ$  is chosen. A wider angular range ( $\pm 9^\circ$ ) shows better agreement in the peak position, although the calculated spectrum clearly overestimates the experimental one above 30 keV.

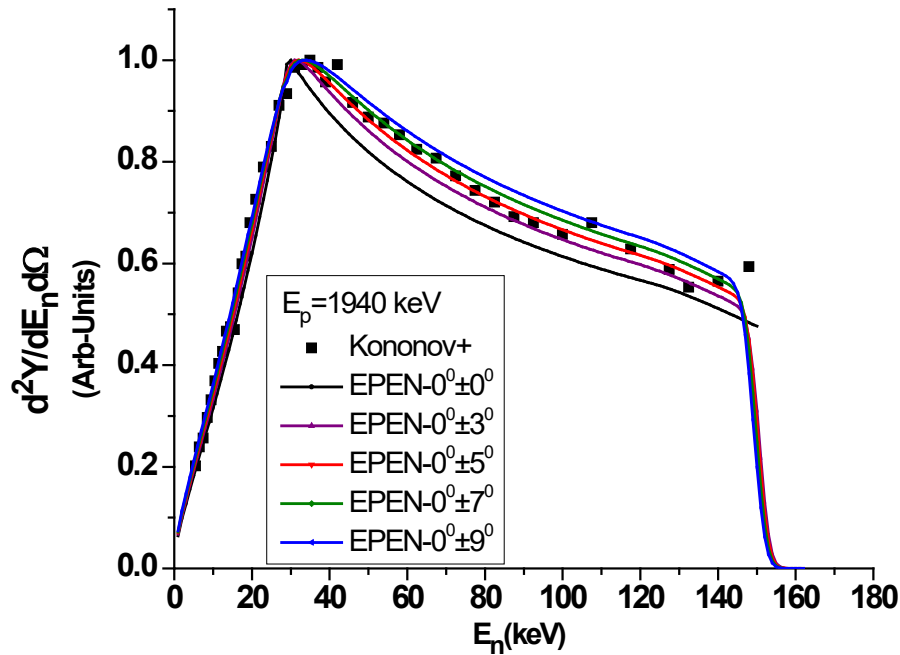


Figure 9: Comparison of EPEN  ${}^7\text{Li}(p,n){}^7\text{Be}$  double differential neutron energy spectrum at  $E_p=1940$  keV for various angular range with experimental result (Kononov *et al.*, 1977; Kononov, 2016).

To further confirm this, we also compared the calculated spectrum with Feinberg *et al.* (2012) experimental spectrum ( $E_p=1912\pm 1.5$  keV with  $0\pm 2.9^\circ$ ) in Figure 10 for a thick natural lithium target. The peak position of the calculated and experimental spectra exactly match though the calculated one overestimates the experimental one around 100 keV. Herrera *et al.* also did the same comparison for their spectrum calculated by a different approach (see Figure 11 of M.S. Herrera, 2015), and reported the same discrepancy. Friedman *et al.* also compare their calculated spectrum with the Feinberg *et al.*'s experiment in Figure 5 of (Friedman *et al.*, 2013), but the experimental spectrum ( $E_p=1912\pm 1.5$  keV with  $0\pm 2.9^\circ$ ) shown in the figure is different from the experimental spectrum compiled in EXFOR (O1983.004, data received from Feinberg in 2012).

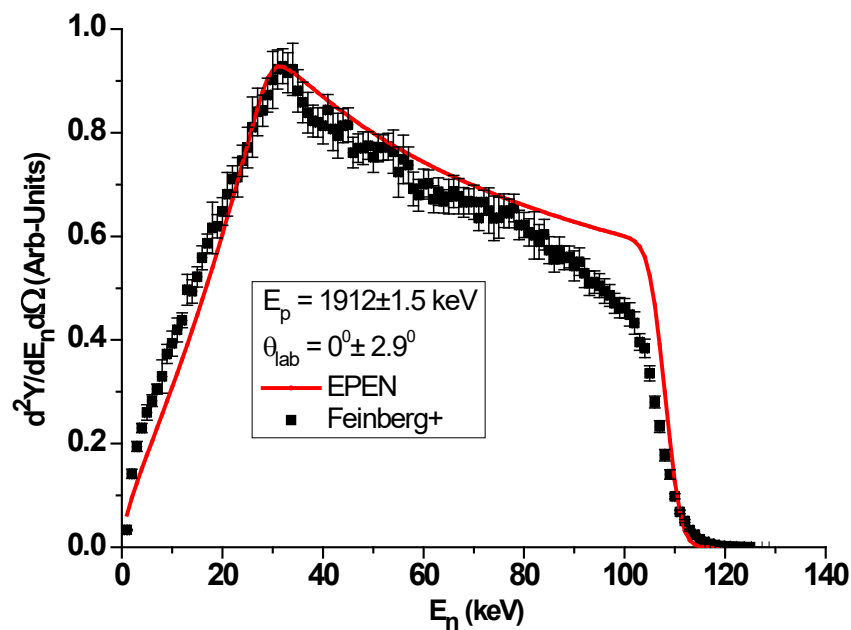
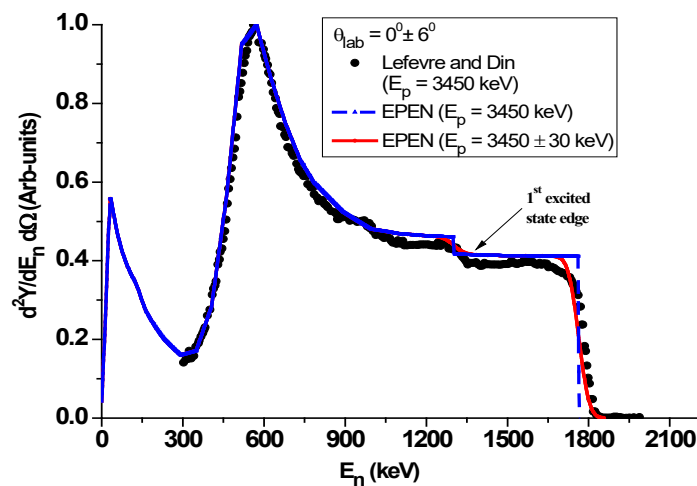


Figure 10: Comparison of EPEN  ${}^7\text{Li}(p,n_0){}^7\text{Be}$  double differential neutron energy spectrum with experimental result (Feinberg, 2012) at  $E_p=1912\pm 1.5$  keV at  $0\pm 2.9^\circ$  for a thick natural lithium target.

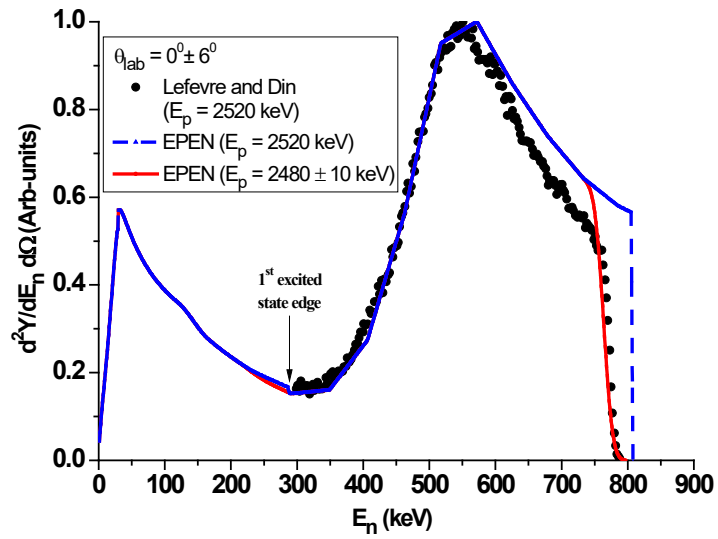
Figures 11(a) and (b) show comparison of the  $(p,n_0)$  and  $(p,n_1)$  forward direction ( $0$  deg) neutron energy spectra between the EPEN and experimental ones reported by Lefevre and Din (1969) for  $E_p = 3450$  keV and  $E_p = 2520$  keV, respectively, for a thick LiF target. Moreover, the experimental neutron spectrum is reported up to the  $\sim 300$ -keV lower boundary. The experimental angular coverage of the detector reported is  $\pm 6$  deg, which is also used in the EPEN calculation. Lefevre and Din do not specify the incident proton beam energy spread. As shown by Figure 11(a), the EPEN calculation at 3450 keV with zero beam spread for a thick LiF target, where the protons slowed down below the reaction threshold inside the lithium target, does not match the experimental higher neutron energy tail as well as the first excited state edge. The EPEN calculation with 30-keV beam energy spread well

reproduces the first excited state edge as well as the higher-energy tail of the experimental result in the case of  $E_p = 3450$  keV. At  $E_p = 2520$  keV, EPEN reproduces very well the experimental neutron spectrum below 600 keV. However, the highest neutron energy of EPEN is much higher, and it also overestimates the spectrum above 600 keV. Another EPEN calculation at  $E_p = 2480 \pm 10$  keV reproduces very well the high-energy tail of the neutron energy spectrum, while it still overestimates the spectrum above 600 keV.

Figures 12 (a) and (b) show comparison of EPEN neutron spectra with the theoretical neutron spectra reported in Table I of Ritchie (1976) at  $E_p = 2400$  and 2800 keV for a thick natural lithium target where the protons slowed down below the  $(p,n_0)$  reaction threshold inside the lithium target. The comparison in absolute units matches very well at both these energies for  $(p,n_0)$  as well as  $(p,n_1)$  neutron spectra. However, as shown in Figures 12 (a) and (b), there is a discrepancy around 100 keV where the peak of Ritchie's theoretical neutron yield is relatively higher compared to the EPEN yield. It is also worth mentioning that the multiplication factor  $10^{-2}$  given by Ritchie in Table I should be  $10^2$ , which can also be confirmed by the y-axis scale in Figure 6 of the same paper.

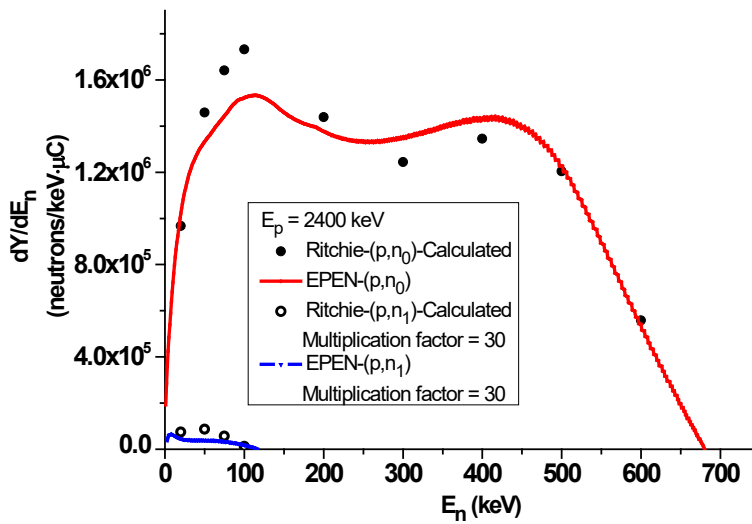


(a)

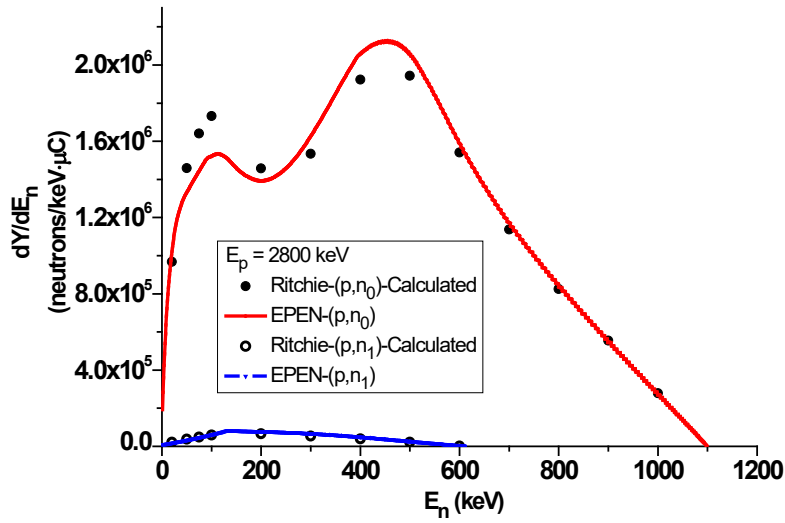


(b)

Figure 11: Comparison of differential neutron spectra of EPEN with experimental results of Lefevre and Din for (a)  $E_p = 3450$  keV and (b)  $E_p = 2520$  keV at  $0 \pm 6$  deg for a thick LiF target. For comparison, the neutron spectra are normalized such that they have a common maximum 1.



(a)



(b)

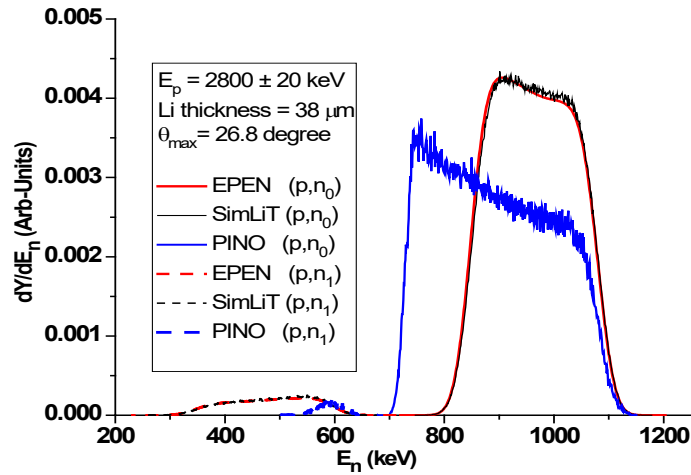
Figure 12: Comparison of angle-integrated neutron spectrum of EPEN with theoretical results of Ritchie at (a)  $E_p = 2400$  keV and (b)  $E_p = 2800$  keV for a thick natural lithium target. In (a), the  $(p,n_1)$  neutron spectra of Ritchie and EPEN are multiplied by 30 for better visibility.

#### 2.4.2. Comparison with SimLiT and PINO

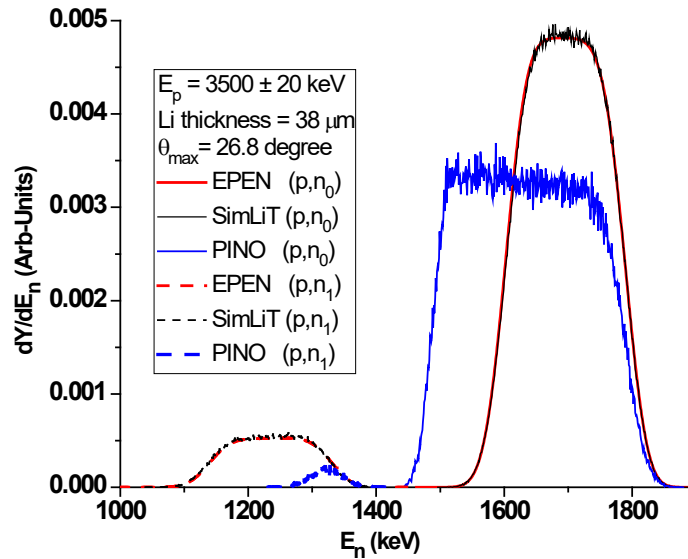
PINO (Protons In Neutrons Out) (R. Reifarh *et al.*, 2016) and SimLiT (Friedman *et al.*, 2013) are Monte-Carlo based programs, which allow the simulation of neutron spectra from  ${}^7\text{Li}(p,n){}^7\text{Be}$  reaction considering the geometry of the setup and the proton-energy spread. We compare our results with those obtained by SimLiT and PINO at two incident proton energies 2800 keV and 3500 keV with two beam energy spread, 0 keV and 20 keV for lithium targets thicker and thinner than the proton range. In all the results reported here, the proton beam size is treated as negligible. Monte-Carlo simulations were performed for 100 nC protons for SimLiT, and 10 million protons (maximum number allowed by the web interface) for PINO.

Figures 13 (a) and (b) show comparison between EPEN, SimLiT and PINO ( $p,n_0$ ) and ( $p,n_1$ ) neutron energy spectra for  $E_p=2800\pm 20\text{keV}$  and  $E_p=3500\pm 20\text{keV}$  respectively. The configurations used in EPEN, SimLiT and PINO are similar. A natural lithium target thickness is  $38\ \mu\text{m}$ , a square shape neutron activation sample foil ( $10\times 10\ \text{mm}^2$ ) is placed at a distance  $14\ \text{mm}$  from the lithium target in the beam direction. The maximum sample angular coverage is  $26.8^\circ$  in this geometry. In the present work, the natural lithium density adopted is  $0.534\ \text{g/cm}^3$ . For comparison, the EPEN, SimLiT and PINO spectra are normalized such that the  $(p,n_0)+(p,n_1)$  total neutron yield is equal to 1. These figures show that there is a perfect match between EPEN and SimLiT neutron energy spectra for both ( $p,n_0$ ) and ( $p,n_1$ ) contributions. However, the PINO shows large discrepancy from the other two codes for both ( $p,n_0$ ) and ( $p,n_1$ ) contributions. EPEN reproduces the ( $p,n_0$ ) contribution calculated by PINO if there is no proton energy spread, which implies a problem in treatment of proton energy spread in PINO. It is also worth mentioning that EPEN can reproduce the PINO ( $p,n_0$ ) spectrum in figures 13 (a) and (b) if the necessary weighting function described in Section 2.3.7. is ignored.

Similarly, a perfect match between EPEN and SimLiT ( $p,n_1$ ) spectra is observed, whereas, there exist large discrepancy of PINO ( $p,n_1$ ) result from the other two results. A much sharper ( $p,n_1$ ) spectrum predicted by PINO shows as if the lithium target thickness is thinner than the given one.



(a)



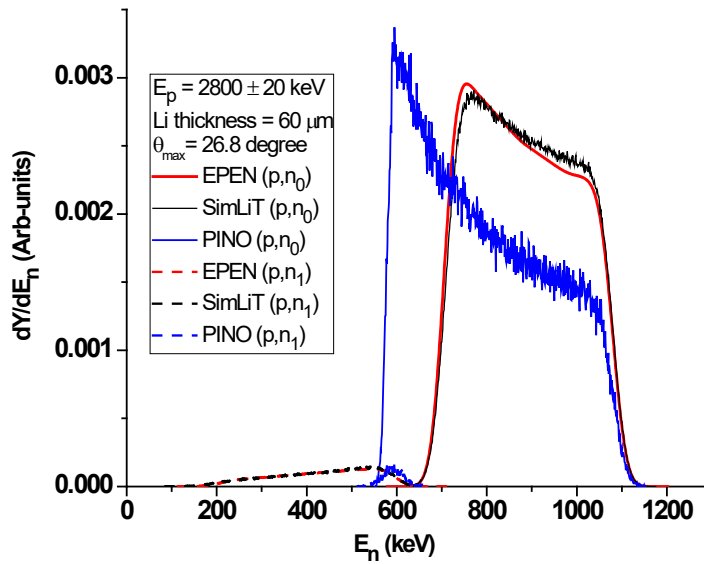
(b)

Figure 13: Comparison between EPEN, SimLiT and PINO neutron energy spectra for thin lithium target thickness 38  $\mu\text{m}$  at (a)  $E_p = 2800 \pm 20 \text{ keV}$  and (b)  $E_p = 3500 \pm 20 \text{ keV}$ .

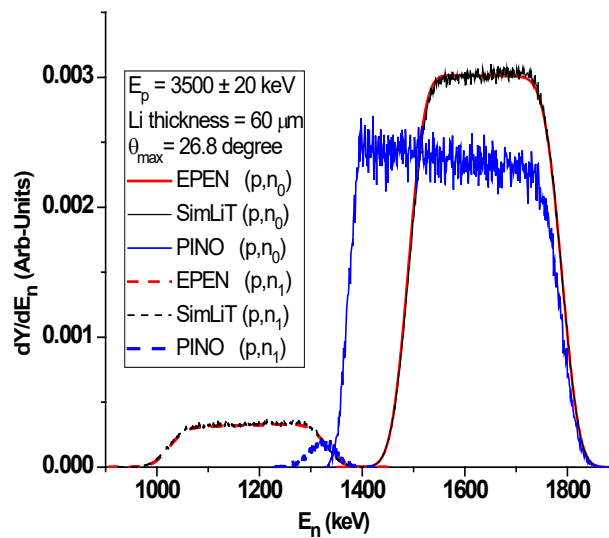
Figures 14 (a) and (b) show comparison between EPEN, SimLiT and PINO ( $p, n_0$ ) and ( $p, n_1$ ) neutron energy spectra for  $E_p = 2800 \pm 20 \text{ keV}$  and  $E_p = 3500 \pm 20 \text{ keV}$  respectively. All other configurations are the same as in Figures 13 (a) and (b) except that the thickness of natural lithium is now 60  $\mu\text{m}$ . Again for comparison, we normalized EPEN, SimLiT and



PINO spectra such that the  $(p,n_0)+(p,n_1)$  total neutron yield is equal to 1. The same arguments and conclusions can be drawn similar to Figures 13 (a) and (b). It is worth mentioning that the PINO neutron energy range in the case of  $(p,n_1)$  spectra remains the same even if the lithium thickness is increased for a given incident energies, and similar configurations.



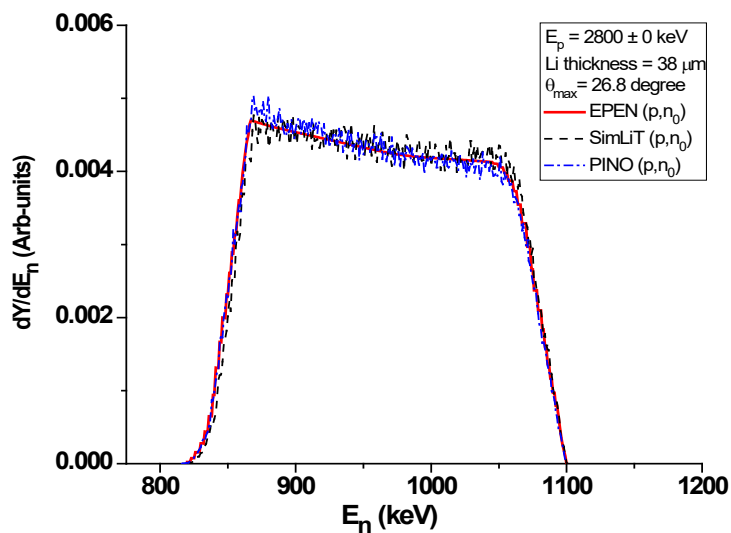
(a)



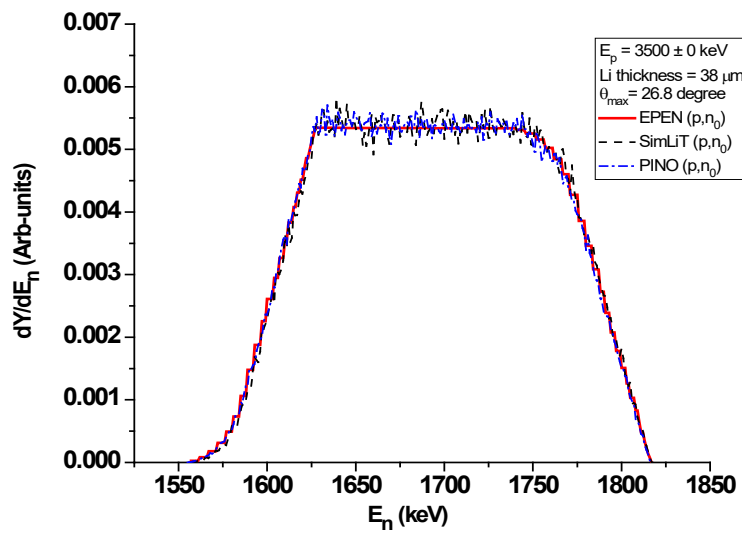
(b)

Figure 14: Comparison between EPEN, SimLiT and PINO neutron energy spectra for thin lithium target thickness 60  $\mu\text{m}$  at (a)  $E_p = 2800 \pm 20$  keV and (b)  $E_p = 3500 \pm 20$  keV.

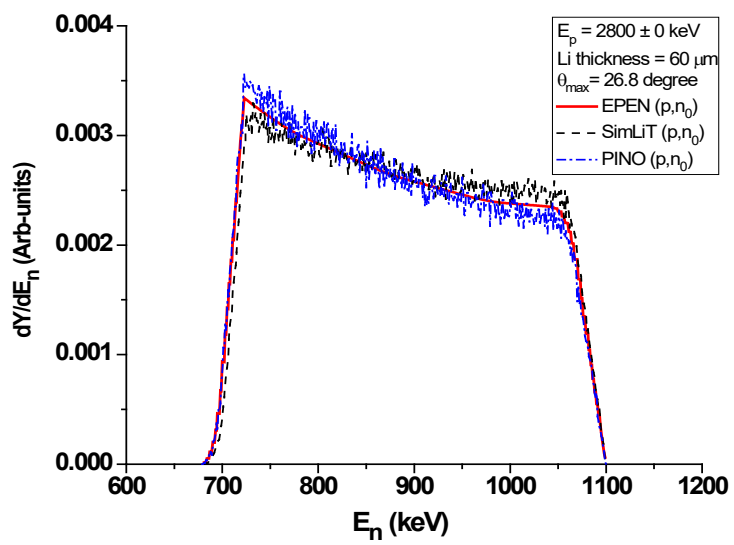
Figures 15 (a-d) show comparison between EPEN, SimLiT and PINO ( $p, n_0$ ) neutron energy spectra for  $E_p = 2800$  keV and  $E_p = 3500$  keV with negligible proton energy spread. We observed perfect match between all the results. This clearly shows that there is a serious problem in PINO simulation when it considers finite beam energy spread as shown in Figures 13 and 14. EPEN and SimLiT assume a normal distribution of incident proton energy when the energy spread is specified (See Section 2.4.7. for the treatment of the energy spread in EPEN) while the procedure is not clear for PINO (Reifarth *et al.*, 2016).



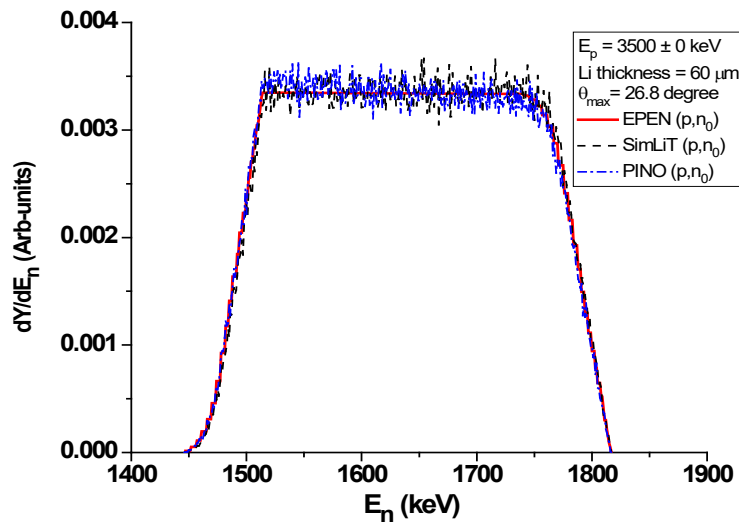
(a)



(b)



(c)



(d)

Figure 15: Comparison between EPEN, SimLiT and PINO ( $p, n_0$ ) neutron energy spectra for zero proton beam energy spread at (a)  $E_p = 2800$  keV and thin lithium target thickness 38  $\mu\text{m}$ , (b)  $E_p = 3500$  keV and thin lithium target thickness 38  $\mu\text{m}$ , (c)  $E_p = 2800$  keV and thin lithium target thickness 60  $\mu\text{m}$  (d)  $E_p = 3500$  keV and thin lithium target thickness 60  $\mu\text{m}$ . SimLiT always requires finite proton energy spread, and we set it to 0.1 keV instead of 0 keV.

**CHAPTER – 3**  
**EXPERIMENTAL DETAILS**

We measured the neutron capture cross section on  $^{70}\text{Zn}(n,\gamma)^{71}\text{Zn}^m$  reaction using standard activation technique. The experiment was carried out at the Folded Tandem Ion Accelerator (FOTIA) Facility, Nuclear Physics Division, Bhabha Atomic Research Centre (BARC), Mumbai. The energies of proton beam used in the experiment were 2.25 MeV and 2.60 MeV with energy spread of  $\pm 0.02$  MeV.

### 3.1. Neutron Source

The neutron beam required for the experiment was obtained from the  $^7\text{Li}(p,n)^7\text{Be}$  reaction. The thickness of the lithium targets used for irradiations at 2.25 and 2.60 MeV proton energies were 2.0-mg/cm<sup>2</sup>-(37.4- $\mu\text{m}$ ) and 2.5-mg/cm<sup>2</sup>-(46.8- $\mu\text{m}$ ) respectively. The proton beam current during irradiation varied from 50 to 100 nA, and the beam diameter on the lithium target was about 5 mm. The lithium foil was pasted on a 0.25-mm-thick tantalum foil (manufactured by Goodfellow Cambridge Limited, United Kingdom and supplied by H. Fillunger & Co. Pvt. Ltd., Bangalore) in order to stop the proton beam. The neutron flux was monitored online by a NE213 neutron detector at 0° and at 1-m distance from the lithium target. The neutron flux was recorded and saved every 30 min to get the neutron flux fluctuation during the whole irradiation period.

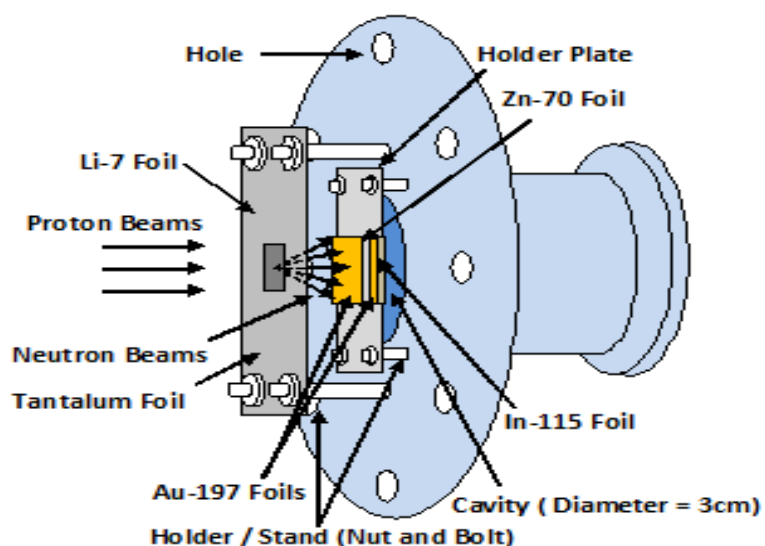


Figure 16: The schematic diagram of the Experimental Setup.



Figure 17: NE213 neutron detector at zero degree kept at 1 m distance from the lithium target.

Since the time-of-flight and multiple foil activation techniques cannot be applied at BARC-FOTIA due to the continuous beam structure and weak neutron flux, the neutron energy spectrum code - EPEN was used to calculate the neutron energy spectra of the  ${}^7\text{Li}(p,n){}^7\text{Be}$  reaction. The neutron flux energy spectra calculated by EPEN at proton energies

$2.25 \pm 0.02$  MeV and  $2.60 \pm 0.02$  MeV are shown in Figure 18 and Figure 19 respectively. The input parameters in the present work for 2.25 MeV and 2.60 MeV are (Energy = 2250; Energy Sigma = 20; Type = Li; Thickness = 37.4; Distance to Lithium = 1.4; Shape = Square; Half Width = 0.5) and (Energy = 2600; Energy Sigma = 20; Type = Li; Thickness = 46.8; Distance to Lithium = 1.4; Shape = Square; Half Width = 0.5).

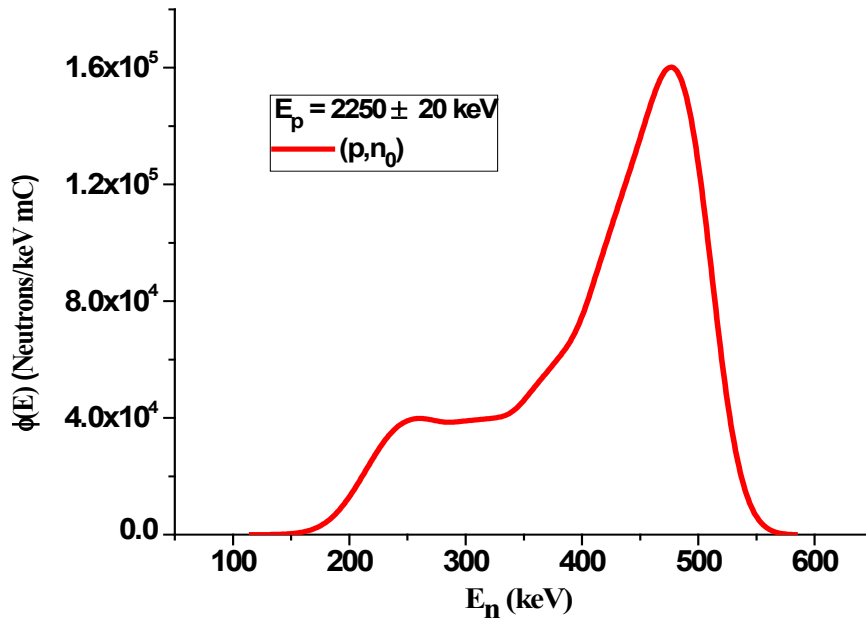


Figure 18: Neutron flux energy spectrum  $\phi(E)$  from the  ${}^7\text{Li}(p, n_0){}^7\text{Be}$  reaction at  $E_p = 2.25 \pm 0.02$  MeV obtained from the code EPEN.



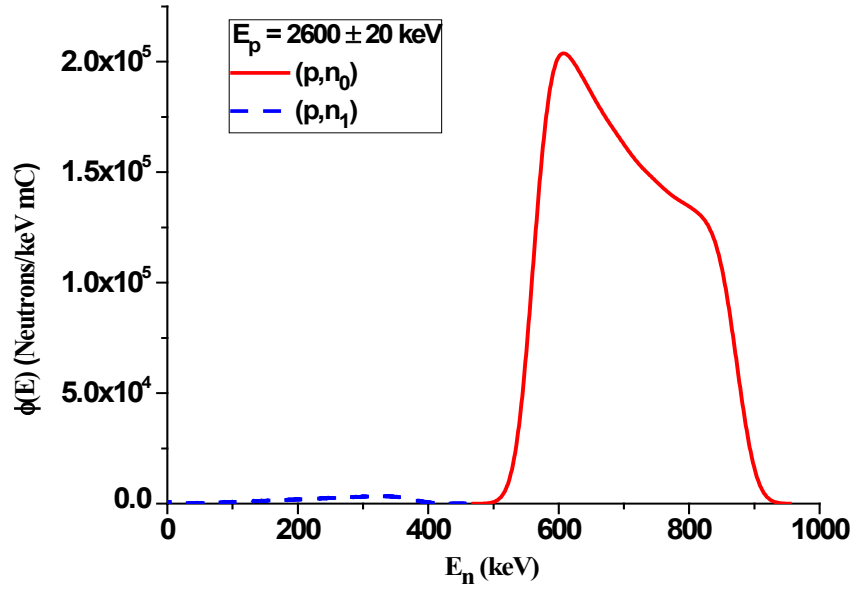


Figure 19: Neutron flux energy spectrum  $\phi(E)$  from the  ${}^7\text{Li}(p,n_0){}^7\text{Be}$  and  ${}^7\text{Li}(p,n_1){}^7\text{Be}$  reaction at  $E_p = 2.60 \pm 0.02 \text{ keV}$  obtained from the code EPEN.

The mean energy of the  $(p,n_0)$  neutron group was obtained using the equation

$$\langle E_n \rangle = \frac{\int \phi_0(E) E dE}{\int \phi_0(E) dE} \quad (39)$$

with the EPEN  $(p,n_0)$  neutron flux energy spectrum  $\phi_0(E)$  and it is  $0.40 \pm 0.15 \text{ MeV}$  and  $0.70 \pm 0.10 \text{ MeV}$  for  $E_p = 2.25$  and  $2.60 \text{ MeV}$  respectively. EPEN is available online (<http://www.epen.nhergmzu.com/epen/>), and the numerical neutron energy spectra can also be downloaded from the web page.

### 3.2. Sample preparation

An enriched zinc foil ( $72.4 \pm 1.0\%$ ) to  ${}^{70}\text{Zn}$  (manufactured by FUSE “Integrated Plant Electrohimpribor,” Russia and supplied by AMT Ventures Pvt. Ltd.) was sandwiched between gold foils (manufactured by Goodfellow Cambridge Limited, United Kingdom and supplied by H. Fillunger & Co. Pvt. Ltd., Bangalore). The gold foils were used for

normalization of the measured cross section with the  $^{197}\text{Au}(n,\gamma)^{198}\text{Au}$  reaction as standard cross section. Another natural indium foil (provided by BARC) was stacked at the end of the foil stack to serve as an independent flux monitor foil using the  $^{115}\text{In}(n,n')^{115}\text{In}^m$  reaction for cross-checking. The whole stacked foils ( $10 \times 10 \text{ mm}^2$ ) were then wrapped with a 0.025-mm-thick super pure aluminum foil. The Au-Zn-Au-In stack was mounted at  $0^\circ$  with respect to the beam direction at a distance of 14 mm from the lithium target. All foils were weighted at TIFR with an accuracy of 0.1 mg. Details about the foils used in the experiment are given in Table 2.

**TABLE 2:** Details of foils used in the present experiment.

Isotope	Enrichment (%)	Purity (%)	$E_n$ (MeV)	Thickness ( $\text{mg}/\text{cm}^2$ )
$^{70}\text{Zn}$	72.4±1.0	>99.97	0.40	113.6±0.1
	8.49 ( $^{64}\text{Zn}$ )			
	8.40 ( $^{66}\text{Zn}$ )		0.70	113.6±0.1
	2.01 ( $^{67}\text{Zn}$ )			
8.70 ( $^{68}\text{Zn}$ )				
$^{197}\text{Au}$	100%	99.95	0.40	54.2±0.1 (front)
				52.6±0.1 (back)
			0.70	72.3±0.1 (front)
				68.5±0.1 (back)
$^{115}\text{In}$	95.71%	99.99	0.40	129.8±0.1
			0.70	129.8±0.1

### 3.3. Measurement of $\gamma$ -ray activity

The foil stack was transferred to the counting room after the completion of the neutron irradiation and sufficient cooling. For each incident energy, the activities of the stacks of the foils were counted together, not the individual foils separately. Then gamma-ray activity counting was done using a precalibrated lead-shielded 185-cc high-purity germanium (HPGe) detector having 30% relative efficiency and 1.8-keV energy resolution at 1.33-MeV gamma energy. The data acquisition was carried out using CAMAC-based LAMPS (Linux Advanced Multiparameter System) software (TCAMCON-95/CC 2000 crates controller and CM-48 ADCs). Therefore, the dead time of the detector was negligible. The decay curve analysis was carried out by saving the gamma count periodically. This procedure helped in correct identification of the gamma ray of interest. Details of decay data adopted in the analysis are given in Table 3. The irradiation, cooling and counting times are presented in Table 4.

**TABLE 3:** Decay data adopted in the present work taken from the ENSDF library (Abusaleem et al., 2011; Huang Xiaolong, 2009; Blachot, 2012).

Nuclide	Half-life	$E_\gamma$ (keV)	$I_\gamma$ (%)
$^{71}\text{Zn}^m$	$3.96 \pm 0.05\text{h}$	386.280	$91.40 \pm 2.10$
$^{198}\text{Au}$	$2.6947 \pm 0.0003\text{d}$	411.802	$95.62 \pm 0.06$
$^{115}\text{In}^m$	$4.486 \pm 0.004\text{h}$	336.240	$45.80 \pm 2.20$

**TABLE 4:** Irradiation, cooling and counting times.

$E_n$ (MeV)	Irradiation time (sec.)	Run No.	Cooling time (sec.) (beam stop time - counting start time)	Counting time (sec.)
0.40	14760.0	1	2428.0	3776.7
		2	6210.7	7232.1
		3	13450.8	7216.7
		4	20674.5	7306.3
		5	27989.8	7235.1
		6	35233.9	2551.8
0.70	18924.0	1	1127.0	1983.7
		2	3115.7	1804.9
		3	6623.0	1804.4
		4	8434.4	1760.6
		5	10381.0	3599.9
		6	13987.9	3600.0

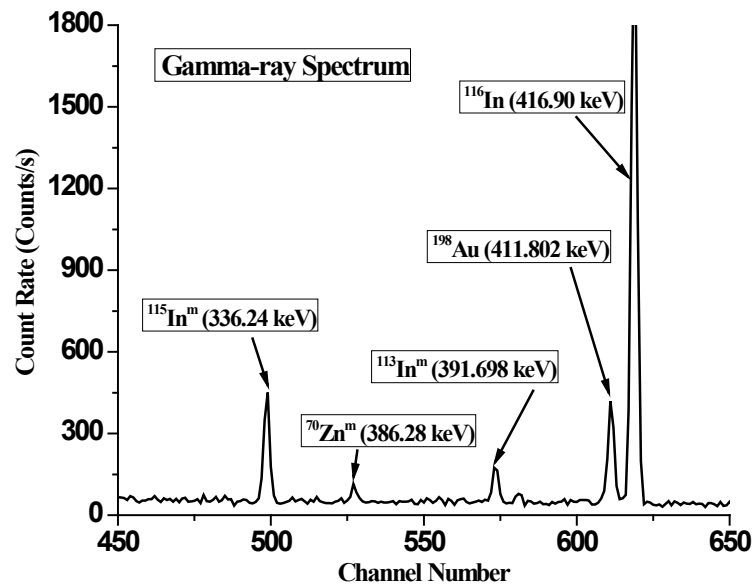


Figure 20: Typical  $\gamma$ -ray spectrum of radioactive nuclides  $^{115}\text{In}^m$ ,  $^{71}\text{Zn}^m$  and  $^{198}\text{Au}$  at  $\langle E_n \rangle = 2.6$  MeV.

### 3.4. Calibration of HPGe detector

The detection efficiency is a measure of the percentage of radiation that a given detector detects from the overall yield emitted from the source. It can vary with the volume and shape of the detector material, absorption cross section in the material, attenuation layers in front of the detector, and distance and position from the source to the detector.

The detector efficiency depends on different parameters and thus various kinds of the efficiency definitions are used to cover those parameters.

(i) Absolute total efficiency: Especially in the radioactivity measurement the absolute efficiency of the detector must be known. It is defined as the ratio of the number of counts recorded by the detector ( $N_c$ ) to the number of radiation ( $N_s$ ) emitted by the source in all directions as represented in the following formula:

$$\varepsilon_{abs} = \frac{N_c}{N_s} \quad (40)$$

(ii) Intrinsic efficiency: It is the ratio of the number of pulses recorded by the detector to the number of gamma rays hitting the detector i.e., the fraction of gamma rays recorded in the net full energy peak to the number incident on the detector. This efficiency is independent of source/detector geometry.

(iii) Absolute full-energy peak (or photo-peak) efficiency: It is the efficiency for producing full-energy peak pulses only, rather than a pulse of any size, for the gamma ray. It depends on geometrical arrangement of source and detector. This parameter is of most significance in practical gamma-spectroscopy.

The photon radiations of  $^{152}\text{Eu}$  cover the energy range of our interest and it also provide the highest possible accuracy. Therefore, a  $^{152}\text{Eu}$  point source ( $T_{1/2} = 13.517$  years,

Martin, 2013) of known activity ( $A_0 = 7582.5$  Bq on 1 Oct. 1999) was used for determination of the absolute photopeak efficiency of the HPGe detector at various characteristic gamma energies of the point source. The characteristics of the  $^{152}\text{Eu}$  point source used in the experiment are given in Table 5.

**TABLE 5:** Characteristics of the  $^{152}\text{Eu}$  point source.

Isotope	Activity on Reference Date [DPS]	Activity Measurement on Date (24.2.2013)[DPS]	Reference Date	Half-life [ $t_{1/2}$ years]
$^{152}\text{Eu}$	7582.5	3733.17	1.10.1999	$13.517 \pm 0.014$

The spectrum obtained demonstrates that the  $^{152}\text{Eu}$  source was a long-lived multi gamma-ray emitter with gamma-rays being emitted over a wide range of energies. This spectrum emphasizes the capability of the HPGe detector to measure complex spectra and to distinguish between very close energy lines, in the limits of the values for the energy resolutions. The detection efficiency for the point source placed at a distance of 1 cm from the detector  $\varepsilon_p$  was determined by

$$\varepsilon_p = \varepsilon_I \varepsilon_G = \frac{CK_c \varepsilon_G}{A_0 e^{-\lambda t} \Delta I_\gamma} \quad (41)$$

where  $\varepsilon_I$  is the intrinsic detection efficiency,  $\varepsilon_G$  is the geometric efficiency depending on the distance and shape of the source), and  $\Omega$  is solid angle for a point source located along the axis of a right circular cylindrical detector.

Since the count rate from the  $^{70}\text{Zn}(n,\gamma)^{71}\text{Zn}^m$  reaction is rather low, we needed to place the foil stack very close to the detector to obtain a high count rate. Therefore, the

efficiency calibration source also had to be placed at the same distance, which is 1 cm from the detector. However, this introduces the coincidence-summing effect. Evaluations of the coincidence summing effect and detection efficiency are discussed in the following sections. All the parameters independent of gamma energies are finally canceled because we need only the ratio of detection efficiencies in the determination of the cross sections.

### 3.4.1. Intrinsic Efficiency

Intrinsic efficiency is defined as the probability that a ray incident on an infinite-area flawless crystal is registered in the full energy peak. At a given energy this probability is a function only of detector thickness and it approaches unity as the thickness increases (Michael G. Strauss *et al.*, 1977). It is also defined as the number of events detected in the total absorption peak over the total number of events impinging on the detector's window (or wall). It depends on several variables like the gamma energy, the detector characteristics (dimensions, shape, material, etc) and the source's relative placement. The peak efficiency of a system consisting of a source placed inside an infinite detector would be unity, because eventually all energy would be absorbed by the detector. Real systems almost never meet these requirements, but high peak efficiencies can still be obtained. Not all gammas will see the full detector thickness and this effect will be less and less important as the source is placed further away from the detector (Peralta, 2004). The detection efficiency depends mainly on the intrinsic factors characteristic of the detector and on the solid angle  $\Omega$  under which the source is seen by the detector. The intrinsic efficiency is represented by Eqn. (42) as:

$$\varepsilon_I = \frac{CK_c}{A_0 e^{-\lambda t} \Delta I_\gamma} \quad (42)$$

where  $C$  is the number of counts during the counting time ( $\Delta t = 3607$  sec),  $A_0$  is the  $^{152}\text{Eu}$  source activity at the time of manufacture,  $t$  is the time elapsed from the date of manufacturer to the start time of counting,  $\lambda$  is the decay constant,  $I_\gamma$  is the decay gamma intensity,  $K_C$  is the correction factor for the coincidence summing effect.

### 3.4.2. Geometric Efficiency

For an arbitrary detector and isotropic point source the geometric acceptance can be defined as the fraction of solid angle subtended by the detector at the source position (Peralta, 2004)

$$\varepsilon_G = \frac{1}{4\pi} \int d\Omega = \frac{1}{4\pi} \int_A \frac{\vec{r} \cdot \vec{n}}{r^3} dA \quad (43)$$

where  $\vec{n}$  is a unitary vector perpendicular to the detector surface at each point and  $\vec{r}$  the vector linking the point source to a detector elementary area  $dA$ . For an extended source an extra integration must be carried out to cover all source points. For a cylindrical detector with a window of radius  $r$  and a point source located in the symmetry axis at a distance  $d$  from the detector, the solid angle can be computed as shown in Figure 21.

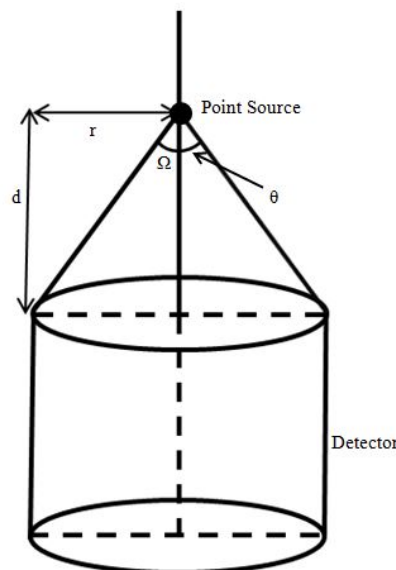




Figure 21: Geometric arrangement of  $^{152}\text{Eu}$  point source.

$$\Delta\Omega = \int_0^{2\pi} d\phi \int_{\cos\theta}^1 d(\cos\theta') = 2\pi(1 - \cos\theta) \quad (44)$$

where

$$\tan\theta = \frac{r}{d} \text{ and } \cos\theta = \frac{1}{\sqrt{\tan^2\theta + 1}} = \frac{d}{\sqrt{r^2 + d^2}}$$

Therefore, the solid angle and geometric efficiency can then be written as,

$$\Delta\Omega = 2\pi \left( 1 - \frac{d}{\sqrt{r^2 + d^2}} \right) \quad (45)$$

$$\varepsilon_G = \frac{\Delta\Omega}{4\pi} = \frac{1}{2} \left( 1 - \frac{d}{\sqrt{r^2 + d^2}} \right) \quad (46)$$

### 3.5. Coincidence summing effect

When two gamma rays emitted in a cascade are detected within the resolving time of the detector, it becomes impossible for the detector to distinguish between the two gamma rays. Therefore, instead of two signals, a single signal is observed in the spectrum as if a single gamma ray had been detected. This condition is known as “cascade” or “true coincidence” summing. This leads to

(1) a loss in count (“summed out”) from the peaks corresponding to two gamma rays.

(2) an addition of count (“summed in”) at the sum of two energies.

For any source-to-detector distance, there will be some degree of summing depending on the detector size, beyond a certain distance; coincidence-summing losses will be negligible.

A simplified decay scheme for Eu-152 is depicted in Figure 21. There are two possible modes of decay for the atoms of this nuclide:

(1) they can either emit  $\beta^-$  - particle and form Gd-152 (27.92% of events) and the daughter nucleus de-excites by emitting a number of gamma-rays.

(2) they can capture electron to form Sm-152 (72.08% of events) and the daughter nucleus de-excites by emitting a number of gamma-rays.

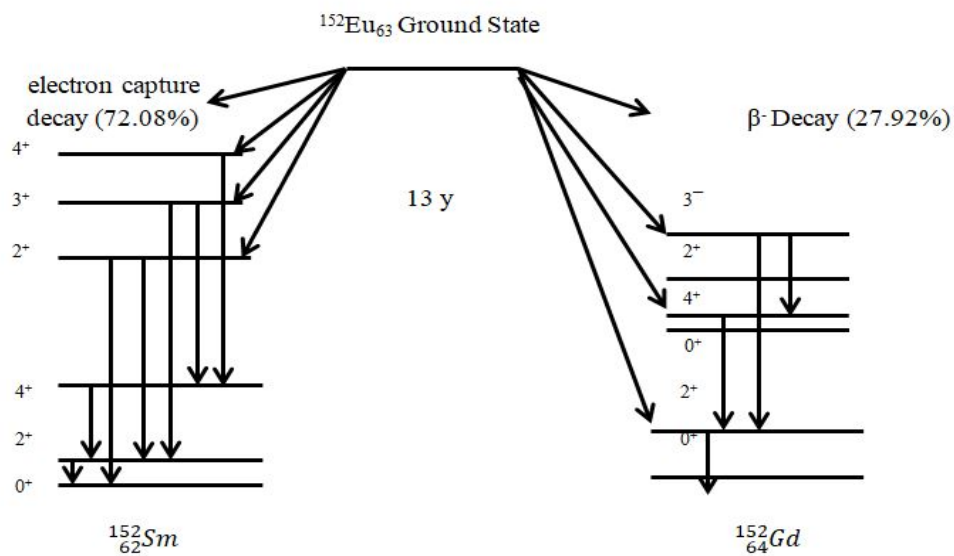


Figure 22: Simplified decay scheme for  $^{152}\text{Eu}$ .

The electron capture decay to Sm-152 is to be coupled with the emission of Sm X-rays. The individual nuclear levels have short lifetimes, which are much shorter than the resolving time of the gamma spectrometer system. Each disintegration of a Eu-152 atom in the source releases a number of gamma-rays, possibly X-rays, simultaneously. For the detector, there is a certain probability that more than one of these will be detected together. In that case, the recorded pulse represents the sum of the energies of the two individual photons. This phenomenon is True coincidence summing (TCS), i.e. it is the summing of two gamma-rays emitted in coincidence (Damon, 2005).

The probability that two gamma rays will be detected together decreases with increasing distance between the source and the detector. Thus, for the probability of two gamma rays reaching the detector at the same time to be negligible, the sample should be counted far from the detector so that the coincidence summing corrections can be avoided. But this method is impracticable for samples with low activity where the samples are required to be counted as close as possible to the detector. In the present experiment, the count rate from the  $^{70}\text{Zn}(n,\gamma)^{71}\text{Zn}^m$  reaction is very low. Therefore, to obtain high count rate, the foil stack was placed close to the detector. To avoid coincidence summing corrections in such cases, a gamma ray standard,  $^{152}\text{Eu}$ , has to be used as a monitor. To prove the evidence for coincidence summing, the sum peaks in the  $^{152}\text{Eu}$  standard source spectrum is shown in Figure 23. The indicated photo-peaks from Figure 23 correspond to the combination of gamma-ray lines are given in Table 6.

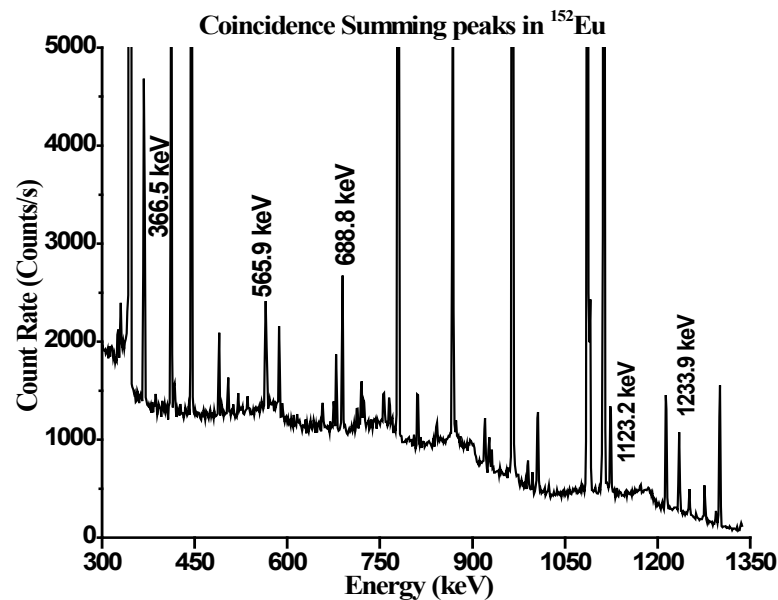


Figure 23: Sum peaks in the  $^{152}\text{Eu}$  standard source spectrum due to coincidence summing.

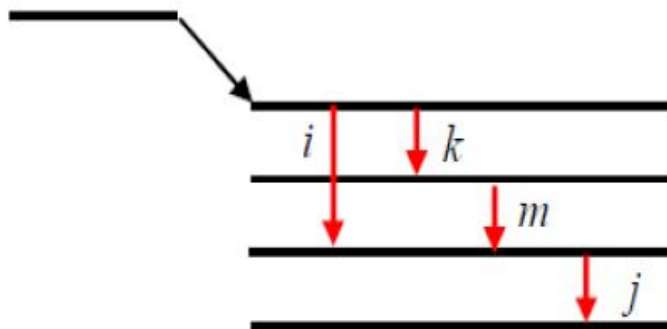


Figure 24: Example of cascade decay scheme. Coincident emission of the photons (i-j ),

(k-m), (k-j ) and (m-j ).

**TABLE 6:** Combinations of gamma-ray energies (keV) of the  $^{152}\text{Eu}$  standard source that undergo coincidence summing. The yellow boxes indicate those peaks that undergo summing in and those blue boxes, summing out.

Coincidence Summing Out/In on Eu - 152				
keV	121.8	244.7	344.3	444.1
244.7	366.5			
444.1	565.9			
778.9			1123.2	
867.4		1112.1		
964.0	1085.8			1408.1
1085.8				
1112.1	1233.9			
1408.0	1529.8			

### 3.5.1. Software for Correction of TCS (EFFTRAN)

EFFTRAN is a Monte Carlo efficiency transfer code for gamma-ray spectrometry (Vidmar, 2005). Table 7 shows the  $^{152}\text{Eu}$  standard source characteristic gamma energies and their corresponding gamma intensities considered in the detector efficiency measurement. EFFTRAN was used to calculate the correction factor  $K_c$  to correct the measured efficiency for the coincidence-summing effect. A detailed specifications of the HPGe detector (e.g., dimensions and materials of the crystal, crystal hole cavity, end cap, window, mount cup, and absorber) and the  $^{152}\text{Eu}$  gamma source (e.g., dimension, material, and characteristic gamma and X-rays) were provided as inputs to the simulation. Thus, the simulation takes care of  $\gamma$ -ray- $\gamma$ -ray,  $\gamma$ -ray-X-ray, and X-ray-X-ray coincidences. The detector efficiencies with and without the correction measured at the characteristic gamma energies of the  $^{152}\text{Eu}$  point source are shown in Figure 21. All characteristic gamma lines are affected by the summed out effect whereas only those with higher energies are affected by the summed in effect as shown in Table 7 where the gamma rays with lower energies in general have larger correction factors because the loss of their counts due to the summed out effect is not or less compensated by the summed in effect. Only the efficiency ratio is necessary for determination of the cross sections, and therefore only the uncertainties in counting statistics and gamma intensity were considered in the error propagation to the efficiencies of the  $^{71}\text{Zn}^m$  and  $^{198}\text{Au}$  characteristic gamma-lines. Since the calibration of the HPGe detector was carried out with the point source while the activated foil stack has finite area ( $1 \times 1 \text{ cm}^2$ ), the efficiency for the point source geometry  $\epsilon_p$  was transferred by EFFTRAN to the efficiency for the foil stack geometry  $\epsilon$ , which is given in Table 7.

**TABLE 7:** Detection efficiencies for the point source geometry  $\epsilon_p$  and for the foil stack geometry  $\epsilon$  at the characteristic  $\gamma$  energies of  $^{152}\text{Eu}$  with their  $\gamma$  intensities  $I_\gamma$  (Martin,2013) adopted for efficiency determination, counts C and coincidence summing effect correction factors  $K_c$ . The 444.0 keV  $\gamma$ -line consists of 443.96 keV ( $I_\gamma = 2.827 \pm 0.014\%$ ) and 444.01 keV ( $I_\gamma = 0.298 \pm 0.011\%$ ) unresolved by our detector. The uncertainty in  $\epsilon$  is propagated from the uncertainties in C and  $I_\gamma$ .

$E_\gamma(\text{keV})$	$I_\gamma$	C	$K_c$	$\epsilon_p$	$\epsilon$
121.8	$28.53 \pm 0.16$	328049.3	1.113	3.0514	$3.0270 \pm 0.0178$
244.7	$7.55 \pm 0.04$	53997.8	1.158	2.0083	$1.9940 \pm 0.0136$
344.3	$26.59 \pm 0.20$	157183.5	1.078	1.555	$1.5450 \pm 0.0123$
411.1	$2.237 \pm 0.013$	9647.2	1.193	1.2803	$1.2720 \pm 0.0149$
444	$3.125 \pm 0.018$	13292.1	1.142	1.2087	$1.2013 \pm 0.0125$
778.9	$12.93 \pm 0.08$	32542.8	1.112	0.6964	$0.6922 \pm 0.0058$
1112.1	$13.67 \pm 0.08$	28712.2	1.033	0.5399	$0.5368 \pm 0.0045$
1408	$20.87 \pm 0.09$	34940.8	1.05	0.4374	$0.4349 \pm 0.0030$

**CHAPTER – 4**  
**DATA ANALYSIS PROCEDURE**

#### 4.1. Estimation of measured Cross Section

The spectrum averaged cross section for  $^{70}\text{Zn}(n,\gamma)^{71}\text{Zn}^m$  was calculated using the standard activation equation

$$\langle \sigma_{\text{Zn}}^m \rangle = \langle \sigma_{\text{Au}} \rangle (A_{\text{Zn}}/A_{\text{Au}}) [(a_{\text{Au}} N_{\text{Au}} I_{\text{Au}} \epsilon_{\text{Au}} f_{\text{Au}}) / (a_{\text{Zn}} N_{\text{Zn}} I_{\text{Zn}} \epsilon_{\text{Zn}} f_{\text{Zn}})] (C_{\text{Zn}}/C_{\text{Au}}) \quad (47)$$

where,  $A_x = \sum_i A_{x,i}$  ( $x$ : Zn or Au) is the number of counts ( $A_{x,i}$  is the number of counts from  $i$ -th counting),  $a_x$  is the isotopic abundance of the sample,  $N_x$  is the number of atoms,  $I_x$  is the gamma intensity,  $\epsilon_x$  is the detection efficiency,

$$f_x = [1 - \exp(-\lambda_x t_1)] \sum_i \exp(-\lambda_x t_{2,i}) [1 - \exp(-\lambda_x t_{3,i})] / \lambda_x \quad (48)$$

is the timing factor for the irradiation time  $t_1$ , cooling time for the  $i$ th counting  $t_{2,i}$ , measuring time for the  $i$ th counting  $t_{3,i}$ ,  $\lambda_x$  is the decay constant, and  $C_x$  is the correction factor ( $x$  = Zn or Au). The timing parameters and decay data are given in Table 3 and Table 4 respectively. The symbol  $\langle \dots \rangle$  in Eqn. (47) signifies that the cross section is averaged for the  $(p, n_0)$  neutron flux energy spectrum  $\phi_0(E)$  obtained from EPEN.

#### 4.2. Reference Cross Section

The  $^{197}\text{Au}(n,\gamma)^{198}\text{Au}$  reaction was used as the neutron flux monitor. Since the incident neutron beam of  $^7\text{Li}(p, n_0)^7\text{Be}$  is not monoenergetic with an energy spread of 0.15 MeV and 0.10 MeV at neutron energies 2.25 MeV and 2.60 MeV respectively, the point wise monitor cross section in the IAEA Neutron Cross-Section Standards was folded by neutron energy spectrum obtained from EPEN using the relation

$$\langle \sigma_{\text{Au}} \rangle = \int \Phi_0(E) \sigma_{\text{Au}}(E) dE \quad (49)$$

where  $\phi_0$  is the neutron flux energy spectrum obtained from EPEN and  $\sigma_{\text{Au}}(E)$  is the IAEA Standard Neutron Cross-Sections obtained from IAEA Neutron Cross-Section Standards (Carlson *et al.*, 2009).



The fractional uncertainty in the cross section was estimated using the quadrature sum of the fractional uncertainty in  $\langle\sigma_{Au}\rangle$ ,  $A_x$ ,  $a_x$ ,  $N_x$ ,  $I_x$ ,  $f_x$ ,  $C_x$  ( $x = \text{Zn}$  and  $\text{Au}$ ) as well as  $\varepsilon_{Au}/\varepsilon_{Zn}$  while the fractional uncertainty in  $\Delta f_x/f_x$  was obtained by assuming that the uncertainties were contributed by half-lives of  $^{71}\text{Zn}^m$  and  $^{198}\text{Au}$ . A detail explanation on the determination of  $\Delta f_x/f_x$  is given in Section 4.4.3.

### 4.3. Correction Factors

In the present work, we took into account different correction factors. The correction factor  $C_x$  ( $x = \text{Zn}$  or  $\text{Au}$ ) in Eqn. (47) is decomposed to

$$C_x = C_{x,fluc}C_{x,low}C_{x,scat}C_{x,attn.}$$

Each term is the correction factor for

- (1) neutron flux fluctuation (fluc)
- (2) low-energy neutron backgrounds due to  $^7\text{Li}(p,n_1)^7\text{Be}$  neutrons (low)
- (3) scattered neutron background originating from elastic, inelastic, and multiple scatterings in the foil stack and the surrounding materials (scat)
- (4)  $\gamma$ -ray self-attenuation (attn)

#### 4.3.1. Neutron flux fluctuation correction factor

During the irradiations, proton straggling in the target, the angle dependence of the neutron yield and energy, the close geometry, and multiple scattering of the neutron result in energy distributions of the primary component of the flux that differ for the monitor foils and the sample because of the flux attenuation between their different distances from the neutron source. This may be accounted for by simple means in very lightweight arrangements

(Reimer, 2005). On the other hand, the activity of the irradiated foil is proportional to the neutron flux, as a result of which the activation formula given in Eqn. (10) assumes a constant neutron flux during the irradiation. Therefore, the impact of fluctuations of the proton beam current during the long irradiation time was taken into consideration. Its correction factor for flux fluctuation was obtained by

$$C_{x,fluc} = \langle \Phi_m \rangle [1 - \exp(-\lambda_x t_1)] / \sum_{i=1,n} \Phi_{m,i} [1 - \exp(-\lambda_x \Delta t_1)] \exp[-\lambda_x (t_1 - i \Delta t_1)] \quad (50)$$

where  $\Phi_m$  is the neutron flux measured by the NE213 monitor detector during the  $i$ -th time interval ( $i=1,n$  i.e., time bin and  $n$  is number of total time bins),  $\Delta t_1 = t_1/n$  is the dwell time (i.e., 30 min) and  $\langle \phi_m \rangle = \sum_{i=1,n} \phi_{m,i}/n$  is the mean flux during irradiation (Sage *et al*, 2010; Fessler *et al.*, 2000). This method of taking the ratio of correction factors for measured Zinc to Gold samples for each irradiation is quite significant because the half-lives of the captured products  $^{71}\text{Zn}^m$  ( $3.96 \pm 0.05\text{h}$ ) and  $^{198}\text{Au}$  ( $2.6947 \pm 0.0003\text{d}$ ) which are formed simultaneously, are very different.

#### 4.3.2. Low-energy neutron backgrounds correction factor

One of the most important correction factors is contributed by the presence of low energy breakup neutrons ( $p,n_1$ ) coming from the target reactions. These low energy second groups of neutrons are produced due to the population of first excited state of  $^7\text{Be}$ . The neutron spectra are obtained from the neutron energy spectrum code EPEN. For proton energies above the cut-off energy,  $E_p^c = 2.37$  MeV, a second neutron production channel  $^7\text{Li}(p,n_1)^7\text{Be}$  opens in addition to  $^7\text{Li}(p,n_0)^7\text{Be}$  neutrons, leading to a second neutron group having lower energies. Above this cut-off energy, the neutrons are quasi-monoenergetic. The neutron spectrum obtained from EPEN clearly shows the separation between the two groups of neutrons with a deep valley between them. This separation between the ( $p,n_0$ ) and ( $p,n_1$ )

neutrons can be clearly seen for proton energy 2.60 MeV. On the other hand, the incident proton energy 2.25 MeV is lower than the cut-off energy, i.e. 2.37 MeV, therefore there is no contribution from the second group of neutrons and hence, the neutron spectrum obtained from EPEN show a broad spectrum. The third neutron group due to  ${}^7\text{Li}(p,n_2){}^7\text{Be}$  does not appear until  $E_p=7.07$  MeV, but at proton energies above  $E_p=3.70$  MeV, the  ${}^7\text{Li}(p,n+{}^3\text{He}+\alpha)$  three-body breakup channel opens up and shows a broad neutron spectrum. The position of the cut-off energy varies depending upon the incident proton energy. In general, the neutron capture cross sections decreases as the neutron energy increases and therefore, the contribution of the low-energy background neutrons has to be carefully determined and subtracted. The required correction factor for  $E_p=2.60$  MeV was then calculated by forming a ratio of the sample activities produced by neutrons below the cut-off energy to those produced by the entire neutron spectrum. Then, the  $(p,n_1)$  low energy neutron background was subtracted by the correction factor

$$C_{x,low} = 1 - \int \varphi_1(E)\sigma_x(E)dE / \int \varphi(E)\sigma_x(E)dE \quad (51)$$

where  $\varphi_1(E)$  is the  $(p,n_1)$  neutron flux energy spectrum calculated by EPEN and  $\varphi(E)$  is the sum of  $(p,n_0)$  and  $(p,n_1)$  neutron flux energy spectrum.  $\sigma_x(E)$  is the  ${}^{70}\text{Zn}(n,\gamma){}^{71}\text{Zn}^m$  cross section taken from TENDL-2015 library (Koning et al., 2015) or  ${}^{197}\text{Au}(n,\gamma){}^{198}\text{Au}$  cross section taken from the IAEA Neutron Cross-Sections Standards (Carlson *et al.*, 2009).

#### 4.3.3. Scattered neutron background correction factor

Several neutrons are scattered in the room background due to elastic, inelastic and multiples scattering in the foil stack and surrounding materials. The correction factors for these effects are considered and were evaluated by PHITS (Particle and Heavy Ion Transport code System) Ver 2.840 (Sato *et al.*, 2013). PHITS can deal with the transport of nearly all particles, including neutrons, protons, heavy ions, photons, and electrons, over wide energy

ranges using various nuclear reaction models and data libraries. PHITS also has several important features, such as an event-generator mode for low-energy neutron interaction (Niita, 2011), beam transport functions (Furusaka *et al.*, 2004; Nose *et al.*, 2005; Sakaki *et al.*, 2010), a function for calculating the displacement per atom (DPA) (Iwamoto *et al.*, 2012), and a microdosimetric tally function (Sato *et al.*, 2009). Due to these reasons, it has been widely used for several applications. The geometrical configurations of the simulation are all set up in accordance with the experimental set up. All the materials in and around the foil stack placed downstream of the tantalum proton beam stopper was modeled in the simulation. Neutrons were generated according to the (p,n<sub>0</sub>) neutron flux energy spectra  $\phi_0(E)$  calculated by EPEN and in the forward direction. Productions of  $^{71}\text{Zn}^m$  and  $^{198}\text{Au}$  were calculated with the (p,n<sub>0</sub>) neutron spectra from EPEN and evaluated cross sections of all foil stack and surrounding materials from the AceLibJ40 library (a library in the ACE Format based on JENDL-4.0). Cross sections were calculated by counting  $^{71}\text{Zn}^m$  and  $^{198}\text{Au}$  produced by all neutrons including neutrons scattered by a foil stack or surrounding material before the production (All), and those produced by neutrons not scattered before the production (True). The uncertainties in  $C_{\text{scat}}$  are about 0.5% and 0.1% for Zn and Au foils, respectively. The weighted means of  $C_{\text{scat}}$  are adopted in determination of experimental cross sections because it was impossible to distinguish gamma-rays from front and back foils in our measurement.

#### 4.3.4. Gamma-ray self-attenuation correction factor

Gamma-ray spectrometry is one of the most widely used techniques to determine the concentration of natural and artificial radionuclides in environmental samples. The use of germanium detectors in high-resolution gamma-ray spectrometry allows a precise quantitative determination of the radioactive concentration of any type of sample. When a gamma photon passes through any material, including the sample in which it is generated, it undergoes specific interactions with a given probability. In these interactions the photon is

either absorbed or scattered, losing energy; in any case it cannot contribute to the peak count-rate. This effect of gamma photon energy with a loss of energy within the sample itself before being measured with a detector apparatus is called Self-attenuation. The degree of self-attenuation depends on a number of factors such as sample geometry and linear attenuation coefficient  $\mu$ ; the linear attenuation coefficient depends in turn on material density, sample composition, and photon energy  $E$  (Robu *et al.*, 2008). If a stack of foils is used, the gamma photon attenuation in the sample can also induce serious systematic errors because the gamma photon, while passing through the second foil, is reduced by absorption in the first foil and so on. For the purposes of accuracy and precision that are needed in the analysis involving the NAA technique, gamma spectrometric analysis requires correction for the self-attenuation effect due to the interactions of the gamma-rays with the foil stack. If a stack of foils is used, the gamma photon attenuation in the sample also induces serious systematic errors since the gamma photon while passing through the second foil is reduced by absorption in the first foil and so on. It is usually a function of the total linear coefficient  $\mu_l$  multiplied by the thickness of the sample as measured in the direction of the gamma photon. For the purpose of accuracy and precision which are required in the analysis involving the NAA technique, gamma spectrometric analysis requires correction for the self-attenuation effect due to the interactions of the gamma-rays with the foil stack. According to Beer Lambert's law, the attenuation of a gamma-ray flux passing through a path of length  $x$  in a sample with linear attenuation coefficient  $\mu$  can be expressed as:

$$I_1/I_0 = \exp(-\mu_{l,1}x_1) = \exp(-\mu_{m,1}\rho_1x_1) \quad (52)$$

where  $\mu_m$  is the mass attenuation coefficient of the gamma energy and material-1,  $I_l$  is the gamma-ray flux at interface-1. If the 1<sup>st</sup> foil of thickness  $x_l$  is a homogenous source of the

gamma-line, and it penetrates other  $n-1$  foils of thickness  $x_i$  before reaching the detector, the probability is expressed by (Millsap *et al.*, 2015; Robu *et al.*, 2009; Jackman, 2007)

$$C_{S,attn} = \left[ \left(1/x_1\right) \int_0^{x_1} \exp(-\mu_{m,1}\rho_1x_1) dx \right] \cdot \prod_{i=2,n} \exp(-\mu_{m,i}\rho_ix_i)$$

$$= \left[ \left[1 - \exp(-\mu_{m,1}\rho_1x_1)\right] / (\mu_{m,1}\rho_1x_1) \right] \cdot \prod_{i=2,n} \exp(-\mu_{m,i}\rho_ix_i) \quad (53)$$

If the measured sample is subjected to attenuation and the calibration source is not, the correction factor  $C_{attn}$  must be applied to the peak area, i.e.,  $1/C_{S,attn}$ , then,

$$C_{attn} = C_{S,attn}^{-1} = \left[ (\mu_{m,1}\rho_1x_1) / \left[1 - \exp(-\mu_{m,1}\rho_1x_1)\right] \right] \cdot \prod_{i=2,n} \exp(-\mu_{m,i}\rho_ix_i) \quad (54)$$

The values of the correction factors are summarized in **Table 8**.

**Table 8:** Correction factors applied to the measured cross sections.

$E_n$ (MeV)	0.40	0.70
$C_{Zn,fluc} / C_{Au,fluc}$	0.888	0.939
$C_{Au,low}$		0.967
$C_{Zn,low}$		0.988
$C_{Zn,scat}$	0.980	0.984
	0.981 (front)	0.983 (front)
$C_{Au,scat}$	0.978 (back)	0.980 (back)
	0.980 (mean)	0.982 (mean)
$C_{Zn,attn}$	1.019	1.021
	1.024 (front)	1.028 (front)
$C_{Au,attn}$	1.013 (back)	1.015 (back)
	1.019 (mean)	1.022 (mean)

#### 4.4. Uncertainty Propagation

##### 4.4.1. Uncertainty in Detector Efficiency

In the present experiment, we used a hyperpure HPGe detector separated by 1 cm from the irradiated foil stack was used to determine  $C_{Zn}$  and  $C_{Au}$  in Eqn. (47). The detection efficiencies of the detector were measured by using eight gamma-lines of a  $^{152}Eu$  calibration source. The detection efficiency for the  $i$ -th gamma-line (emission probability  $I_i$ , Martin, 2013) was determined by

$$\varepsilon_{p,i} = \frac{C \varepsilon_{G,i} K_{c,i}}{A_0 e^{-\lambda t} \Delta t_{c,i} I_{\gamma,i}} \quad (55)$$

where  $C$  is the number of counts during the measuring time,  $K_{c,i}$  is the correction factor for the coincidence summing effect,  $A_0$  is the activity of the calibration source at the time of its manufacturer to the start of counting,  $\lambda$  is the decay constant of  $^{152}Eu$ .

In order to obtain the detector efficiencies at the characteristic gamma energies of the  $^{71}Zn^m$  ( $E_{Zn} = 386.28$  keV) and  $^{198}Au$  ( $E_{Au} = 411.802$  keV), the point-wise efficiencies in Table 7 were interpolated through the following fitting function (see Figure 26):

$$\varepsilon(E) = \varepsilon_0 \exp(-E/E_0) + \varepsilon_c \quad (56)$$

The fitting parameter values are given in Table 9. This equation gives the detection efficiencies of 386.28 keV gamma-ray of  $^{71}Zn^m$  and 411.802 keV gamma-ray of  $^{198}Au$  as  $\varepsilon_{Zn} = 1.404644 \pm 0.034969\%$  and  $\varepsilon_{Au} = 1.319418 \pm 0.034688\%$ , respectively.

**TABLE 9:** The efficiency curve fitting parameter values.

	Value	Uncertainty	Correlation Coefficient		
$\epsilon_0$	3.8896	0.2083	1		
$E_0$	279.5410	16.8800	-0.843	1	
$\epsilon_c$	0.4279	0.0194	0.408	-0.687	1

The uncertainties of  $\epsilon_0$ ,  $E_0$  and  $\epsilon_c$  are propagated from  $\Delta C_i = \sqrt{C_i}$  and  $\Delta I_i$  are determined by the ENSDF evaluator (Martin, 2013). It is not necessary to propagate the uncertainties in the parameters which are commonly applied to all the gamma-lines (e.g.,  $\Delta A_0$  and  $\Delta \gamma$ ) because only the ratio of the detection efficiency ( $\eta_{r,x} = \epsilon_r/\epsilon_x$ ) is required in our cross section measurement. The parameters reproducing the efficiency  $\epsilon_i$  in Table 7 gives the detection efficiency curve  $\epsilon(E_\gamma)$  in Figure 25.

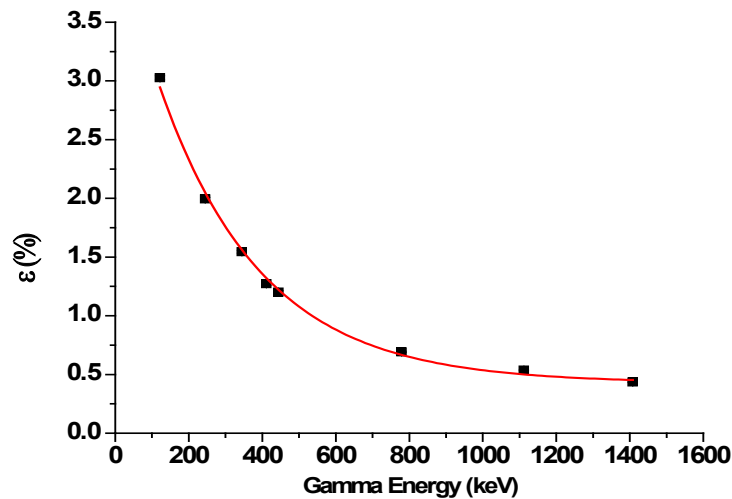


Figure 25: Detection efficiency calibration curve of the HPGe detector for the  $(1 \times 1)\text{-cm}^2$  source placed at a distance of 1 cm from the detector. The error bar for the uncertainty due to counting statistics is within the symbol.



The counts  $C$ , gamma intensities  $I_\gamma$ , coincidence summing effect correction factors  $K_c$ , the detection efficiencies for the point source geometry  $\varepsilon_p$  and for the foil stack geometry  $E$  at the characteristic gamma energies of  $^{152}\text{Eu}$  and the uncertainties  $\Delta\varepsilon$  propagated from the  $C$ ,  $\Delta C$ ,  $I_\gamma$ ,  $\Delta I_\gamma$ ,  $\varepsilon_p$ , and  $\varepsilon$  are given in Table 10.

**TABLE 10:** The uncertainties  $\Delta\varepsilon$  propagated from the  $C$ ,  $\Delta C$ ,  $I_\gamma$ ,  $\Delta I_\gamma$ ,  $\varepsilon_p$ , and  $\varepsilon$ .

$E_\gamma$ (keV)	$C$	$\Delta C$	$I_\gamma$	$\Delta I_\gamma$	$\varepsilon_{p(\text{uncor})}$ (%)	$K_c$	$\varepsilon_{p(\text{cor})}$ (%)	$\varepsilon$ (%)	$\Delta\varepsilon$ (%)
121.8	328049.3	572.7559	0.2853	0.00160	2.7416	1.113	3.0514	3.0270	0.0178
244.7	53997.8	232.3743	0.0755	0.00040	1.7343	1.158	2.0083	1.9940	0.0136
344.3	157183.5	396.4637	0.2659	0.00200	1.4425	1.078	1.5550	1.5450	0.0123
411.1	9647.2	98.22016	0.02237	0.00013	1.0731	1.193	1.2803	1.2720	0.0149
444.0	13292.1	115.2914	0.03125	0.00018	1.0584	1.142	1.2087	1.2013	0.0125
778.9	32542.8	180.3962	0.1293	0.00080	0.6263	1.112	0.6964	0.6922	0.0058
1112.1	28712.2	169.4467	0.1367	0.00080	0.5227	1.033	0.5399	0.5368	0.0045
1408.0	34940.8	186.9246	0.2087	0.00090	0.4166	1.050	0.4374	0.4349	0.0030

The covariance between the two interpolated efficiencies  $\varepsilon_{\text{Zn}}$  and  $\varepsilon_{\text{Au}}$  are obtained following the prescription by Mannhart (Mannhart, 2013):

$$\begin{aligned}
\text{cov}(\varepsilon_{\text{Zn}}, \varepsilon_{\text{Au}}) &= \exp\left[-(E_{\text{Zn}} + E_{\text{Au}})/E_0\right](\Delta\varepsilon_0)^2 \\
&+ \left(\varepsilon_0^2 E_{\text{Zn}} E_{\text{Au}}/E_0^4\right) \exp\left[-(E_{\text{Zn}} + E_{\text{Au}})/E_0\right](\Delta E_0)^2 + (\Delta\varepsilon_c)^2 + \varepsilon_0 \left[(E_{\text{Zn}} + E_{\text{Au}})/E_0^2\right] \\
&\exp\left[-(E_{\text{Zn}} + E_{\text{Au}})/E_0\right] \text{cov}(E_0, \varepsilon_0) + \left[\exp(-E_{\text{Zn}}/E_0) + \exp(-E_{\text{Au}}/E_0)\right] \text{cov}(\varepsilon_0, \varepsilon_c) \\
&+ \left[\left(\varepsilon_0 E_{\text{Zn}}/E_0^2\right) \exp(-E_{\text{Zn}}/E_0) + \left(\varepsilon_0 E_{\text{Au}}/E_0^2\right) \exp(-E_{\text{Au}}/E_0)\right] \text{cov}(\varepsilon_c, E_0)
\end{aligned} \tag{57}$$

which can also be used to obtain the uncertainty in the detection efficiency  $(\Delta\varepsilon_i)^2 = \text{Cov}(\varepsilon(\text{Ei}), \varepsilon(\text{Ei}))$ . Since only the ratio of the efficiencies  $\eta_{\text{Zn,Au}} = \varepsilon_{\text{Zn}}/\varepsilon_{\text{Au}}$  are required. It is not necessary to propagate the uncertainties in the parameters commonly applied to all gamma-lines (e.g.,  $\Delta A_0$ ,  $\Delta\lambda$ ) because only the ratio of the detection efficiency ( $\eta_{\text{m,x}} = \varepsilon_{\text{m}} = \varepsilon_{\text{x}}$ ) is

required in our cross section determination. Therefore, the fractional uncertainty  $\Delta\eta_{Zn}/\eta_{Au}$  is propagated from  $\text{var}(\varepsilon_{Zn})$ ,  $\text{var}(\varepsilon_{Au})$  and  $\text{cov}(\varepsilon_{Zn}, \varepsilon_{Au})$ .

$$(\Delta\eta/\eta)^2 = (\Delta\varepsilon_{Zn}/\varepsilon_{Zn})^2 + (\Delta\varepsilon_{Au}/\varepsilon_{Au})^2 - 2\text{cov}(\varepsilon_{Zn}, \varepsilon_{Au})/(\varepsilon_{Zn}, \varepsilon_{Au}) \quad (58)$$

where  $(\Delta\varepsilon_{Zn})^2 = \text{var}(\varepsilon_{Zn})$  and  $(\Delta\varepsilon_{Au})^2 = \text{var}(\varepsilon_{Au})$

Finally the detection efficiency ratio was obtained with very low uncertainty,  $\eta = 1.06459 \pm 0.00274$ .

#### 4.4.2. Uncertainty in Standard Gold Monitor Cross Section

The  $^{197}\text{Au}(n,\gamma)^{198}\text{Au}$  cross section in the IAEA Neutron Cross Section Standards (Carlson *et al.*, 2009, Figure 2(a)) was adopted as the monitor cross section in the present experiment. The uncertainties are estimated for the reference and measured cross section for the neutron energies 0.40, 0.70, 0.96, 1.69 MeV. The cross sections for the latter two energies were obtained in our previous work (Punte *et al.*, 2017; Lalremruata *et al.*, 2017). However, the uncertainty propagation is repeated in the present work. In order to estimate the uncertainty for the reference cross section, the covariance information provided by the IAEA Cross-Section Standard was adopted (Carlson *et al.*, 2009). Since the  $^7\text{Li}(p,n_0)^7\text{Be}$  incident neutron beam is not monoenergetic but has energy spread ( $E_n = 0.40 \pm 0.15$  and  $0.70 \pm 0.15$  MeV, see Figure (18) and (19)), the point-wise monitor cross section in the IAEA Neutron Cross-Section Standards  $\sigma_r(E)$  was folded by the neutron flux energy spectrum

$\phi_i(E)(\int_0^\infty dE\phi_i(E) = 1; i=1 \text{ and } 2 \text{ are for } E_n = 0.40 \text{ and } 0.70 \text{ MeV})$  calculated by the neutron energy spectrum code EPEN.

$$\bar{\sigma}_{r,i} = \int dE\phi_i(E)\sigma_r(E) \quad (59)$$

The IAEA Neutron Cross-Section Standards provide the covariance information of  $\sigma_r(E)$  for its group-wise cross section expression:

$$\langle \sigma_r \rangle_k = \left( \int_{E_{k,\min}}^{E_{k,\max}} dE \sigma_r(E) \right) / (E_{k,\max} - E_{k,\min}) \quad (60)$$

where  $E_{k,\min}$  and  $E_{k,\max}$  are the lower and upper boundaries of the k-th energy group. Similarly, we also introduce the group-wise neutron flux energy spectrum  $\Phi_{i,k}$  by

$$\Phi_{i,k} = \int_{E_{k,\min}}^{E_{k,\max}} dE \phi_i(E) \quad (61)$$

which satisfies  $\sum_k \phi_{i,k} = 1$  and the value of k ranges from 1-30, 31-44, 45-55, 56-59 for neutron energies  $0.40 \pm 0.15$ ,  $0.70 \pm 0.10$ ,  $0.96 \pm 0.15$ ,  $1.69 \pm 0.15$  MeV respectively. By using  $\langle \sigma_r \rangle_k$  and  $\Phi_{i,k}$ , Eqn. 59 is discretized to

$$\bar{\sigma}_{r,i} = \sum_k \Phi_{i,k} \langle \sigma_r \rangle_k \quad (62)$$

The uncertainty in our monitor cross section,  $\Delta \langle \sigma_{Au} \rangle$  due to the uncertainty in the IAEA Neutron Cross-Section Standards was obtained using the relation

$$(\Delta \langle \sigma_{Au} \rangle)^2 = \sum_i [\Phi_i^2 \text{var}(\langle \sigma_i \rangle)] / (\sum_i \Phi_i)^2 + 2 \sum_{i>j} [\Phi_i \Phi_j \text{cov}(\langle \sigma_i \rangle, \langle \sigma_j \rangle)] / (\sum_i \Phi_i)^2 \quad (63)$$

where  $\text{cov}(\langle \sigma_i \rangle, \langle \sigma_j \rangle)$  and  $\text{var}(\langle \sigma_i \rangle)$  are the covariance between the ith and the jth group-wise cross sections compiled in the IAEA Neutron Cross-Section Standards and its diagonal component ( $i = j$ ) and  $\Phi_i = \int \phi_o(E) dE$  is the neutron flux energy spectrum integrated over the ith group of the IAEA Neutron Cross-Section Standards. The summations for i and j are taken for all energy groups between 0.090 and 0.585 MeV for  $\langle E_n \rangle = 0.40$  MeV neutrons, between 0.4625 and 0.970 MeV for  $\langle E_n \rangle = 0.70$  MeV neutrons, between 0.675 and 1.325

MeV for  $\langle E_n \rangle = 0.96$  MeV neutrons, between 1.325 and 2.100 MeV for  $\langle E_n \rangle = 1.69$  MeV neutrons. The spectrum average cross sections are  $\langle \sigma_{Au} \rangle = 167.16 \pm 1.11$  mb,  $99.00 \pm 0.77$  mb,  $82.77 \pm 0.86$  mb and  $64.09 \pm 0.92$  mb for  $\langle E_n \rangle = 0.40, 0.70, 0.96$  and  $1.69$  MeV respectively. The fractional group-wise flux  $\Phi_i / \sum \Phi_i$  is obtained using EPEN neutron spectra, and we adopted unweighted group-wise cross sections of the IAEA neutron cross-section standard. The group-wise quantities for all energies are given in **Appendix 1** and the correlation coefficients obtained from the IAEA Neutron Cross Section Standards (Carlson et al., 2009) are given in **Appendix 2-7**. The covariance in the IAEA Neutron Cross Section Standards are then propagated to  $\langle \sigma_{Au} \rangle$  as

$$\text{cov}(\langle \sigma \rangle_i, \langle \sigma \rangle_j) = \sum_i \sum_j w_{ik} w_{jl} \Delta \sigma_k \Delta \sigma_l \text{cor}(\sigma_k, \sigma_l) \quad (64)$$

where

$w_{ik} = \Phi_k / \sum \Phi_k$  and  $w_{jl} = \Phi_l / \sum \Phi_l$  for fields  $i$  and  $j$  respectively. Finally, the correlation coefficients between the spectrum averaged cross sections are obtained using the equation

$$\text{cor}(\langle \sigma_i \rangle, \langle \sigma_j \rangle) = \text{cov}(\langle \sigma_i \rangle, \langle \sigma_j \rangle) / (\Delta \langle \sigma \rangle_i / \langle \sigma \rangle_i) \cdot (\Delta \langle \sigma \rangle_j / \langle \sigma \rangle_j) \quad (65)$$

Table 11 shows the spectrum averaged monitor cross section along with its uncertainty and correlation coefficients between them obtained by Eqn.(65).

**TABLE 11:** Spectrum averaged monitor cross section, its uncertainty and correlation coefficients.

En (MeV)	$\langle \sigma_{Au} \rangle$ (mb)	Correlation coefficient			
0.40	$167.16 \pm 1.11$	1.000			
0.70	$99.00 \pm 0.77$	0.472	1.00		
0.96	$82.77 \pm 0.86$	0.341	0.402	1.00	
1.69	$64.09 \pm 0.92$	0.248	0.217	0.222	1.00

#### 4.4.3. Uncertainty in the timing factor, $\Delta f_x/f_x$

The equation for the timing factor given in Eqn. (55) contains five sources of uncertainties viz.,  $t_1$ ,  $t_2$ ,  $t_3$ ,  $\lambda_x$  and  $\lambda_x$  ( $x = \text{Zn}$  and  $m = \text{Au}$ ). The gamma-lines of the reaction product  $^{71}\text{Zn}^m$  and monitor product  $^{198}\text{Au}$  were measured simultaneously. Therefore, it is possible to set  $t_{2,x} = t_{2,m} = t_2$  and  $t_{3,x} = t_{3,m} = t_3$ . In the present experimental work, the uncertainties in  $t_1$ ,  $t_2$  and  $t_3$  were considered as negligible as a result of which only the uncertainties in  $\lambda_x$  and  $\lambda_x$  had to be propagated. Since the decay constant is related with the cross section through the exponential function, the uncertainty in the decay constant should not be included in the quadrature sum formula. The uncertainties in the timing factors should be propagated from the uncertainties in the decay constants. Then, the uncertainties in the timing factor should again be propagated to find the uncertainties in measured cross section using the quadrature sum formula i.e.,  $(\Delta\sigma + \sigma)^2 = \dots + (\Delta f_x + f_x)^2 + (\Delta f_m + f_m)^2 + \dots$

For the timing factor in Eqn. (48),

$$f_x = [1 - \exp(-\lambda_x t_1)] \sum_i \exp(-\lambda_x t_{2,i}) [1 - \exp(-\lambda_x t_{3,i})] / \lambda_x = \sum_i f_{x,i} \quad (66)$$

The uncertainty in the timing factor is given by,

$$\begin{aligned}\Delta f_{x,i} &= \left(\partial f_{x,i} / \partial \lambda_x\right) \Delta \lambda_x = \left(\partial f_{x,i} / \partial \lambda_x\right) \left(d\lambda_x / dT_{1/2,x}\right) \Delta T_{1/2,x} \\ &= \left(\lambda_x / T_{1/2,x}\right) \left(\partial f_{x,i} / \partial \lambda_x\right) \Delta T_{1/2,x}\end{aligned}\quad (67)$$

Assuming that only the uncertainty in the half-life is responsible to the uncertainty in the timing factor, the uncertainty in the decay constant  $\Delta \lambda = (\ln 2 \Delta T_{1/2}) = T_{1/2}^2$  can be obtained from  $\Delta T_{1/2}$  in the ENSDF library. The partial derivative  $\partial f_{x,i} / \partial \lambda_x$  can be calculated by

$$\begin{aligned}\partial f_{x,i} / \partial \lambda_x &= f_{x,i} t_{1,i} \exp(-\lambda_x t_{1,i}) / [1 - \exp(-\lambda_x t_{1,i})] - f_{x,i} t_{2,i} \\ &+ f_{x,i} t_{3,i} \exp(-\lambda_x t_{3,i}) / [1 - \exp(-\lambda_x t_{3,i})] - f_{x,i} / \lambda_x\end{aligned}\quad (68)$$

This equation shows that the sensitivity depends not only on  $\lambda$  but also on  $t_1$ ,  $t_2$  and  $t_3$ , even though the uncertainties in the latter three parameters are treated as negligible. Finally, the fractional uncertainty in  $f_x$  is obtained by

$$\Delta f_x / f_x = \left[ \sum_i (\Delta f_{x,i})^2 \right]^{1/2} f_x \quad (69)$$

Taking the first, second, third and fourth parts of the right hand side of Eqn. (48) as Eqn.(i), (ii), (iii) and (iv), and the parameters given in Table 12, the timing factors for  $^{71}\text{Zn}^m$  and  $^{198}\text{Au}$  at proton energies of 2.6 MeV and 2.25 MeV are calculated as shown in the Tables 13(a) & (b) and 14(a) & (b).

**TABLE 12:** Decay data adopted for calculation of timing factor taken from the ENSDF library.

Nuclide	$T_{1/2}$ (sec)	$\Delta T_{1/2}$ (sec)	$\lambda$ (1/sec)	$\Delta\lambda$ (1/sec)
$^{71}\text{Zn}^m$	14256	180	4.86214E-05	6.13907E-07
$^{198}\text{Au}$	232822.08	25.92	2.97715E-06	3.31446E-10

**TABLE 13(a):** Calculation of timing factor for  $^{71}\text{Zn}^m$  at  $E_p = 2.6$  MeV.

$E_p = 2.6$ MeV										
$^{71}\text{Zn}^m$										
$t_1$ Sec	$t_{2i}$ sec	$t_{3i}$ sec	$f_i$ sec	Eqn.(i) sec <sup>2</sup>	Eqn.(ii) sec <sup>2</sup>	Eqn.(iii) sec <sup>2</sup>	Eqn.(iv) sec <sup>2</sup>	$\partial f_i / \partial \lambda$ sec <sup>2</sup>	$\Delta f$ sec	$\Delta f / f$ (%)
18924	1127	1983.7	1077	13499447	-1213614	21096807	-22147718	11234923	14.097918	0.1626515
18924	3115.7	1804.9	893	11198465	-2783267	17578265	-18372637	7620825		
18924	6623	1804.4	753	9440243	-4987451	14818560	-15488029	3783322		
18924	8434.4	1760.6	674	8443398	-5680835	13268114	-13852566	2178111		
18924	10381	3599.9	1199	15032972	-12448723	22568142	-24663677	488714		
18924	13987.9	3600	1006	12615152	-14076211	18938361	-20696909	-3219608		
18924	17594.9	3600	844	10585881	-14857802	15891939	-17367608	-5747590		
18924	21201.9	3600	709	8883038	-15023706	13335565	-14573857	-7378960		
18924	24808.9	3600	595	7454114	-14751776	11190408	-12229509	-8336763		
18924	28415.9	3600	499	6255047	-14178580	9390321	-10262272	-8795485		
18924	32022.9	3600	419	5248861	-13408077	7879795	-8611485	-8890905		

**TABLE 13(b):** Calculation of timing factor for  $^{198}\text{Au}$  at  $E_p = 2.6$  MeV.

$E_p = 2.6$ MeV										
$^{198}\text{Au}$										
$t_1$	$t_{2i}$	$t_{3i}$	$f_i$	Eqn.(i)	Eqn.(ii)	Eqn.(iii)	Eqn.(iv)	$\partial f_i / \partial \lambda$	$\Delta f$	$\Delta f / f$
sec	sec	sec	sec	$\text{sec}^2$	$\text{sec}^2$	$\text{sec}^2$	$\text{sec}^2$	$\text{sec}^2$	sec	(%)
18924	1127	1983.7	107.988	351612269	-1213614.3	360638763	-36170578	349331629	0.2832743	0.0168057
18924	3115.7	1804.9	97.7003	291679925	-2783267.2	299247563	-30005300	288091218		
18924	6623	1804.4	96.6588	245884524	-4987451.5	252264188	-25294298	240218279		
18924	8434.4	1760.6	93.8113	219920278	-5680835.4	225641004	-22623339	213647050		
18924	10381	3599.9	190.187	391555083	-12448723	400640603	-40279521	376951746		
18924	13987.9	3600	188.161	328579549	-14076211	336203754	-33801188	312695209		
18924	17594.9	3600	186.151	275724299	-14857802	282122076	-28363934	259349223		
18924	21201.9	3600	184.163	231371335	-15023706	236739967	-23801317	215074425		
18924	24808.9	3600	182.196	194152982	-14751776	198658016	-19972641	178332809		
18924	28415.9	3600	180.25	162921567	-14178580	166701922	-16759845	147846452		
18924	32022.9	3600	178.324	136714031	-13408077	139886279	-14063859	122553636		

**TABLE 14(a):** Calculation of timing factor for  $^{71}\text{Zn}^m$  at  $E_p = 2.25$  MeV.

$E_p = 2.25$ MeV										
$^{71}\text{Zn}^m$										
$t_1$	$t_{2i}$	$t_{3i}$	$f_i$	Eqn.(i)	Eqn.(ii)	Eqn.(iii)	Eqn.(iv)	$\partial f_i / \partial \lambda$	$\Delta f$	$\Delta f / f$
Sec	sec	sec	sec	$\text{sec}^2$	$\text{sec}^2$	$\text{sec}^2$	$\text{sec}^2$	$\text{sec}^2$	sec	(%)
32160	2428	3776.7	2424.11	20644442	-5885750	45419352	-4985691	10321132	28.9162432	0.24404775
32160	6210.7	7232.1	3564.29	30354462	-2213671	61172045	-7330688	-3917087		
32160	13450.8	7216.7	2502.18	21309230	-3365626	42960597	-5146239	-2084882		
32160	20674.5	7306.3	1779.3	15153061	-3678623	30479045	-3659506	-2774920		
32160	27989.8	7235.1	1236.62	10531371	-3461263	21221781	-2543355	-2829304		
32160	35233.9	2551.8	342.104	2913454.6	-1205366	6608608.4	-7036075	-9567673.		



**TABLE 14(b):** Calculation of timing factor for  $^{198}\text{Au}$  at  $E_p = 2.25$  MeV.

$E_p = 2.25$ MeV										
$^{198}\text{Au}$										
$t_1$	$t_{2i}$	$t_{3i}$	$f_i$	Eqn.(i)	Eqn.(ii)	Eqn.(iii)	Eqn.(iv)	$\partial f_i / \partial \lambda$	$\Delta f$	$\Delta f / f$
Sec	sec	sec	sec	$\text{sec}^2$	$\text{sec}^2$	$\text{sec}^2$	$\text{sec}^2$	$\text{sec}^2$	sec	(%)
32160	2428	3776.7	340.429	775881075	-5885750	809669913	-81423891	765426326	0.55433948	0.01824202
32160	6210.7	7232.1	641.298	1.141E+09	-2213671	1.184E+09	-1.20E+09	1.106E+09		
32160	13450.8	7216.7	626.3	800865819	-3365626	831462452	-84045884	758213164		
32160	20674.5	7306.3	620.503	569498205	-3678623	591176428	-59765293	526235465		
32160	27989.8	7235.1	601.282	395801012	-3461263	410911074	-41536853	356730914		
32160	35233.9	2551.8	208.994	109496506	-1205366	114473832	-11490977	97006907		

#### 4.4.4. Correlation between measured Cross Sections

**Table 15** summarizes the overall and partial uncertainties in various parameters to obtain the  $^{70}\text{Zn}(n,\gamma)^{71}\text{Zn}^m$  cross section at neutron energies, 0.40, 0.70, 0.96 and 1.69 MeV. The cross sections at 0.96 and 1.69 MeV are obtained in our previous work (Punte *et al.*, 2017; Lalremruata *et al.*, 2017). The total uncertainty reported is the quadrature sum of partial uncertainties. The fractional variance and covariance and hence the correlation coefficients between each set of energy are constructed using the following equations 70 to 78.

$$\text{var}(\Delta x_i) = \sum_i (\Delta x_i)^2 \quad (70)$$

$$\text{cov}(\Delta x_i, \Delta x_j) = \sum_i \sum_j \Delta x_i \Delta x_j \text{cor}(\Delta x_i, \Delta x_j) \quad (71)$$

$$\text{Correlation} = \text{Cov}(\Delta x_i, \Delta x_j) / [\text{Var}(\Delta x_i) \cdot \text{Var}(\Delta x_j)]^{1/2} \quad (72)$$

**TABLE 15:** Fractional uncertainties (%) in various parameters to obtain the  $^{70}\text{Zn}(n,\gamma)^{71}\text{Zn}^m$  cross section.

En (MeV)	AZn	AAu	aZn	nZn	nAu	lZn	lAu	fZn	fAu	$\eta$	$\langle\sigma_{\text{Au}}\rangle$	Total
0.40	5.239	1.996	1.381	0.088	0.131	2.298	0.063	0.244	0.018	0.257	0.679	6.262
0.70	1.410	0.598	1.381	0.088	0.099	2.298	0.063	0.163	0.017	0.257	0.780	3.203
0.96	7.809	3.247	1.381	0.115	0.099	2.298	0.063	0.177	0.027	0.257	1.030	8.940
1.69	5.988	2.471	1.381	0.088	0.097	2.298	0.063	0.273	0.015	0.257	1.461	7.167
Cor(0.40,0.70)	0	0	1	1	0	1	1	1	1	1	0.472	0.373
Cor(0.40,0.96)	0	0	1	0	0	1	1	1	1	1	0.341	0.135
Cor(0.40,1.69)	0	0	1	1	0	1	1	1	1	1	0.248	0.169
Cor(0.70,0.96)	0	0	1	0	0	1	1	1	1	1	0.402	0.262
Cor(0.70,1.69)	0	0	1	1	0	1	1	1	1	1	0.217	0.316
Cor(0.96,1.69)	0	0	1	0	0	1	1	1	1	1	0.222	0.119

#### 4.5. Nuclear Models

The excitation function of  $^{70}\text{Zn}(n,\gamma)^{71}\text{Zn}^m$  reaction from 0.1 MeV to 2.5 MeV has been calculated using the nuclear reaction model code TALYS-1.8 (Koning *et al.*, 2015). The nuclear models implemented in this code can generally be categorized into optical, direct, pre-equilibrium, compound and fission models, which can be used with various buildup parameter options including those compiled in the RIPL-3 Reference Input Parameter Library (Capote *et al.*, 2009). They are all driven by a comprehensive database of nuclear structure and model parameters.

The default optical model potentials (OMP) used in TALYS are based on the local and global parametrizations by Koning and Delaroche (Koning and Delaroche, 2003). The compound nucleus contribution was calculated by the Hauser-Feshbach model (Hauser and Feshbach, 1952).

##### 4.5.1. Level Densities

Since many years back, nuclear level densities (NLDs) had been a field of research with Bethe's pioneering work (Bethe, 1936). In the evaluation of nuclear data, the knowledge

of NLDs plays an important role. In certain nuclear reactions, the number of levels to which decay occurs is too large to allow an individual description. In such cases, level densities are required for modeling the nuclear reactions. In statistical models for predicting cross sections, nuclear level densities are used at excitation energies where discrete level information is not available or incomplete. Several models for the level density are used in TALYS, which range from phenomenological analytical expressions to tabulated level densities derived from microscopic models.

The following six level density models available in TALYS-1.8 were used:

(1) Level Density Model 1(LDM-1): The Constant Temperature and Fermi Gas Model

In this model, the constant temperature model is used in the low excitation region and the Fermi-gas model is used in the high excitation energy region. The transition energy is around the neutron separation energy.

Arguably the best known analytical level density expression is that of the Fermi Gas model (FGM). It is based on the assumption that the single particle states which construct the excited levels of the nucleus are equally spaced, and that collective levels are absent. For a two-fermion system, i.e. distinguishing between excited neutrons and protons, the total Fermi gas state density reads

$$w_F^{tot}(E_x) = \frac{\sqrt{\pi}}{12} \frac{\exp[2\sqrt{aU}]}{a^{1/4}U^{5/4}} \quad (73)$$

with U is the effective excitation energy defined by

$$U = E_x - \Delta, \quad (74)$$

where the energy shift  $\Delta$  is an empirical parameter which is equal to, or for some models closely related to, the pairing energy which is included to simulate the known odd-even

effects in nuclei. In practice,  $\Delta$  plays an important role as adjustable parameter to reproduce observables, and its definition can be different for different level density models.

Under the assumption that the projections of the total angular momentum are randomly coupled, the Fermi gas level density can be derived (Ericson, 1960) as:

$$\rho F(E_x, J, \Pi) = \frac{1}{2} \frac{2J+1}{2\sqrt{2\pi}\sigma^3} \exp\left[-\frac{\left(J+\frac{1}{2}\right)^2}{2\sigma^2}\right] \frac{\sqrt{\pi} \exp[2\sqrt{aU}]}{12 a^{1/4} U^{5/4}} \quad (75)$$

where the first factor  $1/2$  represents the aforementioned equiparity distribution and  $\sigma^2$  is the spin cut-off parameter, which represents the width of the angular momentum distribution which depends on excitation energy.

In the Constant Temperature Model (CTM), as introduced by Gilbert and Cameron (Gilbert *et al.*, 1965), the excitation energy range is divided into a low energy part from 0 MeV up to a matching energy  $E_M$ , where the so-called constant temperature law applies and a high energy part above  $E_M$ , where the Fermi gas model applies. Hence, for the total level density we have

$$\rho^{tot}(E_x) = \rho_T^{tot}(E_x), \text{ if } E_x \leq E_M \quad (76)$$

$$= \rho_F^{tot}(E_x), \text{ if } E_x \geq E_M \quad (77)$$

and similarly for the level density

$$\begin{aligned} \rho(E_x, J, \Pi) &= \frac{1}{2} R_F(E_x, J) \rho_T^{tot}(E_x), \text{ if } E_x \leq E_M \\ &= \rho_F(E_x, J, \Pi), \text{ if } E_x \geq E_M \end{aligned} \quad (78)$$

(2) Level Density Model2(LDM-2): The Back-shifted Fermi gas Model:

In the Back-shifted Fermi gas Model (BFM) (Goriely *et al.*, 2011), the pairing energy is treated as an adjustable parameter and the Fermi gas expression is used all the way down to 0 MeV. Hence for the total level density, we have

$$\rho_F^{tot}(E_x) = \frac{1}{\sqrt{2\pi\sigma}} \frac{\sqrt{\pi}}{12} \frac{\exp\left[2\sqrt{aU}\right]}{a^{1/4}U^{5/4}} \quad (79)$$

And for the level density,

$$\rho_F(E_x, J, \Pi) = \frac{1}{2} \frac{2J+1}{2\sqrt{2\pi}\sigma^3} \exp\left[-\frac{\left(J+\frac{1}{2}\right)^2}{2\sigma^2}\right] \frac{\sqrt{\pi}}{12} \frac{\exp\left[2\sqrt{aU}\right]}{a^{1/4}U^{5/4}} \quad (80)$$

(3) Level Density Model 3(LDM-3): The Generalized Superfluid Model:

The Generalized Superfluid Model (GSM) takes superconductive pairing correlations into account according to the Bardeen-Cooper-Schrieffer theory. The phenomenological version of the model (Larsen *et al.*, 2010a; Larsen *et al.*, 2010b) is characterized by a phase transition from a superfluid behaviour at low energy, where pairing correlations strongly influence the level density, to a high energy region which is described by the FGM. The GSM thus resembles the CTM to the extent that it distinguishes between a low energy and a high energy region, although for the GSM this distinction follows naturally from the theory and does not depend on specific discrete levels that determine a matching energy. Instead, the model automatically provides a constant temperature-like behavior at low energies. For the level density expressions, it is useful to recall the general formula for the total level density,

$$\rho^{tot}(E_x) = \frac{1}{\sqrt{2\pi\sigma}} \frac{e^S}{\sqrt{D}} \quad (81)$$

where  $S$  is the entropy and  $D$  is the determinant related to the saddle-point approximation. For the GSM this expression has two forms: one below and one above the so called critical energy  $U_c$ .

For energies below  $U_c$ , the level density is described in terms of thermodynamical functions defined at  $U_c$ , which is given by

$$U_c = a_c T_c^2 + E_{cond}. \quad (82)$$

Here, the critical temperature  $T_c$  is

$$T_c = 0.567 \Delta_0 \quad (83)$$

where the pairing correlation function is given by

$$\Delta_0 = \frac{12}{\sqrt{A}} \quad (84)$$

(4) Level Density Model 4(LDM-4): The Microscopic Level Densities from Goriely's table (Capote *et al.*, 2009).

Besides the phenomenological models that were used in TALYS, there is also an option to employ more microscopic approaches. For the RIPL database, S. Goriely has calculated level densities from drip line to drip line on the basis of Hartree-Fock calculations (Goriely *et al.*, 2001) for excitation energies up to 150 MeV and for spin values up to  $I = 30$ . In LDM-4, these tables with microscopic level densities can be read. Moreover, new energy-, spin- and parity-dependent nuclear level densities based on the microscopic combinatorial model have been proposed by Hilaire and Goriely (Goriely *et al.*, 2008). The combinatorial model includes a detailed microscopic calculation of the intrinsic state density and collective enhancement. The only phenomenological aspect of the model is a simple damping function

for the rotational effects. The calculations make coherent use of nuclear structure properties determined within the deformed Skyrme-Hartree-Fock-Bogolyubov framework.

(5) Level Density Model 5(LDM-5): The Microscopic Level Densities from Hilaire's table (R. Capote *et al.*, 2009).

Level densities for more than 8500 nuclei are made available in tabular format, for excitation energies up to 200 MeV and for spin values up to  $J = 49$ . These level densities are used with LDM-5. For the ldmodel 5, the new energy-, spin- and parity-dependent nuclear level densities based on the microscopic combinatorial model have been proposed by Hilaire and Goriely (Goriely *et al.*, 2008). The combinatorial model includes a detailed microscopic calculation of the intrinsic state density and collective enhancement. The only phenomenological aspect of the model is a simple damping function for the rotational effects. The calculations make coherent use of nuclear structure properties determined within the deformed Skyrme-Hartree-Fock-Bogolyubov framework.

For both microscopic Level Density Models, tables for level densities on top of the fission barriers are automatically invoked for LDM-4 or LDM-5, when available in the structure database. For nuclides outside the tabulated microscopic database, the default Fermi gas model is used.

(6) Level Density Model 6(LDM-6): The microscopic level densities (temperature dependent Hartree-Fock-Bogolyubov, Gogny force) from Hilaire's combinatorial tables (Hilaire *et al.*, 2012)

The most recent option, invoked with LDM-6, is based on temperature-dependent Hartree-Fock-Bogolyubov calculations using the Gogny force (Hilaire *et al.*, 2012). Since these microscopical level densities, called  $\rho_{\text{HFM}}$ , have not been adjusted to experimental data, an adjustment flexibility was added through a scaling function, i.e.

$$\rho(E_x, J, \pi) = \exp\left(c\sqrt{E_x - \delta}\right) \rho_{HFM}(E_x - \delta, J, \pi) \quad (85)$$

where by default  $c = 0$  and  $\delta = 0$  (i.e. unaltered values from the tables). The “pairing shift”  $\delta$  simply implies obtaining the level density from the table at a different energy. The constant  $c$  plays a role similar to that of the level density parameter  $a$  of phenomenological models. Adjusting  $c$  and  $\delta$  together gives adjustment flexibility at both low and higher energies.

For both microscopic Level Density Models, tables for level densities on top of the fission barriers are automatically invoked for LDM-4, LDM-5 or LDM-6, when available in the structure database. For nuclides outside the tabulated microscopic database, the default Fermi gas model is used.

#### 4.5.2. Gamma-ray Transmission Coefficients

Gamma-ray transmission coefficients are important for the description of the gamma emission channel in nuclear reactions. This is an almost universal channel since gamma rays, in general, may accompany emission of any other emitted particle. Like the particle transmission coefficients that emerge from the optical model, gamma-ray transmission coefficients enter the Hauser-Feshbach model for the calculation of the competition of photons with other particles.

There are eight different options for the  $\gamma$ -ray strength function in TALYS-1.8 and their sensitivity has been studied. In general, most of these options are based on the work of Kopecky and Uhl (Kopecky and Uhl, 1990), or Brink (Brink, 1957) and Axel (Axel, 1962). The eight different Photon Strength Functions are listed below:

(1) Photon Strength Function 1 (PSF-1): Kopecky-Uhl generalized Lorentzian (Kopecky and Uhl, 1990).



- (2) Photon Strength Function 2(PSF-2): Brink (Brink, 1957) and Axel Lorentzian (Axel, 1962).
- (3) Photon Strength Function 3(PSF-3): Hartree-Fock BCS tables (Capote *et al.*, 2009).
- (4) Photon Strength Function 4(PSF-4): Hartree-Fock-Bogolyubov tables (Capote *et al.*, 2009).
- (5) Photon Strength Function 5(PSF-5): Goriely's hybrid model (Goriely, 1998).
- (6) Photon Strength Function 6(PSF-6): Goriely temperature-dependent Hartree-Fock-Bogolyubov.
- (7) Photon Strength Function 7(PSF-7): Temperature-dependent relativistic mean field.
- (8) Photon Strength Function 8(PSF-8): Gogny D1M Hartree-Fock-Bogolyubov+QRPA.

**CHAPTER – 5**  
**RESULTS AND DISCUSSIONS**

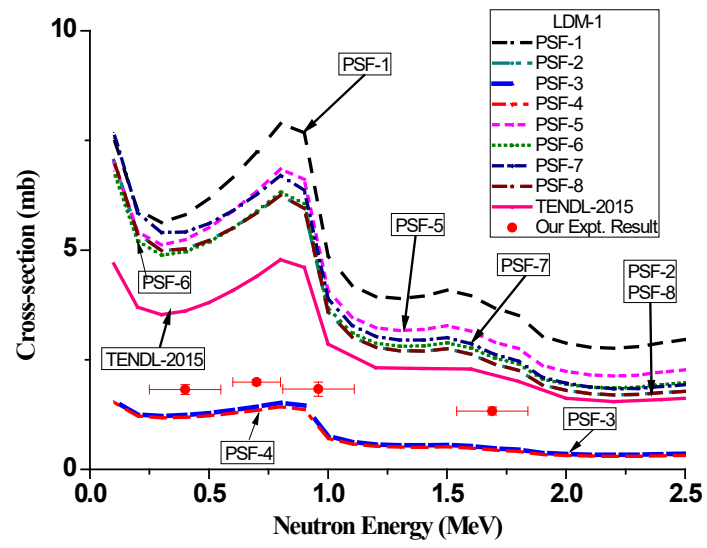
## RESULTS AND DISCUSSIONS

The  $^{70}\text{Zn}(n,\gamma)^{71}\text{Zn}^m$  reaction cross sections newly determined in the present work at neutron energies 0.40 MeV and 0.70 MeV including our earlier measured cross-sections at 0.96 MeV and 1.69 MeV are given in Table 16.

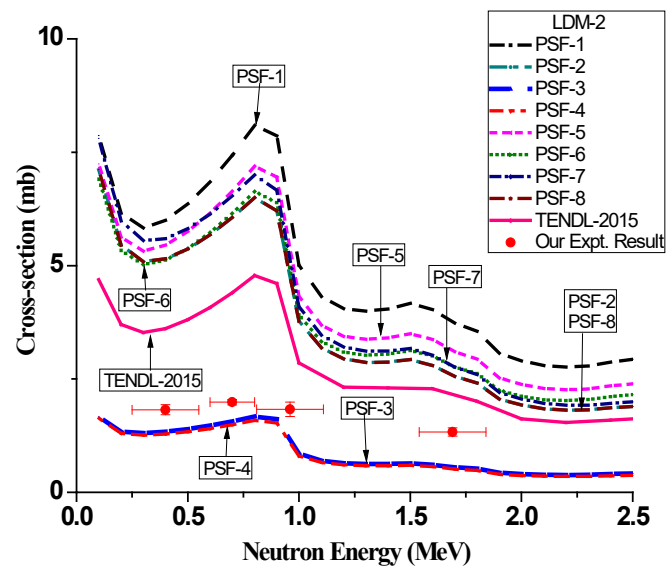
**TABLE 16:** The  $^{70}\text{Zn}(n,\gamma)^{71}\text{Zn}^m$  cross sections measured in the present experiment with their total uncertainties and their correlation coefficients.

En (MeV)	$\langle \sigma_{Zn}^m \rangle_{\text{exp}}$ (mb)	Correlation coefficients			
0.40	$1.82 \pm 0.11$	1.00			
0.70	$1.99 \pm 0.06$	0.38	1.00		
0.96	$1.83 \pm 0.16$	0.13	0.27	1.00	
1.69	$1.33 \pm 0.10$	0.17	0.33	0.12	1.00

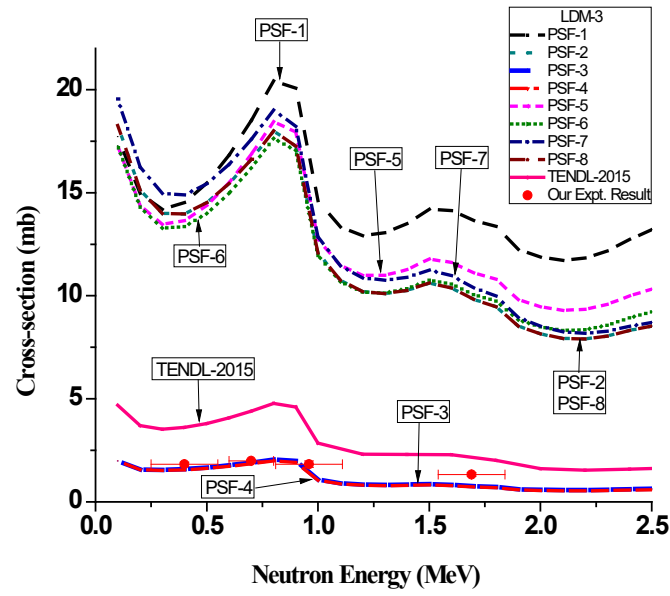
The comparison between the measured spectrum averaged  $^{70}\text{Zn}(n,\gamma)^{71}\text{Zn}^m$  reaction cross sections and the cross sections for monoenergetic neutrons calculated by nuclear reaction model code TALYS-1.8 at various Level Density Models and Photon Strength Functions are shown in Figure 27(a-f). This figure shows that the TALYS-1.8 results for all level density models (LDM-1 to LDM-6) with two Photon Strength Functions (PSF-3 and PSF-4) are close to all the experimental cross sections. TALYS-1.8 with the generalized superfluid level model (LDM-3) in Figure 26(c) best matches the measured cross sections at 0.40, 0.70 and 0.96 MeV. However, the cross section at neutron energy 1.69 MeV is slightly underestimated by these theoretical values calculated by TALYS-1.8 with Level Density Model 3 (LDM-3), Photon Strength Functions (PSF-3 and PSF-4). Figure 26 shows that the prediction of TALYS-1.8 is very sensitive to the choice of the Level Density Models and the Photon Strength Functions.



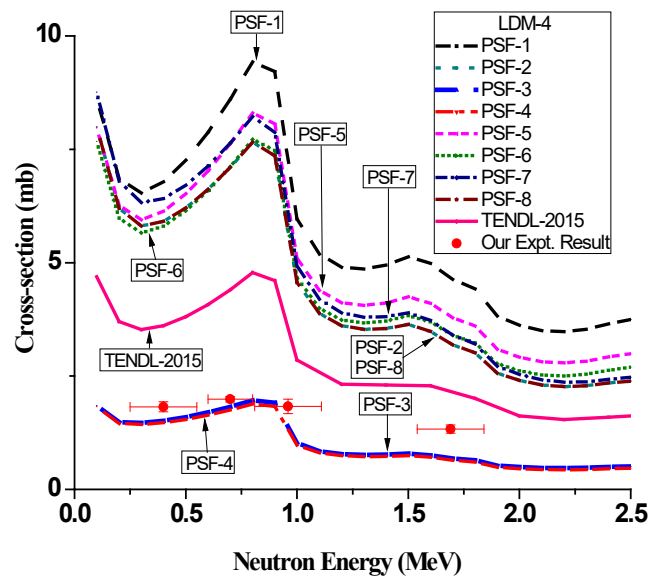
(a)



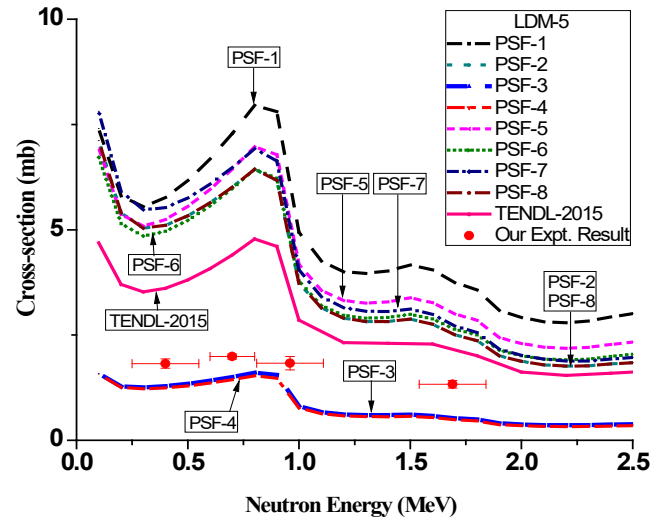
(b)



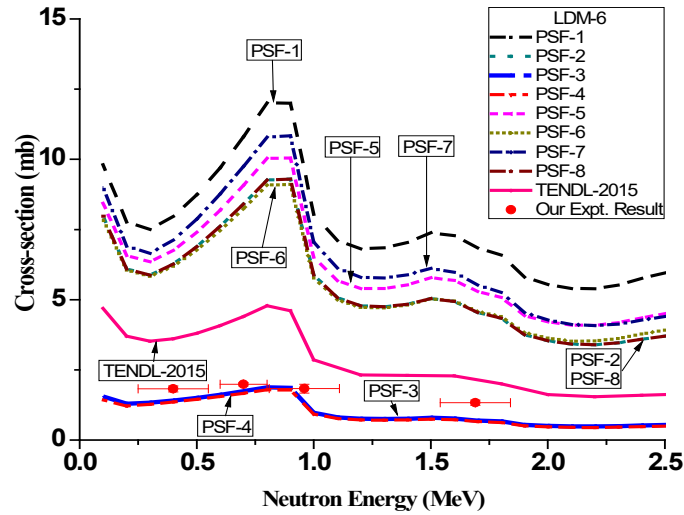
(c)



(d)



(e)



(f)

Figure 26: Excitation functions of the  $^{70}\text{Zn}(n,\gamma)^{71}\text{Zn}^m$  cross sections measured in this paper, evaluated in TENDL-2015 (solid line) as well as calculated by TALYS-1.8 with eight different Photon Strength Functions (PSF-1 to PSF-8) with the Level Density Models: (a) LDM-1 (b) LDM-2, (c) LDM-3, (d) LDM-4, (e) LDM-5 and (f) LDM-6. The experimental cross sections are  $(p,n_0)$  neutron flux energy spectrum averaged, whereas the evaluated and calculated cross sections are for monoenergetic neutrons.

The predictions of  $^{70}\text{Zn}(n,\gamma)^{71}\text{Zn}^m$  reaction cross sections at the four neutron energies by TALYS-1.8 are also compared with the predictions of TALYS-1.6. The same Level Density Model (LDM-3) and Photon Strength Functions (PSF-3 and PSF-4) used in TALYS-1.8 are also used in TALYS-1.6. Figure 27 shows that the theoretical predictions by TALYS-1.6 are much lower compared to theoretical predictions by TALYS-1.8 even though the same set of input parameters and nuclear models are used. Our previous work demonstrates that LDM-3 and LDM-1 (Kopecky-Uhl) are the best combination to reproduce our cross sections at 0.96 and 1.69 MeV by TALYS-1.6.

Interpreting data and understanding the accompanying theoretical models often requires a statistical analysis. Very often, this analysis takes the form of a minimization of a function,  $\chi^2$ . As the measured cross sections have been determined with their covariances, it is possible to quantify the model prediction capability by estimating

$$\chi^2 = (\sigma_{\text{exp}} - \sigma_{\text{mod}})^t V^{-1} (\sigma_{\text{exp}} - \sigma_{\text{mod}})$$

Where  $\sigma_{\text{exp}}$  and  $\sigma_{\text{mod}}$  are 1x4 column vectors which consist of the cross sections at four energies from the experiment and model respectively, and V is the 4x4 covariance matrix of the measured cross sections. TALYS-1.6 (LDM-3+PSF-1) and TALYS-1.8 (LDM-3+PSF-3) give  $\sqrt{(\chi^2 / 4)} = 6.3$  and 3.4 respectively.

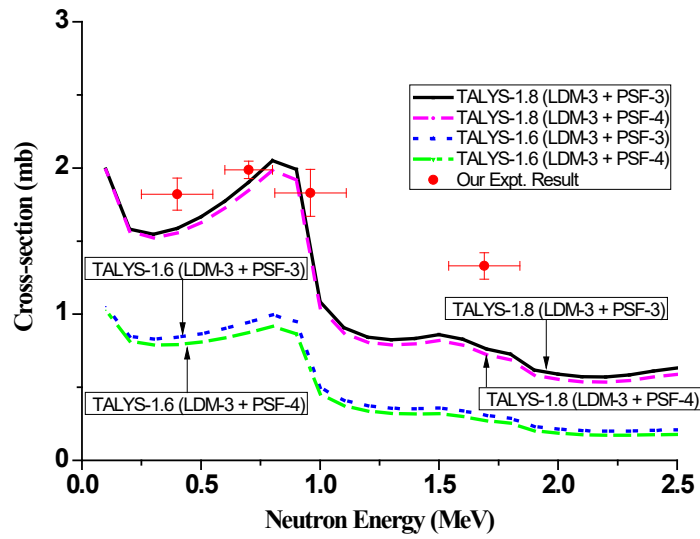


Figure 27: Comparison between predictions of  $^{70}\text{Zn}(n,\gamma)^{71}\text{Zn}^m$  reaction cross sections at neutron energies 0.40, 0.70, 0.96 and 1.69 MeV by TALYS-1.6 and TALYS-1.8 with two different Photon Strength Functions (PSF-3 and PSF-4) and the Level Density Model 3 (LDM-3) respectively.



**CHAPTER – 6**  
**SUMMARY AND CONCLUSIONS**

## SUMMARY AND CONCLUSIONS

The  ${}^7\text{Li}(p,n){}^7\text{Be}$  reaction is widely used as quasi-monoenergetic neutron source because it produces large amount of relatively low energy neutrons. This neutron source reaction has been utilized for experimental studies of several neutron-induced reactions. It is also a strong candidate as small accelerator-based neutron sources for Boron Neutron Capture Therapy (BNCT) which is a cancer treatment modality.

In India, the 14 UD Pelletron Accelerator at the Tata Institute of Fundamental Research, Mumbai (BARC-TIFR Pelletron) and Folded Tandem Ion Accelerator at the Bhabha Atomic Research Centre (BARC-FOTIA) are currently the main accelerators serving as  ${}^7\text{Li}(p,n){}^7\text{Be}$  neutron sources for neutron induced reaction cross-section measurements. But the time-of-flight and multiple foil activation techniques cannot be applied at these accelerators due to the continuous beam structure and weak neutron flux. As a result, experimentalists using these accelerators have to rely on calculated neutron energy spectra for subtraction of the  ${}^7\text{Li}(p,n_1){}^7\text{Be}$  contribution whose cross sections can be very pronounced as they have lower neutron energies. Therefore, the  ${}^7\text{Li}(p,n){}^7\text{Be}$  neutron spectra below the three-body break up reaction threshold was studied by developing a new deterministic neutron energy spectrum code Energy of Proton Energy of Neutron-EPEN.

To examine the approach near the threshold region, thick target  ${}^7\text{Li}(p,n_0){}^7\text{Be}$  neutron spectrum at  $E_p = 1912\text{keV}$  was compared with those measured by Lederer *et al.*, Ratynski *et al.* and Feinberg *et al.* The neutron spectrum produced by EPEN agrees well with the measured spectra except for broader low- and high- energy tail observed by Feinberg *et al.* which is due to the relatively thick  ${}^6\text{Li}$ -glass detector and its effects on the time-of-flight resolution.

EPEN result was also compared with Kononov *et al.*'s experimental result of zero degree neutron yield for  ${}^7\text{Li}(p,n){}^7\text{Be}$  reaction near threshold, for a thick lithium target. But there is a mismatch of the peak position by 5 keV between EPEN and Kononov *et al.* experimental zero degree neutron yield and also, EPEN underestimates the experimental result throughout the whole energy range as long as the finite detector solid angle was not considered. The cause of this disagreement was studied by calculating the neutron energy spectra with various angular range covered by the detector and the best agreement with experimental spectrum was observed when  $\pm 5^\circ$  was chosen. To further confirm this, the calculated spectrum was also compared with Feinberg *et al.* experimental spectrum at  $E_p=1912\pm 1.5$  keV and the peak position of EPEN result and experimental spectra exactly match. The overestimation by EPEN around 100 keV was also reported by Herrera *et al.*

EPEN result was also compared with the ones reported by Lefevre and Din for  $E_p = 3450$  keV and  $E_p = 2520$  keV, respectively, for a thick LiF target. Lefevre and Din did not specify the incident proton beam energy spread. EPEN calculation at 3450 keV with zero beam spread did not match the experimental higher neutron energy tail as well as the first excited state edge but the recalculation with 30-keV beam energy spread well reproduces the first excited state edge as well as the higher-energy tail of the experimental result in the case of  $E_p = 3450$  keV. Similarly, at  $E_p = 2520$  keV, EPEN neutron spectrum did not match the experimental result but the two results matches very well when one uses a proton beam spread of  $\pm 10$  keV.

Besides validating EPEN results with the available experimental results, the neutron spectra were compared with the theoretical neutron spectra reported by Ritchie at  $E_p = 2400$  and 2800 keV for a thick natural lithium target where the protons slowed down below the  $(p,n_0)$  reaction threshold inside the lithium target. The comparison in absolute units matches

very well at both these energies for ground state as well as first excited state neutron spectra although certain discrepancies are found around 100 keV.

There are some Monte Carlo codes such as PINO and SimLiT for the calculation of neutron energy spectrum using  ${}^7\text{Li}(p,n){}^7\text{Be}$  reaction as neutron source. The neutron energy spectra produced by EPEN was compared with the results produced by PINO and SimLiT at proton energies 2800 and 3500 keV with proton beam spread of 20 keV. The configurations used in the three codes are similar and the thickness of the natural lithium target is 38  $\mu\text{m}$ . The comparison result shows that there is a perfect match between EPEN and SimLiT neutron energy spectra for both the ground state and first excited state contributions. However, the result produced by PINO shows large discrepancy from the other two codes for both ground state and first excited state contributions. For the ground state neutron spectra, EPEN reproduces the same result as that of PINO if the necessary weighting function for the proton beam spread is ignored. Similarly, for the first excited state contribution, a much sharper spectrum is produced by PINO as if the thickness of the lithium target is thinner than the given one.

The disagreement shown by PINO is further studied by comparing the three codes again at proton energies 2800 and 3500 keV with a beam spread of 20 keV. The configurations used are similar as the previous case except for the lithium thickness which had been increased from 38  $\mu\text{m}$  to 60  $\mu\text{m}$ . Similar to the previous case, EPEN and SimLiT shows a perfect match whereas PINO shows certain discrepancy for both the ground state and first excited state neutrons. While the increase in the thickness of the lithium target was expected to increase the neutron energy range, the energy range covered by the first excited state neutrons in case of PINO remains the same. This means that PINO has a problem in the treatment of not only the ground state neutrons but also with the first excited state neutrons. The problem detected in the treatment of ground state neutrons by PINO are confirmed by

further comparing the results produced by the three codes at the same neutron energies i.e. 2800 and 3500 keV. In the present case, the proton beam spread is treated negligible. The three codes produce the same result which clearly shows that there is a serious problem with PINO simulation when it considers finite beam energy spread.

The present work reveals that the deterministic approach works well for description “ideal”  ${}^7\text{Li}(p,n_0){}^7\text{Be}$  neutron source systems (e.g., pencil proton beam, no surrounding material) and usable to study physics of the neutron source system (e.g., validation of  ${}^7\text{Li}(p,n_0){}^7\text{Be}$  microscopic nuclear data by thick target neutron spectra). Its output can be used as an input to the Monte Carlo particle transport codes to describe more complicated neutron source systems.

For all users around the globe, EPEN is now freely available at Mizoram University website (<http://www.epen.nhergmzu.com/epen/>).

The  ${}^{70}\text{Zn}(n,\gamma){}^{71}\text{Zn}$  reaction cross sections have been measured for the first time in the just below and above the inelastic scattering threshold energy. The standard activation technique was used and the  ${}^7\text{Li}(p,n){}^7\text{Be}$  reaction was used as the neutron source. The experiment was carried out at the Folded Tandem Ion Accelerator (FOTIA) Facility, Nuclear Physics Division, Bhabha Atomic Research Centre (BARC), Mumbai and the proton energies bombarding the lithium targets were 2.25 MeV and 2.6 MeV. The mean energies of the (p,n<sub>0</sub>) neutron groups were obtained from the neutron energy spectrum code Energy of Proton Energy of Neutron (EPEN) and the mean neutron energies obtained were 0.40 MeV and 0.70 MeV at proton energies 2.25 and 2.6 MeV respectively. Subtractions of the first excited state and breakup neutron contributions are an essential part in experimental determination of neutron-induced reaction cross section and therefore, subtraction of these contributions are carried out using the code EPEN. The data analysis was carried out using the latest decay

data in the ENSDF library and  $^{197}\text{Au}(n,\gamma)^{198}\text{Au}$  cross sections in the IAEA Neutron Cross Section Standards.

During the whole irradiation period, the neutron flux was recorded and saved after every 30 minutes to get the neutron flux fluctuation. The gamma-ray activity was measured using a pre-calibrated lead shielded 185 cc high purity germanium (HPGe) detector having 30% relative efficiency, and 1.8 keV energy resolutions at 1.33 MeV gamma-energy. The data acquisition was carried out using CAMAC based LAMPS (Linux Advanced Multi Parameter System) software (TCAMCON-95/CC 2000 crates controller and CM-48 ADCs). Due to low count rate of  $^{71}\text{Zn}^m$ , the foil stack was placed very close to the detector to obtain high count rate. However, it introduces the coincidence-summing effect. In order to correct the measured efficiency for the coincidence summing effect, the correction factor  $K_c$  was calculated using the Monte Carlo simulation code EFFTRAN. The data analysis was carried out using the latest decay data, and by taking into account the neutron flux fluctuation due to proton current fluctuation during irradiation, low energy (p,n<sub>1</sub>) neutron backgrounds coming from the neutron population of the first excited state of  $^7\text{Be}$ , scattered neutron background originating from elastic, inelastic and multiple scattering in the foil stack and surrounding materials, and gamma self-attenuation due to a gamma photon during its passes through any material, including the sample in which it was generated, underwent specific interactions which attenuated the photon either by absorption or scattering with losing energy partially or totally. The uncertainty propagation from various sources of the uncertainty and correlation for the present work at 0.40 MeV and 0.70 MeV neutron energies along with our earlier reported work at 0.96 MeV and 1.69 MeV was also performed, and the total and partial uncertainties of the measured cross sections at the four neutron energies were reported with their correlations.

The  $^{70}\text{Zn}(n,\gamma)^{71}\text{Zn}^m$  reaction cross section was calculated theoretically using the computer code TALYS-1.8 from 0.1 MeV to 2.5 MeV neutron energies. Various Level Density Models and Photon Strength Functions available in TALYS-1.8 were used. The result of the theoretical calculation was compared with the cross sections determined at our present work at neutron energies 0.40 MeV and 0.70 MeV and our earlier reported cross sections at 0.96 MeV and 1.69 MeV. The comparison result shows that TALYS-1.8 with the generalized superfluid level model (LDM-3) with Photon Strength Functions 3 and 4 as shown in Figure 27(c) best matches the measured cross sections at neutron energies 0.40, 0.70 and 0.96 MeV. The cross section at neutron energy 1.69 MeV is slightly underestimated by the theoretical calculation by TALYS-1.8. The predictions of  $^{70}\text{Zn}(n,\gamma)^{71}\text{Zn}^m$  reaction cross sections at the four neutron energies by TALYS-1.8 are also compared with the predictions of TALYS-1.6. The same Level Density Model (LDM-3) and Photon Strength Functions (PSF-3 and PSF-4) used in TALYS-1.8 are also used in TALYS-1.6. Figure 28 shows that the theoretical predictions by TALYS-1.6 are much lower compared to theoretical predictions by TALYS-1.8 even though the same set of input parameters and nuclear models are used.

## References

- Abusaleem K. and Singh B., (2011), “Nuclear Data Sheets for A= 71”, *Nucl. Data Sheets***112**, 133-273.
- Alhassan Erwin, (2015), “Nuclear data uncertainty quantification and data assimilation for a lead-cooled fast reactor”, A Dissertation submitted at Uppsala University for the degree of Doctor of Philosophy.
- Axel P., (1962), “Electric dipole ground-state transition width strength function and 7-MeV photon interactions”, *Phys. Rev.*, **126**, 671-683.
- Bethe H. A., (1936), “An Attempt to Calculate the Number of Energy Levels of a Heavy Nucleus”, *Physical Review*, **50**, 332.
- Birgersson E. and Lövestam G., (2009) , “Computer Code NeuSDesc,” EUR 23794 EN, Joint Research Centre—Institute for Reference Materials and Measurements.
- Blachot J., (2012), “Nuclear Data Sheets for A = 115”, *Nucl. Data Sheets*, **113**, 10, 2391-2535.
- Brink D.M., (1957), “Individual particle and collective aspects of the nuclear photoeffect”, *Nucl. Phys.*, **4**, 215-220.
- Burbidge, E. M., Burbidge, G. R., Fowler, W. A., & Hoyle, F., Rev., (1957), “Synthesis of the elements in stars”, *Mod. Phys.*, **29**, 547-650.
- Capote R., Herman M., Oblozinsky P., Young P.G., Goriely S., Belgia T., Ignatyuk A.V., Koning A.J., Hilaire S., Plujko V., Avrigeanu M., Bersillon O., Chadwick M.B., Fukahori T., Kailas S., Kopecky J., Maslov V.M., Reffo G., Sin M., Soukhovitskii E., Talou P., Han Yinlu, and GeZhigang, (2009), “Reference Input Parameter Library (RIPL-3)”, *Nucl. Data Sheets*, **110**, 3107- 3214.
- Carlson A.D., Pronyaev V.G., Smith D.L., Larson, Zhenpeng Chen N.M., Hale G.M., Hamsch F.-J., Gai E.V., Soo-Youl Oh, Badikov S.A., Kawano T., Hofmann H.M., Vonach H., and Tagesen S., (2009), “International evaluation of neutron cross section standards”, *Nucl. Data Sheets*, **110**, 3215-3324.



- Chaudhri M. A., Templer J. and Rouse J. L., (1979), “The  ${}^7\text{Li}(p,n){}^7\text{Be}$  reaction as a source of fast neutrons for smaller compact cyclotrons”, *IEEE Transactions on Nuclear Science*, **26**, 2.
- Cohen I.M., Guevara S.R., Arribére M.A., Fornaciari Illjadic M.C., Kestelman A.J., Ohaco R.A., Segovia M.S. and Yunes A.N., (2005), “Determination of nuclear constants of reactions induced on zinc by short irradiations with the epithermal and fast components of a reactor neutron spectrum”, *Radiochim. Acta*, **93**, 543–546.
- Damon R.W., (2005), “Determination of the photo-peak detection efficiency of a HpGe detector, for volume sources, via Monte Carlo simulations”, Dissertation submitted to the University of the Western Cape.
- Drosg M., (1981), “The  ${}^7\text{Li}(n,p){}^7\text{Be}$  reaction as a neutron source in the MeV range”, Los Alamos National Laboratory, New Mexico.
- EPRI (2011), “PWR dose reduction efforts at Exelon”, Proceedings of the August 2011 EPRI PWR Primary Zinc Addition Workshop, Palo Alto, August 2011, 2-9.
- Ericson T., (1960), “The statistical model and nuclear level densities”, *Adv. Phys.*, **9**, 425-511.
- Feinberg G., Friedman M., Krasa A., Shor A., Eisen Y., Berkovits D., Cohen D., Giorginis G., Hirsh T., Paul M., Plompen A. J. M. and Tsuk E., (2012), “Quasi-Stellar Neutrons from the  ${}^7\text{Li}(p,n){}^7\text{Be}$  Reaction with an Energy-Broadened Proton Beam”, *Phys. Rev. C*, **85**, 055810.
- Fessler A., Plompen A.J.M., Smith D.L., Meadows J.W., and Ikeda Y., (2000), “Neutron activation cross-section measurements from 16 to 20 MeV for Isotopes of F, Na, Mg, Al, Si, P, Cl, Ti, V, Mn, Fe, Nb, Sn, and Ba”, *Nucl. Sci. Eng.*, **134**, 171-200.
- Friedman M., Cohen D., Paul M., Berkovits D., Eisen Y., Feinberg G., Giorginis G., Halfon S., Krasa A., Plompen A.J.M. and Shor A., (2013), “Simulation of the Neutron Spectrum from the  ${}^7\text{Li}(p,n)$  Reaction with a Liquid-Lithium Target at Soreq Applied Research Accelerator Facility,” *Nucl. Instrum. Methods Phys. Res. A*, **698**, 117-126.

- Furusaka M., Niita K., Suzuki S., Fujita K., Suzuki J., Oku T., Shimizu H. M., Otomo T. and Misawa M., (2004), “Monte-Carlo simulation codes development and their applications to neutron optical devices and neutron scattering instruments”, *NuclInstrum Meth A*, **529**, 223–230.
- Gasper Zerovnik, (2012), “Use of covariance matrices for estimating uncertainties in reactorCalculations”, Doctoral Dissertation submitted to the University of Ljubljana.
- Gibbons J. H. and Macklin R. L., (1959), “Total Neutron Yields from Light Elements Under Proton and Alpha Bombardment”, *Phys. Rev.*, **114**, 571.
- Gilbert A. and Cameron A.G.W., (1965), “A composite nuclear-level density formula with shell corrections”, *Can. J. Phys.*, **43**, 1446-1496.
- Glascock Michael, (2003), “An overview of Neutron Activation Analysis”, Book, University of Missouri Research Reactor.
- Goriely S., Hilaire S. and Koning A.J., (2008), “Improved microscopic nuclear level densities within the Hartree-Fock-Bogoliubov plus combinatorial method”, *Phys. Rev. C*, **78**, 064307.
- Goriely S., Tondeur F., Pearson J.M., (2001), “A Hartree–Fock nuclear mass table”, *Atom. Data Nucl. Data Tables*, **77**, 311-381.
- Goriely S., Hilaire S., Koning A.J., and Capote R., (2011), “Towards improved evaluation of neutron induced fission cross section”, Proceedings of the International Conference on Nuclear Data for Science and Technology, *Journ. Kor. Phys. Soc.*, **59**, 23, 979-982.
- Gunsing, F., Aberle, O., Andrzejewski, J., Audouin, L., Bécáres, V., MBacák, M., Balibrea-Correa, J., Barbagallo, M., Barros, S., Bečvář, F., Beinrucker, C., Belloni, F., Berthoumieux, E., Billowes, J., Bosnar, D., Brugger, M., Caamaño, M., Calviño, F., Calviani, M., Cano-Ott, D. and Cardella, R., (2015), “Nuclear Data Measurements At The Upgraded Neutron Time-Of-Flight Facility N-TOF At CERN”, *14th International Conference on Nuclear Reaction Mechanisms, Villa Monastero, Varenna, Italy*, 323-330.

- Hauser W. and Feshbach H., (1952), “The Inelastic Scattering of Neutrons”, *Phys. Rev.*, **87**, 366-373.
- Herman, M., Capote, R., Carlson, B.V., Oblozinsky, P., Sin, M., Trkov, A., Wienke, H., & Zerkin, V. (2007). EMPIRE: Nuclear Reaction Model Code System for Data Evaluation. *Nuclear Data Sheets*, 108(12), 2655-2715. doi:101016/jnds200711003
- Herrera M. S., Moreno G. A. and Kreiner A. J., (2015), “New Method to Evaluate the  ${}^7\text{Li}(p,n){}^7\text{Be}$  Reaction near Threshold”, *Nucl. Instrum. Methods Phys. Res. B*, **349**, 64-71.
- Hilaire S. and Girod M., (2012), “Temperature-dependent combinatorial level densities with the DIM Gogny force”, *Phys. Rev. C*, **86**, 064317.
- Huang Xiaolong, (2009), “Nuclear Data Sheets for A = 198”, *Nucl. Data Sheets*, **110**, 2533-2688.
- Iwamoto Y., Niita K., Sawai T., Ronningen R. M. and Baumann T., (2012), “Improvement of radiation damage calculation in PHITS and tests for copper and tungsten irradiated with protons and heavy-ions over a wide energy range”, *NuclInstrum Meth B*, **274**, 57–64.
- Jackman K.R., (2007), “KMESS: An Open Source Software Package Using a Semi-empirical Mesh-Grid Method for the Modelling of Germanium Detector Efficiencies”, Dissertation submitted to the University of Texas at Austin.
- Knoll Glenn F, (1989, 1999), “Radiation detection and measurement”, John Willey and Sons, Canada Ltd, Second and Third edition.
- Koning A.J. and Delaroche J.P., (2003), “Local and global nucleon optical models from 1 keV to 200 MeV”, *Nucl.Phys. A*, **713**, 231-310.
- Koning A.J. and Mengoni A, “WPEC Subgroup 30: Quality improvement of the EXFOR database,” (2009), NEA report number NEA/NSC/WPEC/DOC, Vol. 416. OECD/NEA Nuclear Data Bank, Paris, France.

Koning A.J., Rochman D., Kopecky J., Sublet J.Ch., Fleming M., Bauge, E., Hilaire S., Romain P., Morillon B., Duarte H., van der Marck S.C., Pomp S., Sjostrand H., Forres R., Henriksson H., Cabellos O., Goriely S., Leppanen J., Leeb H., Plompen A., and Mills R., (2015), "TENDL-2015 : TALYS-based evaluated nuclear data library", [[https://tendl.web.psi.ch/tendl\\_2015/tendl2015.html](https://tendl.web.psi.ch/tendl_2015/tendl2015.html)].

Kononov V. N., Personal Communication with M. Mikhailiukova, Center Jadernykh Dannykh, Obninsk (Mar. 1, 2016). Experimental Nuclear Reaction Data, EXFOR F1267.001, International Atomic Energy Agency.

Kononov V.N., Poletaev E.D., and Yurlov B.D., (1977) "Accelerator-Based Fast Neutron Sources for Neutron Therapy," *Sov. At.Energy*, **43**, 947.

Koning A.J., Hilaire S. and Duijvestijn M.C., (2008a), "TALYS-1.0", Proceedings of the International Conference on Nuclear Data for Science and Technology, April 22-27, 2007, *EDP Sciences*, 211-214.

Kopecky J. and Uhl M., (1990), "Test of gamma-ray strength functions in nuclear reaction model calculations", *Phys. Rev. C*, **41**, 1941-1955.

Krane K.S., (2017), "Neutron capture cross sections of  $^{70}\text{Zn}$  and the decay of  $^{71\text{m}}\text{Zn}$ ", *Appl. Radiat.andIsot.*, **121**, 28-37.

Lalremruata B., Punte L. R. M., Otuka N., Suryanarayana S. V., Iwamoto Y., Pachua Rebecca, Satheesh B., Thanga H. H., Danu L. S., Desai V. V., Hlondo L. R., Kailas S., Ganesan S., Nayak B. K. and Saxena A., (2017), "Measurements of neutron capture cross sections on  $^{70}\text{Zn}$  at 0.96 and 1.69 MeV", International Atomic Energy Agency Report No. INDC (IND)-0049, 2017.

Larsen A.C. and Goriely S., (2010a), "Impact of a low-energy enhancement in the  $\gamma$ -ray strength function on the neutron-capture cross section", *Phys. Rev. C*, **82**, 014318.

Larsen A.C., Agvaanluvsan U., Bernstein L.A., Brger A., Chankova R., Goriely S., Guttormsen M. , Lonroth T., Mitchell G.E., Nyhus H.T., Siem S., Syed N.U.H., Toft H.K. and Voinov A., (2010b), "Soft structure of gamma-ray strength functions studied

with the Oslo method”, CNR\*09 – Second International Workshop on Compound Nuclear Reactions and Related Topics, eds. Bonneau L., Dubray N., Gunging F., Jurado B., 05 - 08 October 2009, Bordeaux, France, *Eur. Phys. J.*, **2**, 03001.

Lebois M., Wilson J.N., Halipré P., Leniau B., Matea I., Oberstedt A., Oberstedt S. and Verney D., (2014), “Development of a kinematically focused neutron source with the  $p(^7\text{Li},n)^7\text{Be}$  inverse reaction, *Nucl. Instrum. Methods Phys. Res. A*, **735**, 145–151.

Lederer C., Kappeler F., Mosconi M., Nolte R., Heil M., Reifarth R., Schmidt S., Dillmann I., Giesen U., Mengoni A. and Wallner A., (2012), “Definition of a Standard Neutron Field with the  $^7\text{Li}(p,n)^7\text{Be}$  Reaction”, *Phys. Rev. C*, **85**, 055809.

Lee C.L. and Zhou X.L., (1999), “Thick Target Neutron Yields for the  $^7\text{Li}(p,n)^7\text{Be}$  Reaction near Threshold”, *Nucl. Instrum. Methods Phys. Res. B*, **152**, 1-11.

Lefevre H. W. and Din G. U., (1969), “Zero Degree Neutron Yield from the  $^7\text{Li}(p,n)^7\text{Be}$  Reaction near 2.2 MeV”, *Aust. J. Phys.*, **22**, 669.

Liskien H. and Paulsen A., (1975), “Neutron Production Cross Sections and Energies for the Reactions  $^7\text{Li}(p,n)^7\text{Be}$  and  $^7\text{Li}(p,n)^7\text{Be}^*$ ,” *At. Data Nucl. Data Tables*, **15**, 57-84.

Macklin R. L. and Gibbons J. H., (1958), “Study of the  $\text{T}(p,n)\text{He}^3$  and  $\text{Li}^7(p, n)\text{Be}^7$  Reactions”, *Phys. Rev.*, **109**, 105.

Mangal S.K. and Gill P.S., (1962), “Thermal neutron activation cross-sections for isomer production”, *Nuclear Physics*, **36**, 542-548.

Mannhart W. and Vonach H.K., (1968), “Isomerewirkungsquerschnittsverhältnisse Beim thermischen Neutroneneinfang im Bereich der  $2p_{1/2}$  and  $1g_{9/2}$  Schalenmodellzustände (Isomeric cross section ratios for  $2p_{1/2}$  and  $1g_{9/2}$  Shell Model States formed by thermal neutron capture)”, *Zeitschrift für Physik*, **210**, 13-31.

Mannhart W., (2013), Report INDC(NDS)-0588 (Rev.), International Atomic Energy Agency.

Martin M., (2013), “Nuclear Data Sheets for  $A = 152^*$ ”, *J. Nucl. Data Sheets*, **114**, 1497-1847.

- Millsap D.W. and Landsberger S., (2015), “Self-attenuation as a function of gamma ray energy in naturally occurring radioactive material in the oil and gas industry”, *Appl. Radiat. Isot.***97**, 21-23.
- Newson H. W., Williamson R. M., Jones K. W., Gibbons J. H., and Marshak H., (1957), “Li7(p,n), (p, p'γ), and (p, γ) Reactions near Neutron Threshold”, *Phys. Rev.*, **108**, 1294.
- Niita K., Iwamoto Y., Sato T., Matsuda N., Sakamoto Y., Nakashima H., Iwase H. and Shiver L., (2011), “Event generator models in the particle and heavy ion transport code system; PHITS”, *J Korean Phys Soc.*, **59**, 827–832.
- Nose H., Niita K., Hara M., Uematsu K., Azuma O., Miyauchi Y., Komori M. and Kanai T., (2005), “Improvement of three dimensional Monte Carlo code PHITS for heavy ion therapy”, *J NuclSciTechnol*, **42**, 250–255.
- Otuka N., Lalremruata B., Khandaker M.U., Usman A.R., and Punte L.R.M., (2017), “Uncertainty propagation in activation cross section measurements”, (2017), *Radiation Physics and Chemistry*, <https://doi.org/10.1016/j.radphyschem.2017.01.013>.
- Otuka N., Dupont E., Semkova V., Pritychenko B., Blokhin A.I., Aikawa M., Babykina S., Bossant M., Chen G., Dunaeva S., Forrest R.A., Fukahori T., Furutachi N., Ganesan S., Ge Z., Gritzay O.O., Herman M., Hlavač S., Katō K., Lalremruata B., Lee Y. O., Makinaga A., Matsumoto K., Mikhaylyukova M., Pikulina G., Pronyaev V. G., Saxena A., Schwerer O., Simakov S. P., Soppera N., Suzuki R., Takács S., Tao X., Taova S., Tárkányi F., Varlamov V. V., Wang J., Yang S. C., Zerkin V. and Zhuang Y., (2014), *Nucl. Data Sheets*, **120**, 272-276.
- Paul H. and Schinner A., (2005), “Judging the Reliability of Stopping Power Tables and Programs for Protons and Alpha Particles Using Statistical Methods”, *Nucl. Instrum. Methods Phys. Res. B*,**227**, 461-470.
- Peralta, L., (2004), “Measuring the activity of a radioactive source in the classroom”, *Eur. J. Phys*, **25**, 211-219.

- Pignatari M., Gallino R., Heil M., Wiescher M., Käppeler F., Herwig F. and Bisterzo S., (2010), “The weak s-process in massive stars and its dependence on the neutron capture cross sections”, *APJ*, **710**, 1557-1577.
- Punte L. R. M., Lalremruata B., Otuka N., Suryanarayana S. V., Iwamoto Y., Pachuau Rebecca, Satheesh B., Thanga H. H., Danu L. S., Desai V. V., Hlondo L. R., Kailas S., Ganesan S., Nayak B. K. and Saxena A., (2017), “Measurements of neutron capture cross sections on  $^{70}\text{Zn}$  at 0.96 and 1.69 MeV”, *Phys. Rev. C*, **95**, 024619.
- Qaim S. M., (2010), “Radiochemical determination of nuclear data for theory and applications”, *J RadioanalNuclChem*, **284**, 489–505.
- Ratynski W. and Kappeler F., (1988), “Neutron capture cross section of Au : A standard for stellar nucleosynthesis”, *Phys. Rev. C*, **37**, 2.
- Reifarth R., Heil M., Kappeler F. and Plag R., (2009), “PINO—a tool for simulating neutron spectra resulting from the  $^7\text{Li}(p,n)$  reaction”, *Nucl. Instrum.Methods Phys. Res. A*, **608**, 139–143.
- Reifarth R., Dababneh S., Heil M., Käppeler F., Plag R., Sonnabend K. and Uberseder E., (2012), “Neutron activation of natural zinc samples at  $kT = 25$  keV”, *Phys. Rev. C*, **85**, 035802.
- Ritchie A.I.M., (1976), “Neutron yields and energy spectra from the thick target  $\text{Li}(p,n)$ Source”, *J. Phys. D: Appl. Phys.*, **9**.
- RobuE. and Giovani C., (2009), “Gamma-ray self-attenuation corrections in environmental samples”, *Rom. Rep. Phys.* **61**, 295-300.
- Rochman, D. and Koning, A. J., (2011), “How To Randomly Evaluate Nuclear Data: A New Data Adjustment Method Applied To  $^{239}\text{Pu}$ ”, *Nuclear Science and Engineering*, **169**, 68-80
- Sage C., Semkova V., Bouland O., Dessagne P., Fernandez A., Gunsing F., Nastren C., Noguere G., Ottmar H., Plompen A. J. M., Romain P., Rudolf G., Somers J. and Wastin F.,

(2010), “High resolution measurements of the  $^{241}\text{Am}(n,2n)$  reaction cross section”, *Phys. Rev. C*, **81**, 064604.

Sakaki H., Nishiuchi M., Hori T., Bolton P. R., Yogo A., Katagiri M., Ogura K., Sagisaka A., Pirozhkov A. S., Orimo S., Kondo K., Iwase H., Niita K., Souda H., Noda A., Iseki Y. and Yoshiyuki T., (2010), “Prompt in-line diagnosis of single bunch transverse profiles and energy spectra for laser accelerated ions”, *ApplPhys Express*, **3**.

Salvatores, M., Aliberti, G., Palmiotti, G., Rochman, D., Oblozinsky, P., Hermann, M., Talou, P., Kawano, T., Leal, L., Koning, A. and Kodeli, I., (2007), “Nuclear Data Needs for Advanced Reactor Systems: A NEA Nuclear Science Committee initiative”, International Conference on Nuclear Data for Science and Technology, *EDP Sciences*, 879-882.

Sato T., Kase Y., Watanabe R., Niita K. and Sihver L., (2009), “Biological dose estimation for charged-particle therapy using an improved PHITS code coupled with a microdosimetric kinetic model”, *Radiat Res.*, **171**, 107–117.

Sato T., Niita K., Matsuda N., Hashimoto S., Iwamoto Y., Noda S., Ogawa T., Iwase H., Nakashima H., Fukahori T., Okumura K., Kai T., Chiba S., Furuta, and L. Sihver T., (2013), “Particle and Heavy Ion Transport code System, PHITS, version 2.52”, *J. Nucl. Sci. Technol.*, **50**, 913-923.

Shorin V.S., (1997), “Cross-section of the reaction  $^7\text{Li}(p, n)^7\text{Be}$  close to the threshold”, INDC(CCP)-**0403**, 55-65.

Stanga D. and Muntele I., (2000), “ Importance of covariances for uncertainty estimates in measurement of radionuclide mixtures by multichannel counting”, *Applied Radiation and Isotopes*, **52**, 621-626.

Strauss Michael G., Sherman Irvin S., Cattelino Mark J., Brenner Raul and Pehl Richard H., (1977), “Intrinsic efficiency of germanium - a basis for calculating expected detector efficiency\*”, *IEEE Transactions on Nuclear Science*, **24**, 1.



- The L. -S., Mounib F. El Eid and Bradley S. Meyer, (2007), “s-Process Nucleosynthesis in Advanced Burning Phases of Massive Stars”, *ApJ*, **655**, 1058-1078.
- Theobald J. P., Migneco E. and Cervini C., (1971), “Neutron Intensities from Proton Bombarded Thick Lithium Targets”, *Nucl.Instrum. Methods*, **95**, 1-4.
- Tilley D. R., Kelley J.H., Godwin J.L., Millener D.J., Purcell J.E., Sheu C.G. and Weller H.R., (2004), “Energy Levels of Light Nuclei A= 8, 9, 10”, *Nucl. Phys. A*, **745**, 155-362.
- Vidmar T., (2005), —EFFTRAN—“A Monte Carlo efficiency transfer code for gamma-ray Spectrometry”, *Nucl.Instrum.Meth. A*, **550**, 603-608.
- Winter J., (1968), “A Simplified Method for Kinematic Calculations of Nuclear Reactions”, *Nucl.Instrum.Methods*, **59**, 167-169.
- Ziegler J. F. and Biersack J. P., (2013), “SRIM—The Stopping and Range of Ions in Matter,” SRIM-2013.00 Version.

## Appendix

APPENDIX 1: Group-wise fractional neutron fluxes, monitor cross sections and their corresponding uncertainties for  $\langle E_n \rangle = 0.40, 0.70, 0.96$  and  $1.69$  MeV adopted in the present work.

Group k	$E_{\min}$ (MeV)	$E_{\max}$ (MeV)	$\sigma_k$ (mb)	$\Delta\sigma_k$ (%)	$\Phi_{i,k} / \sum \Phi_{i,k}$			
					0.40 MeV (i=1)	0.70 MeV (i=2)	0.96 MeV (i=3)	1.69 MeV (i=4)
18	0.0900	0.0975	324.56	0.98	$7.139 \times 10^{-08}$			
19	0.0975	0.1100	314.64	1.02	$6.948 \times 10^{-06}$			
20	0.1100	0.1350	293.85	0.96	$2.300 \times 10^{-04}$			
21	0.1350	0.1600	277.02	0.99	$1.913 \times 10^{-03}$			
22	0.1600	0.1750	266.89	1.14	$4.067 \times 10^{-03}$			
23	0.1750	0.1850	262.62	2.30	$5.133 \times 10^{-03}$			
24	0.1850	0.1950	256.99	1.35	$7.717 \times 10^{-03}$			
25	0.1950	0.2050	252.97	1.40	$1.053 \times 10^{-02}$			
26	0.2050	0.2150	249.01	1.29	$1.313 \times 10^{-02}$			
27	0.2150	0.2250	246.78	1.31	$1.515 \times 10^{-02}$			
28	0.2250	0.2325	243.96	1.58	$1.308 \times 10^{-02}$			
29	0.2325	0.2375	239.11	1.29	$8.423 \times 10^{-03}$			
30	0.2375	0.2425	236.41	1.83	$8.509 \times 10^{-03}$			
31	0.2425	0.2475	236.86	1.27	$8.523 \times 10^{-03}$			
32	0.2475	0.2550	236.70	1.38	$1.185 \times 10^{-02}$			
33	0.2550	0.2650	235.67	1.31	$1.658 \times 10^{-02}$			
34	0.2650	0.2750	230.12	1.63	$1.604 \times 10^{-02}$			
35	0.2750	0.2900	215.25	1.29	$2.334 \times 10^{-02}$			
36	0.2900	0.3125	198.89	1.17	$3.603 \times 10^{-02}$			
37	0.3125	0.3375	188.45	1.15	$4.033 \times 10^{-02}$			
38	0.3375	0.3625	178.70	1.07	$4.684 \times 10^{-02}$			
39	0.3625	0.3875	169.55	1.05	$5.890 \times 10^{-02}$			
40	0.3875	0.4125	162.43	1.03	$7.684 \times 10^{-02}$			
41	0.4125	0.4375	154.97	1.18	$1.066 \times 10^{-01}$			
42	0.4375	0.4625	146.65	1.00	$1.376 \times 10^{-01}$			
43	0.4625	0.4875	141.56	1.06	$1.579 \times 10^{-01}$	$1.037 \times 10^{-05}$		
44	0.4875	0.5100	136.90	1.05	$1.115 \times 10^{-01}$	$3.881 \times 10^{-04}$		
45	0.5100	0.5300	130.30	1.10	$4.825 \times 10^{-02}$	$3.383 \times 10^{-03}$		
46	0.5300	0.5550	124.49	1.18	$1.393 \times 10^{-02}$	$2.350 \times 10^{-02}$		

---

47	0.5550	0.5850	119.09	1.51	$1.037 \times 10^{-03}$	$8.302 \times 10^{-02}$	
48	0.5850	0.6250	108.87	1.08		$1.563 \times 10^{-01}$	
49	0.6250	0.6750	100.47	1.26		$1.816 \times 10^{-01}$	
50	0.6750	0.7250	96.23	1.13		$1.590 \times 10^{-01}$	$5.730 \times 10^{-10}$
51	0.7250	0.7750	93.81	1.30		$1.424 \times 10^{-01}$	$2.746 \times 10^{-05}$
52	0.7750	0.8250	88.93	1.05		$1.311 \times 10^{-01}$	$9.641 \times 10^{-03}$
53	0.8250	0.8750	85.57	1.63		$9.894 \times 10^{-02}$	$1.231 \times 10^{-01}$
54	0.8750	0.9200	84.70	2.18		$1.992 \times 10^{-02}$	$1.975 \times 10^{-01}$
55	0.9200	0.9500	85.22	1.93		$4.215 \times 10^{-04}$	$1.314 \times 10^{-01}$
56	0.9500	0.9700	85.23	4.24		$8.025 \times 10^{-07}$	$8.559 \times 10^{-02}$
57	0.9700	0.9900	84.97	3.18			$8.430 \times 10^{-02}$
58	0.9900	1.0500	79.71	1.04			$2.438 \times 10^{-01}$
59	1.0500	1.1750	77.63	1.39			$1.247 \times 10^{-01}$
60	1.1750	1.3250	73.84	1.26			$2.884 \times 10^{-07}$
61	1.3250	1.5000	70.88	1.72			$1.018 \times 10^{-06}$
62	1.5000	1.7000	67.41	1.51			$5.295 \times 10^{-01}$
63	1.7000	1.9000	60.17	2.04			$4.705 \times 10^{-01}$
64	1.9000	2.1000	52.62	1.63			$3.030 \times 10^{-08}$

---

APPENDIX 2: The 44x39 covariance matrix obtained from IAEA Neutron Cross-Section Standards for the neutron energies 0.40 MeV and 0.70 MeV. Only the lower part of the triangular matrix is presented.  $C_{ij}$  represents the matrix element.

**$C_{0,j}$  where  $0 \leq j < 1$ :**

100

**$C_{1,j}$  where  $0 \leq j < 2$ :**

71.01 100

**$C_{2,j}$  where  $0 \leq j < 3$ :**

39.5 47.36 100

**$C_{3,j}$  where  $0 \leq j < 4$ :**

30.79 30.44 40.4 100

**$C_{4,j}$  where  $0 \leq j < 5$ :**

24.08 24.04 25.94 46.32 100

**$C_{5,j}$  where  $0 \leq j < 6$ :**

13.03 12.95 13.81 18.01 24.86 100

**$C_{6,j}$  where  $0 \leq j < 7$ :**

20.49 20.47 22.65 24.72 48.3 22.24 100

**$C_{7,j}$  where  $0 \leq j < 8$ :**

19.15 18.85 20.84 19.54 32.38 18.71 43.75 100

**$C_{8,j}$  where  $0 \leq j < 9$ :**

21.68 21.39 23.48 22.32 26.42 15.22 43.13 40.81 100

**$C_{9,j}$  where  $0 \leq j < 10$ :**

20.8 20.56 22.68 22.71 21.76 15.17 39.45 41.62 55.18 100

**$C_{10,j}$  where  $0 \leq j < 11$ :**

17.35 17.19 19.08 18.9 15.13 11.39 23.45 25.65 35.37 45.17 100

**$C_{11,j}$  where  $0 \leq j < 12$ :**

21.55 21.16 23.29 22.83 17.85 11.57 23.3 28.33 42.56 49.08 46.97 100

**$C_{12,j}$  where  $0 \leq j < 13$ :**

14.62 14.38 16.31 16 13.29 7.884 14.96 18.86 26.66 34.28 36.06 44.66 100

**$C_{13,j}$  where  $0 \leq j < 14$ :**

22.08 21.74 23.85 22.67 18.77 10.48 19.34 23.48 34.02 38.86 33.49 55.13 35.55  
100

**$C_{14,j}$  where  $0 \leq j < 15$ :**

19.4 19.24 22.27 20.91 17.68 9.037 13.58 16.27 25.15 30.58 30.66 40.9 33.71  
50.46 100

**$C_{15,j}$  where  $0 \leq j < 16$ :**

20.45 20.21 22.69 22.26 20.17 10.27 15.63 17.02 24.23 34.26 30.69 40.31 34.16  
43.11 44.55 100

**C<sub>16,j</sub> where 0 ≤ j < 17:**

16.01	16	18.56	17.33	16.26	8.196	14.49	10.42	15.69	19.87	21.11	27.13	24.32
	28	33.08	46.91	100								

**C<sub>17,j</sub> where 0 ≤ j < 18:**

20.96	20.78	23.2	22.58	21.25	11.39	19.66	16.62	16.24	21.88	24.36	29.24	25.56
	33.29	33.38	52.58	49	100							

**C<sub>18,j</sub> where 0 ≤ j < 19:**

21.68	21.46	24.03	23.12	20.34	10.65	18.63	18.14	19.61	18.19	15.94	23.21	18.06
	29.42	26.48	36.82	32.15	47.6	100						

**C<sub>19,j</sub> where 0 ≤ j < 20:**

21.13	20.9	23.36	22.9	20.75	10.9	18.18	18.08	19.44	19.23	15.46	17.73	11.63
	18	17.89	26.49	24.6	38.52	56.18	100					

**C<sub>20,j</sub> where 0 ≤ j < 21:**

21.55	21.41	23.83	23.43	22.24	11.54	18.9	18.05	19.28	19.35	16.05	19.02	12.9
	19.49	17.03	18.5	17.54	28.73	39.32	57.05	100				

**C<sub>21,j</sub> where 0 ≤ j < 22:**

19.89	19.71	22.46	22.02	20.33	10.19	17.59	17.01	18.05	18.02	15.08	18.31	12.75
	18.93	16.96	19.13	14.82	17.67	27.16	41.15	56.54	100			

**C<sub>22,j</sub> where 0 ≤ j < 23:**

20.85	20.66	24.46	23.76	21.45	10.73	18.77	18.65	19.16	19.19	16.09	19.39	14.12
	19.94	19.41	20.7	17.6	21.31	20.27	28.66	40.29	56.26	100		

**C<sub>23,j</sub> where 0 ≤ j < 24:**

18.09	17.9	20.77	20.26	18.42	9.489	16.21	15.88	16.77	16.69	13.87	16.77	11.88
	17.27	16.02	17.31	14.35	17.9	18.41	17.2	30.49	41.79	54.54	100	

**C<sub>24,j</sub> where 0 ≤ j < 25:**

20.1	19.95	23.39	22.7	20.63	10.42	18.35	17.78	19.02	18.88	15.81	18.88	13.45
	19.08	18.12	19.43	16.4	20.24	21.57	20.3	24.72	35.53	48.64	55.97	100

**C<sub>25,j</sub> where 0 ≤ j < 26:**

19.18	19.12	21.97	21.84	20.6	10.49	17.68	17.05	18.01	17.78	15.04	17.86	12.36
	18.47	17	18.09	15.02	19.65	21.59	22	21.57	27.53	36.35	41.88	55.72
												100

**C<sub>26,j</sub> where 0 ≤ j < 27:**

20.23	20.11	23.17	22.92	20.75	10.57	17.86	17.98	18.77	18.57	15.66	18.87	13.13
	19.48	18.35	18.87	15.28	19.71	22.32	23.34	25.32	21.41	31.28	34.91	46.65
												60.33
												100

**C<sub>27,j</sub> where 0 ≤ j < 28:**

18.62	18.46	21.04	21.26	19.14	9.611	16.49	16.48	17.49	17.26	14.62	17.71	12.43
	17.8	16.08	17.66	14.08	18.24	20.57	21.92	23.93	22.14	23.77	27.08	38.85
												49.15
												61.98
												100

**C<sub>28,j</sub> where 0 ≤ j < 29:**

17.28 17.19 19.61 20.36 20.25 9.428 17 15.95 15.86 17.11 13.54 15.64 11.21  
 16.31 15.18 17.02 13.37 18.13 18.42 19.52 22.19 22 20.93 21.85 31.88  
 44.26 49.84 56.75 100

**C<sub>29,j</sub> where 0 ≤ j < 30:**

12.17 12.12 13.83 14.83 13.44 6.607 11.62 11.56 11.84 12.15 10.22 11.87 8.863  
 11.45 10.46 12.46 10.04 12.69 13.76 14.41 15.51 15.73 15.6 15.4 19.23  
 22.31 27.86 38.11 29.73 100

**C<sub>30,j</sub> where 0 ≤ j < 26:**

19.18 19.12 21.97 21.84 20.6 10.49 17.68 17.05 18.01 17.78 15.04 17.86 12.36  
 18.47 17 18.09 15.02 19.65 21.59 22 21.57 27.53 36.35 41.88 55.72  
 100

**C<sub>31,j</sub> where 0 ≤ j < 27:**

20.23 20.11 23.17 22.92 20.75 10.57 17.86 17.98 18.77 18.57 15.66 18.87 13.13  
 19.48 18.35 18.87 15.28 19.71 22.32 23.34 25.32 21.41 31.28 34.91 46.65  
 60.33 100

**C<sub>32,j</sub> where 0 ≤ j < 28:**

18.62 18.46 21.04 21.26 19.14 9.611 16.49 16.48 17.49 17.26 14.62 17.71 12.43  
 17.8 16.08 17.66 14.08 18.24 20.57 21.92 23.93 22.14 23.77 27.08 38.85  
 49.15 61.98 100

**C<sub>33,j</sub> where 0 ≤ j < 29:**

17.28 17.19 19.61 20.36 20.25 9.428 17 15.95 15.86 17.11 13.54 15.64 11.21  
 16.31 15.18 17.02 13.37 18.13 18.42 19.52 22.19 22 20.93 21.85 31.88  
 44.26 49.84 56.75 100

**C<sub>34,j</sub> where 0 ≤ j < 30:**

12.17 12.12 13.83 14.83 13.44 6.607 11.62 11.56 11.84 12.15 10.22 11.87 8.863  
 11.45 10.46 12.46 10.04 12.69 13.76 14.41 15.51 15.73 15.6 15.4 19.23  
 22.31 27.86 38.11 29.73 100

**C<sub>35,j</sub> where 0 ≤ j < 31:**

15.41 15.4 17.72 18.13 17.27 8.505 14.81 14.6 14.63 15.18 12.75 14.62 10.77  
 14.65 13.26 15.49 12.67 16.31 17.74 18.78 20.98 21.36 21.72 19.44 22.7  
 22.51 27.86 33.66 31.91 44.68 100

**C<sub>36,j</sub> where 0 ≤ j < 32:**

13.13 13.2 15.19 15.36 14.83 7.175 12.67 12.37 12.41 12.84 10.78 12.42 9.201  
 12.46 11.36 13.29 11.21 14 15.11 15.94 17.7 17.85 18.71 16.48 19.18  
 18.78 18.79 20.29 19.07 28.61 52.87 100

**C<sub>37,j</sub> where 0 ≤ j < 33:**

14.71 14.84 17.49 17.23 17.41 8.298 14.45 13.86 13.79 14.32 12.05 13.82 10.28  
 13.96 12.87 15.14 13.67 16.05 16.79 17.46 19.53 19.28 20.55 17.41 20.48  
 19.87 19.66 17.6 19.63 21.82 36.36 46 100

**C<sub>38,j</sub> where 0 ≤ j < 34:**

12.05	12.16	14.08	14.19	13.65	6.638	11.74	11.5	11.54	11.89	9.963	11.56	8.572
	11.6	10.66	12.59	10.7	13.06	14.08	14.65	16.2	16.33	17.17	14.57	16.85
	15.93	15.9	15.39	13.09	11.54	24.99	41.87	43.9	100			

**C<sub>39,j</sub> where 0 ≤ j < 35:**

12.83	12.9	14.96	15.29	14.76	7.094	12.67	12.4	12.41	12.72	10.62	12.43	9.073
	12.65	11.41	13.39	11.2	13.88	15.36	16.11	18.32	19.05	19.36	16.53	19.44
	17.86	18.23	18.51	16.48	13.55	20.04	28.87	34.12	51.77	100		

**C<sub>40,j</sub> where 0 ≤ j < 36:**

11.21	11.22	12.63	12.88	12.2	6.351	10.67	10.58	10.55	11.04	9.111	10.59	7.937
	10.48	9.482	11.31	9.37	11.8	12.42	12.88	13.6	13.7	14.68	12.55	14.32
	13.14	13.78	13.51	12.18	11.47	13.99	11.84	20.01	28.92	33.31	100	

**C<sub>41,j</sub> where 0 ≤ j < 37:**

8.759	8.976	11.58	10.15	10.21	4.845	8.848	9.919	8.609	8.786	7.308	8.767	6.573
	8.953	8.513	10.11	11.19	10.61	11.54	10.47	10.56	11.35	14.4	11	12.62
	10.89	11.91	10.16	8.937	7.224	10.52	9.434	13.07	11.73	12.76	10.72	100

**C<sub>42,j</sub> where 0 ≤ j < 38:**

7.62	7.668	8.943	9.376	8.687	4.25	7.585	7.815	7.607	7.831	6.324	7.508	5.436
	7.617	6.866	8.173	6.526	8.246	9.356	9.47	10.36	11.02	11.61	9.957	11.42
	10.44	11	11.06	9.813	8.828	13.03	10.65	6.647	12.92	24.51	15.21	8.827
												100

**C<sub>43,j</sub> where 0 ≤ j < 39:**

5.08	5.538	5.437	4.343	3.86	1.979	3.333	2.989	3.24	2.714	1.62	2.743	0.2707
	5.488	4.493	2.332	2.113	3.05	3.564	3.271	5.845	4.89	3.987	3.995	4.014
	5.236	5.009	3.438	5.14	1.527	3.401	3.229	2.581	4.046	5.59	9.52	3.219
	6.007	100										

APPENDIX 3: The 41x43covariance matrix obtained from IAEA Neutron Cross-Section Standards for the neutron energies 0.40 MeV and 0.96 MeV. Only the lower part of the triangular matrix is presented.  $C_{i,j}$  represents the matrix element.

**$C_{0,j}$  where  $0 \leq j < 1$ :**

100

**$C_{1,j}$  where  $0 \leq j < 2$ :**

71.01 100

**$C_{2,j}$  where  $0 \leq j < 3$ :**

39.5 47.36 100

**$C_{3,j}$  where  $0 \leq j < 4$ :**

30.79 30.44 40.4 100

**$C_{4,j}$  where  $0 \leq j < 5$ :**

24.08 24.04 25.94 46.32 100

**$C_{5,j}$  where  $0 \leq j < 6$ :**

13.03 12.95 13.81 18.01 24.86 100

**$C_{6,j}$  where  $0 \leq j < 7$ :**

20.49 20.47 22.65 24.72 48.3 22.24 100

**$C_{7,j}$  where  $0 \leq j < 8$ :**

19.15 18.85 20.84 19.54 32.38 18.71 43.75 100

**$C_{8,j}$  where  $0 \leq j < 9$ :**

21.68 21.39 23.48 22.32 26.42 15.22 43.13 40.81 100

**$C_{9,j}$  where  $0 \leq j < 10$ :**

20.8 20.56 22.68 22.71 21.76 15.17 39.45 41.62 55.18 100

**$C_{10,j}$  where  $0 \leq j < 11$ :**

17.35 17.19 19.08 18.9 15.13 11.39 23.45 25.65 35.37 45.17 100

**$C_{11,j}$  where  $0 \leq j < 12$ :**

21.55 21.16 23.29 22.83 17.85 11.57 23.3 28.33 42.56 49.08 46.97 100

**$C_{12,j}$  where  $0 \leq j < 13$ :**

14.62 14.38 16.31 16 13.29 7.884 14.96 18.86 26.66 34.28 36.06 44.66 100

**$C_{13,j}$  where  $0 \leq j < 14$ :**

22.08 21.74 23.85 22.67 18.77 10.48 19.34 23.48 34.02 38.86 33.49 55.13 35.55  
100

**$C_{14,j}$  where  $0 \leq j < 15$ :**

19.4 19.24 22.27 20.91 17.68 9.037 13.58 16.27 25.15 30.58 30.66 40.9 33.71  
50.46 100

**$C_{15,j}$  where  $0 \leq j < 16$ :**

20.45 20.21 22.69 22.26 20.17 10.27 15.63 17.02 24.23 34.26 30.69 40.31 34.16  
43.11 44.55 100

**$C_{16,j}$  where  $0 \leq j < 17$ :**



16.01 16 18.56 17.33 16.26 8.196 14.49 10.42 15.69 19.87 21.11 27.13 24.32  
28 33.08 46.91 100

**C<sub>17,j</sub> where 0 ≤ j < 18:**

20.96 20.78 23.2 22.58 21.25 11.39 19.66 16.62 16.24 21.88 24.36 29.24 25.56  
33.29 33.38 52.58 49 100

**C<sub>18,j</sub> where 0 ≤ j < 19:**

21.68 21.46 24.03 23.12 20.34 10.65 18.63 18.14 19.61 18.19 15.94 23.21 18.06  
29.42 26.48 36.82 32.15 47.6 100

**C<sub>19,j</sub> where 0 ≤ j < 20:**

21.13 20.9 23.36 22.9 20.75 10.9 18.18 18.08 19.44 19.23 15.46 17.73 11.63  
18 17.89 26.49 24.6 38.52 56.18 100

**C<sub>20,j</sub> where 0 ≤ j < 21:**

21.55 21.41 23.83 23.43 22.24 11.54 18.9 18.05 19.28 19.35 16.05 19.02 12.9  
19.49 17.03 18.5 17.54 28.73 39.32 57.05 100

**C<sub>21,j</sub> where 0 ≤ j < 22:**

19.89 19.71 22.46 22.02 20.33 10.19 17.59 17.01 18.05 18.02 15.08 18.31 12.75  
18.93 16.96 19.13 14.82 17.67 27.16 41.15 56.54 100

**C<sub>22,j</sub> where 0 ≤ j < 23:**

20.85 20.66 24.46 23.76 21.45 10.73 18.77 18.65 19.16 19.19 16.09 19.39 14.12  
19.94 19.41 20.7 17.6 21.31 20.27 28.66 40.29 56.26 100

**C<sub>23,j</sub> where 0 ≤ j < 24:**

18.09 17.9 20.77 20.26 18.42 9.489 16.21 15.88 16.77 16.69 13.87 16.77 11.88  
17.27 16.02 17.31 14.35 17.9 18.41 17.2 30.49 41.79 54.54 100

**C<sub>24,j</sub> where 0 ≤ j < 25:**

20.1 19.95 23.39 22.7 20.63 10.42 18.35 17.78 19.02 18.88 15.81 18.88 13.45  
19.08 18.12 19.43 16.4 20.24 21.57 20.3 24.72 35.53 48.64 55.97 100

**C<sub>25,j</sub> where 0 ≤ j < 26:**

19.18 19.12 21.97 21.84 20.6 10.49 17.68 17.05 18.01 17.78 15.04 17.86 12.36  
18.47 17 18.09 15.02 19.65 21.59 22 21.57 27.53 36.35 41.88 55.72  
100

**C<sub>26,j</sub> where 0 ≤ j < 27:**

20.23 20.11 23.17 22.92 20.75 10.57 17.86 17.98 18.77 18.57 15.66 18.87 13.13  
19.48 18.35 18.87 15.28 19.71 22.32 23.34 25.32 21.41 31.28 34.91 46.65  
60.33 100

**C<sub>27,j</sub> where 0 ≤ j < 28:**

18.62 18.46 21.04 21.26 19.14 9.611 16.49 16.48 17.49 17.26 14.62 17.71 12.43  
17.8 16.08 17.66 14.08 18.24 20.57 21.92 23.93 22.14 23.77 27.08 38.85  
49.15 61.98 100

**C<sub>28,j</sub> where 0 ≤ j < 29:**

17.28 17.19 19.61 20.36 20.25 9.428 17 15.95 15.86 17.11 13.54 15.64 11.21  
 16.31 15.18 17.02 13.37 18.13 18.42 19.52 22.19 22 20.93 21.85 31.88  
 44.26 49.84 56.75 100

**C<sub>29,j</sub> where 0 ≤ j < 30:**

12.17 12.12 13.83 14.83 13.44 6.607 11.62 11.56 11.84 12.15 10.22 11.87 8.863  
 11.45 10.46 12.46 10.04 12.69 13.76 14.41 15.51 15.73 15.6 15.4 19.23  
 22.31 27.86 38.11 29.73 100

**C<sub>30,j</sub> where 0 ≤ j < 33:**

14.71 14.84 17.49 17.23 17.41 8.298 14.45 13.86 13.79 14.32 12.05 13.82 10.28  
 13.96 12.87 15.14 13.67 16.05 16.79 17.46 19.53 19.28 20.55 17.41 20.48  
 19.87 19.66 17.6 19.63 21.82 36.36 46 100

**C<sub>31,j</sub> where 0 ≤ j < 34:**

12.05 12.16 14.08 14.19 13.65 6.638 11.74 11.5 11.54 11.89 9.963 11.56 8.572  
 11.6 10.66 12.59 10.7 13.06 14.08 14.65 16.2 16.33 17.17 14.57 16.85  
 15.93 15.9 15.39 13.09 11.54 24.99 41.87 43.9 100

**C<sub>32,j</sub> where 0 ≤ j < 35:**

12.83 12.9 14.96 15.29 14.76 7.094 12.67 12.4 12.41 12.72 10.62 12.43 9.073  
 12.65 11.41 13.39 11.2 13.88 15.36 16.11 18.32 19.05 19.36 16.53 19.44  
 17.86 18.23 18.51 16.48 13.55 20.04 28.87 34.12 51.77 100

**C<sub>33,j</sub> where 0 ≤ j < 36:**

11.21 11.22 12.63 12.88 12.2 6.351 10.67 10.58 10.55 11.04 9.111 10.59 7.937  
 10.48 9.482 11.31 9.37 11.8 12.42 12.88 13.6 13.7 14.68 12.55 14.32  
 13.14 13.78 13.51 12.18 11.47 13.99 11.84 20.01 28.92 33.31 100

**C<sub>34,j</sub> where 0 ≤ j < 37:**

8.759 8.976 11.58 10.15 10.21 4.845 8.848 9.919 8.609 8.786 7.308 8.767 6.573  
 8.953 8.513 10.11 11.19 10.61 11.54 10.47 10.56 11.35 14.4 11 12.62  
 10.89 11.91 10.16 8.937 7.224 10.52 9.434 13.07 11.73 12.76 10.72 100

**C<sub>35,j</sub> where 0 ≤ j < 38:**

7.62 7.668 8.943 9.376 8.687 4.25 7.585 7.815 7.607 7.831 6.324 7.508 5.436  
 7.617 6.866 8.173 6.526 8.246 9.356 9.47 10.36 11.02 11.61 9.957 11.42  
 10.44 11 11.06 9.813 8.828 13.03 10.65 6.647 12.92 24.51 15.21 8.827  
 100

**C<sub>36,j</sub> where 0 ≤ j < 39:**

5.08 5.538 5.437 4.343 3.86 1.979 3.333 2.989 3.24 2.714 1.62 2.743 0.2707  
 5.488 4.493 2.332 2.113 3.05 3.564 3.271 5.845 4.89 3.987 3.995 4.014  
 5.236 5.009 3.438 5.14 1.527 3.401 3.229 2.581 4.046 5.59 9.52 3.219  
 6.007 100

**C<sub>37,j</sub> where 0 ≤ j < 40:**

5.825 5.916 7.322 6.715 6.812 3.321 6.186 7.611 6.048 6.139 4.953 5.942 4.385  
 6.066 5.613 6.601 6.614 7.022 8.35 7.387 7.461 7.681 9.623 7.413 8.427

7.641 8.537 7.194 6.339 5.073 7.117 6.359 7.715 6.316 7.412 6.074 43.52  
4.91 1.937 100

**C<sub>38,j</sub> where 0 ≤ j < 41:**

14.07 14.11 16.26 16.79 16.32 7.855 13.94 14.08 13.7 14.02 11.61 13.53 9.976  
13.63 12.38 14.55 11.94 15.05 16.77 17.32 19.27 20.4 21.51 18.31 21.78  
19.86 20.42 19.49 17.75 15 21.82 18.28 18.68 15.45 24.82 25.12 20.39  
38.09 11.4 11.69 100

**C<sub>39,j</sub> where 0 ≤ j < 42:**

12.71 12.73 14.52 15.08 15.03 7.346 12.66 12.89 12.3 12.73 10.38 12.12 9.008  
12.15 11.03 13.02 10.67 13.52 14.78 14.91 15.77 15.81 17.19 14.63 16.82  
15.58 16.48 15.76 13.83 12.18 16.67 14.41 16.26 14.12 13.78 12.56 13.2  
21.03 7.447 9.168 44.87 100

**C<sub>40,j</sub> where 0 ≤ j < 43:**

13.35 13.43 15.53 15.99 15.62 7.5 13.65 14.44 13.42 13.76 11.25 13.15 9.747  
13.11 12.05 14.15 11.86 14.95 17.21 17.24 18.72 17.76 19.56 16.31 18.78  
17.73 18.58 17.45 15.21 13.45 19.23 16.75 17.28 16.13 18.17 12.91 11.79  
6.297 3.395 12.26 27.56 40.74 100

APPENDIX 4: The 34x47covariance matrix obtained from IAEA Neutron Cross-Section Standards for the neutron energies 0.40 MeV and 1.69 MeV. Only the lower part of the triangular matrix is presented.  $C_{i,j}$  represents the matrix element.

**$C_{0,j}$  where  $0 \leq j < 1$ :**

100

**$C_{1,j}$  where  $0 \leq j < 2$ :**

71.01 100

**$C_{2,j}$  where  $0 \leq j < 3$ :**

39.5 47.36 100

**$C_{3,j}$  where  $0 \leq j < 4$ :**

30.79 30.44 40.4 100

**$C_{4,j}$  where  $0 \leq j < 5$ :**

24.08 24.04 25.94 46.32 100

**$C_{5,j}$  where  $0 \leq j < 6$ :**

13.03 12.95 13.81 18.01 24.86 100

**$C_{6,j}$  where  $0 \leq j < 7$ :**

20.49 20.47 22.65 24.72 48.3 22.24 100

**$C_{7,j}$  where  $0 \leq j < 8$ :**

19.15 18.85 20.84 19.54 32.38 18.71 43.75 100

**$C_{8,j}$  where  $0 \leq j < 9$ :**

21.68 21.39 23.48 22.32 26.42 15.22 43.13 40.81 100

**$C_{9,j}$  where  $0 \leq j < 10$ :**

20.8 20.56 22.68 22.71 21.76 15.17 39.45 41.62 55.18 100

**$C_{10,j}$  where  $0 \leq j < 11$ :**

17.35 17.19 19.08 18.9 15.13 11.39 23.45 25.65 35.37 45.17 100

**$C_{11,j}$  where  $0 \leq j < 12$ :**

21.55 21.16 23.29 22.83 17.85 11.57 23.3 28.33 42.56 49.08 46.97 100

**$C_{12,j}$  where  $0 \leq j < 13$ :**

14.62 14.38 16.31 16 13.29 7.884 14.96 18.86 26.66 34.28 36.06 44.66 100

**$C_{13,j}$  where  $0 \leq j < 14$ :**

22.08 21.74 23.85 22.67 18.77 10.48 19.34 23.48 34.02 38.86 33.49 55.13 35.55  
100

**$C_{14,j}$  where  $0 \leq j < 15$ :**

19.4 19.24 22.27 20.91 17.68 9.037 13.58 16.27 25.15 30.58 30.66 40.9 33.71  
50.46 100

**$C_{15,j}$  where  $0 \leq j < 16$ :**

20.45 20.21 22.69 22.26 20.17 10.27 15.63 17.02 24.23 34.26 30.69 40.31 34.16  
43.11 44.55 100

**$C_{16,j}$  where  $0 \leq j < 17$ :**

16.01 16 18.56 17.33 16.26 8.196 14.49 10.42 15.69 19.87 21.11 27.13 24.32  
28 33.08 46.91 100

**C<sub>17,j</sub> where 0 ≤ j < 18:**

20.96 20.78 23.2 22.58 21.25 11.39 19.66 16.62 16.24 21.88 24.36 29.24 25.56  
33.29 33.38 52.58 49 100

**C<sub>18,j</sub> where 0 ≤ j < 19:**

21.68 21.46 24.03 23.12 20.34 10.65 18.63 18.14 19.61 18.19 15.94 23.21 18.06  
29.42 26.48 36.82 32.15 47.6 100

**C<sub>19,j</sub> where 0 ≤ j < 20:**

21.13 20.9 23.36 22.9 20.75 10.9 18.18 18.08 19.44 19.23 15.46 17.73 11.63  
18 17.89 26.49 24.6 38.52 56.18 100

**C<sub>20,j</sub> where 0 ≤ j < 21:**

21.55 21.41 23.83 23.43 22.24 11.54 18.9 18.05 19.28 19.35 16.05 19.02 12.9  
19.49 17.03 18.5 17.54 28.73 39.32 57.05 100

**C<sub>21,j</sub> where 0 ≤ j < 22:**

19.89 19.71 22.46 22.02 20.33 10.19 17.59 17.01 18.05 18.02 15.08 18.31 12.75  
18.93 16.96 19.13 14.82 17.67 27.16 41.15 56.54 100

**C<sub>22,j</sub> where 0 ≤ j < 23:**

20.85 20.66 24.46 23.76 21.45 10.73 18.77 18.65 19.16 19.19 16.09 19.39 14.12  
19.94 19.41 20.7 17.6 21.31 20.27 28.66 40.29 56.26 100

**C<sub>23,j</sub> where 0 ≤ j < 24:**

18.09 17.9 20.77 20.26 18.42 9.489 16.21 15.88 16.77 16.69 13.87 16.77 11.88  
17.27 16.02 17.31 14.35 17.9 18.41 17.2 30.49 41.79 54.54 100

**C<sub>24,j</sub> where 0 ≤ j < 25:**

20.1 19.95 23.39 22.7 20.63 10.42 18.35 17.78 19.02 18.88 15.81 18.88 13.45  
19.08 18.12 19.43 16.4 20.24 21.57 20.3 24.72 35.53 48.64 55.97 100

**C<sub>25,j</sub> where 0 ≤ j < 26:**

19.18 19.12 21.97 21.84 20.6 10.49 17.68 17.05 18.01 17.78 15.04 17.86 12.36  
18.47 17 18.09 15.02 19.65 21.59 22 21.57 27.53 36.35 41.88 55.72  
100

**C<sub>26,j</sub> where 0 ≤ j < 27:**

20.23 20.11 23.17 22.92 20.75 10.57 17.86 17.98 18.77 18.57 15.66 18.87 13.13  
19.48 18.35 18.87 15.28 19.71 22.32 23.34 25.32 21.41 31.28 34.91 46.65  
60.33 100

**C<sub>27,j</sub> where 0 ≤ j < 28:**

18.62 18.46 21.04 21.26 19.14 9.611 16.49 16.48 17.49 17.26 14.62 17.71 12.43  
17.8 16.08 17.66 14.08 18.24 20.57 21.92 23.93 22.14 23.77 27.08 38.85  
49.15 61.98 100

**C<sub>28,j</sub> where 0 ≤ j < 29:**

17.28 17.19 19.61 20.36 20.25 9.428 17 15.95 15.86 17.11 13.54 15.64 11.21  
 16.31 15.18 17.02 13.37 18.13 18.42 19.52 22.19 22 20.93 21.85 31.88  
 44.26 49.84 56.75 100

**C<sub>29,j</sub> where 0 ≤ j < 30:**

12.17 12.12 13.83 14.83 13.44 6.607 11.62 11.56 11.84 12.15 10.22 11.87 8.863  
 11.45 10.46 12.46 10.04 12.69 13.76 14.41 15.51 15.73 15.6 15.4 19.23  
 22.31 27.86 38.11 29.73 100

**C<sub>30,j</sub> where 0 ≤ j < 44:**

9.667 9.968 11.42 11.19 10.67 5.133 9.4 9.927 9.239 9.212 7.312 8.918 5.918  
 10.08 9.101 9.531 8.194 10.29 12.02 11.75 13.33 12.56 13.77 11.65 13.55  
 13.1 13.61 12.17 11.45 8.579 12.38 10.9 11.87 10.39 12.03 9.145 8.119  
 10.56 6.673 6.962 15.54 17.22 39.12 100

**C<sub>31,j</sub> where 0 ≤ j < 45:**

10.99 11.18 13.01 13.21 12.51 6.051 11.28 12.61 11.17 11.33 9.168 10.92 7.885  
 11.35 10.39 11.86 9.75 12.29 14.42 13.55 14.23 14.16 16.41 13.21 15.14  
 14.6 15.71 14.53 13.11 10.83 14.62 12.78 14.01 12.28 14.4 11.14 10.95  
 10.76 4.417 8.172 18.6 14.93 22.76 34.57 100

**C<sub>32,j</sub> where 0 ≤ j < 46:**

8.423 8.712 9.868 9.71 9.202 4.489 8.324 9.453 8.244 8.172 6.387 7.856 5.11  
 9.066 8.099 8.218 6.876 8.806 10.47 9.778 11.11 10.99 12.76 10.18 11.35  
 11.4 12.29 10.82 10.63 7.548 10.94 9.398 10.34 9.03 10.71 8.154 9.124  
 7.886 6.538 7.369 13.89 10.68 12.57 15.28 37.46 100

**C<sub>33,j</sub> where 0 ≤ j < 47:**

9.14 9.313 10.73 10.87 10.32 5.048 9.393 10.8 9.316 9.426 7.567 9.034 6.437  
 9.508 8.641 9.719 8.012 10.15 12.08 11.23 11.91 11.96 13.97 11.18 12.73  
 12.5 13.59 12.49 11.44 9.096 12.44 10.87 12.09 10.5 12.47 9.483 10.09  
 9.439 4.228 7.915 16.07 12.78 14.88 12.01 25.04 38.21 100

APPENDIX 5: The 25x18covariance matrix obtained from IAEA Neutron Cross-Section Standards for the neutron energies 0.70 MeV and 0.96 MeV. Only the lower part of the triangular matrix is presented.  $C_{ij}$  represents the matrix element.

**$C_{0,j}$  where  $0 \leq j < 1$ :**

100

**$C_{1,j}$  where  $0 \leq j < 2$ :**

60.33 100

**$C_{2,j}$  where  $0 \leq j < 3$ :**

49.15 61.98 100

**$C_{3,j}$  where  $0 \leq j < 4$ :**

44.26 49.84 56.75 100

**$C_{4,j}$  where  $0 \leq j < 5$ :**

22.31 27.86 38.11 29.73 100

**$C_{5,j}$  where  $0 \leq j < 6$ :**

22.51 27.86 33.66 31.91 44.68 100

**$C_{6,j}$  where  $0 \leq j < 7$ :**

18.78 18.79 20.29 19.07 28.61 52.87 100

**$C_{7,j}$  where  $0 \leq j < 8$ :**

19.87 19.66 17.6 19.63 21.82 36.36 46 100

**$C_{8,j}$  where  $0 \leq j < 9$ :**

15.93 15.9 15.39 13.09 11.54 24.99 41.87 43.9 100

**$C_{9,j}$  where  $0 \leq j < 10$ :**

17.86 18.23 18.51 16.48 13.55 20.04 28.87 34.12 51.77 100

**$C_{10,j}$  where  $0 \leq j < 11$ :**

13.14 13.78 13.51 12.18 11.47 13.99 11.84 20.01 28.92 33.31 100

**$C_{11,j}$  where  $0 \leq j < 12$ :**

10.89 11.91 10.16 8.937 7.224 10.52 9.434 13.07 11.73 12.76 10.72 100

**$C_{12,j}$  where  $0 \leq j < 13$ :**

10.44 11 11.06 9.813 8.828 13.03 10.65 6.647 12.92 24.51 15.21 8.827 100

**$C_{13,j}$  where  $0 \leq j < 14$ :**

5.236 5.009 3.438 5.14 1.527 3.401 3.229 2.581 4.046 5.59 9.52 3.219 6.007  
100

**$C_{14,j}$  where  $0 \leq j < 8$ :**

19.87 19.66 17.6 19.63 21.82 36.36 46 100

**$C_{15,j}$  where  $0 \leq j < 9$ :**

15.93 15.9 15.39 13.09 11.54 24.99 41.87 43.9 100

**$C_{16,j}$  where  $0 \leq j < 10$ :**

17.86 18.23 18.51 16.48 13.55 20.04 28.87 34.12 51.77 100

**$C_{17,j}$  where  $0 \leq j < 11$ :**

13.14 13.78 13.51 12.18 11.47 13.99 11.84 20.01 28.92 33.31 100

**C<sub>18,j</sub> where 0 ≤ j < 12:**

10.89 11.91 10.16 8.937 7.224 10.52 9.434 13.07 11.73 12.76 10.72 100

**C<sub>19,j</sub> where 0 ≤ j < 13:**

10.44 11 11.06 9.813 8.828 13.03 10.65 6.647 12.92 24.51 15.21 8.827 100

**C<sub>20,j</sub> where 0 ≤ j < 14:**

5.236 5.009 3.438 5.14 1.527 3.401 3.229 2.581 4.046 5.59 9.52 3.219 6.007  
100

**C<sub>21,j</sub> where 0 ≤ j < 15:**

7.641 8.537 7.194 6.339 5.073 7.117 6.359 7.715 6.316 7.412 6.074 43.52 4.91  
1.937 100

**C<sub>22,j</sub> where 0 ≤ j < 16:**

19.86 20.42 19.49 17.75 15 21.82 18.28 18.68 15.45 24.82 25.12 20.39 38.09  
11.4 11.69 100

**C<sub>23,j</sub> where 0 ≤ j < 17:**

15.58 16.48 15.76 13.83 12.18 16.67 14.41 16.26 14.12 13.78 12.56 13.2 21.03  
7.447 9.168 44.87 100

**C<sub>24,j</sub> where 0 ≤ j < 18:**

17.73 18.58 17.45 15.21 13.45 19.23 16.75 17.28 16.13 18.17 12.91 11.79 6.297  
3.395 12.26 27.56 40.74 100



APPENDIX 6: The 18x22covariance matrix obtained from IAEA Neutron Cross-Section Standards for the neutron energies 0.70 MeV and 1.69 MeV. Only the lower part of the triangular matrix is presented.  $C_{ij}$  represents the matrix element.

**$C_{0,j}$  where  $0 \leq j < 1$ :**

100

**$C_{1,j}$  where  $0 \leq j < 2$ :**

60.33 100

**$C_{2,j}$  where  $0 \leq j < 3$ :**

49.15 61.98 100

**$C_{3,j}$  where  $0 \leq j < 4$ :**

44.26 49.84 56.75 100

**$C_{4,j}$  where  $0 \leq j < 5$ :**

22.31 27.86 38.11 29.73 100

**$C_{5,j}$  where  $0 \leq j < 6$ :**

22.51 27.86 33.66 31.91 44.68 100

**$C_{6,j}$  where  $0 \leq j < 7$ :**

18.78 18.79 20.29 19.07 28.61 52.87 100

**$C_{7,j}$  where  $0 \leq j < 8$ :**

19.87 19.66 17.6 19.63 21.82 36.36 46 100

**$C_{8,j}$  where  $0 \leq j < 9$ :**

15.93 15.9 15.39 13.09 11.54 24.99 41.87 43.9 100

**$C_{9,j}$  where  $0 \leq j < 10$ :**

17.86 18.23 18.51 16.48 13.55 20.04 28.87 34.12 51.77 100

**$C_{10,j}$  where  $0 \leq j < 11$ :**

13.14 13.78 13.51 12.18 11.47 13.99 11.84 20.01 28.92 33.31 100

**$C_{11,j}$  where  $0 \leq j < 12$ :**

10.89 11.91 10.16 8.937 7.224 10.52 9.434 13.07 11.73 12.76 10.72 100

**$C_{12,j}$  where  $0 \leq j < 13$ :**

10.44 11 11.06 9.813 8.828 13.03 10.65 6.647 12.92 24.51 15.21 8.827 100

**$C_{13,j}$  where  $0 \leq j < 14$ :**

5.236 5.009 3.438 5.14 1.527 3.401 3.229 2.581 4.046 5.59 9.52 3.219 6.007  
100

**$C_{14,j}$  where  $0 \leq j < 19$ :**

13.1 13.61 12.17 11.45 8.579 12.38 10.9 11.87 10.39 12.03 9.145 8.119 10.56  
6.673 6.962 15.54 17.22 39.12 100

**$C_{15,j}$  where  $0 \leq j < 20$ :**

14.6 15.71 14.53 13.11 10.83 14.62 12.78 14.01 12.28 14.4 11.14 10.95 10.76  
4.417 8.172 18.6 14.93 22.76 34.57 100

**$C_{16,j}$  where  $0 \leq j < 21$ :**

11.4	12.29	10.82	10.63	7.548	10.94	9.398	10.34	9.03	10.71	8.154	9.124	7.886
	6.538	7.369	13.89	10.68	12.57	15.28	37.46	100				

**C<sub>17,j</sub> where 0 ≤ j < 22:**

12.5	13.59	12.49	11.44	9.096	12.44	10.87	12.09	10.5	12.47	9.483	10.09	9.439
	4.228	7.915	16.07	12.78	14.88	12.01	25.04	38.21	100			

APPENDIX 7: The 15x15covariance matrix obtained from IAEA Neutron Cross-Section Standards for the neutron energies 0.96 MeV and 1.69 MeV. Only the lower part of the triangular matrix is presented.  $C_{ij}$  represents the matrix element.

**$C_{0,j}$  where  $0 \leq j < 1$ :**

100

**$C_{1,j}$  where  $0 \leq j < 2$ :**

43.9 100

**$C_{2,j}$  where  $0 \leq j < 3$ :**

34.12 51.77 100

**$C_{3,j}$  where  $0 \leq j < 4$ :**

20.01 28.92 33.31 100

**$C_{4,j}$  where  $0 \leq j < 5$ :**

13.07 11.73 12.76 10.72 100

**$C_{5,j}$  where  $0 \leq j < 6$ :**

6.647 12.92 24.51 15.21 8.827 100

**$C_{6,j}$  where  $0 \leq j < 7$ :**

2.581 4.046 5.59 9.52 3.219 6.007 100

**$C_{7,j}$  where  $0 \leq j < 8$ :**

7.715 6.316 7.412 6.074 43.52 4.91 1.937 100

**$C_{8,j}$  where  $0 \leq j < 9$ :**

18.68 15.45 24.82 25.12 20.39 38.09 11.4 11.69 100

**$C_{9,j}$  where  $0 \leq j < 10$ :**

16.26 14.12 13.78 12.56 13.2 21.03 7.447 9.168 44.87 100

**$C_{10,j}$  where  $0 \leq j < 11$ :**

17.28 16.13 18.17 12.91 11.79 6.297 3.395 12.26 27.56 40.74 100

**$C_{11,j}$  where  $0 \leq j < 12$ :**

11.87 10.39 12.03 9.145 8.119 10.56 6.673 6.962 15.54 17.22 39.12 100

**$C_{12,j}$  where  $0 \leq j < 13$ :**

14.01 12.28 14.4 11.14 10.95 10.76 4.417 8.172 18.6 14.93 22.76 34.57 100

**$C_{13,j}$  where  $0 \leq j < 14$ :**

10.34 9.03 10.71 8.154 9.124 7.886 6.538 7.369 13.89 10.68 12.57 15.28 37.46  
100

**$C_{14,j}$  where  $0 \leq j < 15$ :**

12.09 10.5 12.47 9.483 10.09 9.439 4.228 7.915 16.07 12.78 14.88 12.01 25.04  
38.21 100

# BIODATA

**Name** : Rebecca Lalnuntluangi

**Father's Name** : P. C. Vanlalhrauaia

**Date of Birth** : 24.02.1990

**Address** : C-3/37, Near Salvation Army Church  
ChhingaVeng, Aizawl, Mizoram; India-796009

**Educational Qualifications** :

- |                   |      |                                |
|-------------------|------|--------------------------------|
| ▪ HSLC            | 2006 | First Division                 |
| ▪ HSSLC           | 2008 | Second Division                |
| ▪ B. Sc (Physics) | 2011 | First Division (Gold Medalist) |
| ▪ M. Sc (Physics) | 2013 | First Division (Gold Medalist) |
| ▪ Pre-Ph.D Course | 2014 | 'O' Grade                      |

**Research Experience:**

- Joined the Nuclear Laboratory under the supervision of Dr. B. Lalremruata in August, 2013 and got admitted in the Department of Physics, Mizoram University as a Ph.D. Scholar in January 2014.
- Developed the neutron energy spectrum code Energy of Proton Energy of Neutron (EPEN). The code was written in C++ programming language.
- Validated EPEN using the available experimental data at different incident proton energies.
- Measurement of neutron radiative capture cross section for  $^{70}\text{Zn}(n,\gamma)^{71}\text{Zn}^m$  reaction at neutron energies 0.40 MeV and 0.70 MeV.
- Detail report on the covariance and correlation coefficients of the measured cross sections.

## Research Publications

### Referred Journals

1. **Pachua R.**, Lalremruata B., Otuka N., Hlondo L.R., Punte L.R.M., Thanga H.H., (2017), “Thick and thin target  ${}^7\text{Li}(p,n){}^7\text{Be}$  neutron spectra below the three-body break up reaction threshold”, *Nucl. Sci. Eng.*, **187**, 70-80.
2. **Pachua R.**, Lalremruata B., Otuka N., Suryanarayana S.V., Punte L.R.M., Hlondo L.R., Desai V.V., Satheesh B., Kailas S., Ganesan S., Nayak B.K., Saxena A., (2018), “Energy dependence of the neutron capture cross section on  ${}^{70}\text{Zn}$  near the inelastic scattering threshold”, *Phys. Rev. C*, **97**, 064617.
3. Punte L.R.M., Lalremruata B., Otuka N., Suryanarayana S.V., Iwamoto Y., **Pachua R.**, Satheesh B., Thanga H.H., Danu L.S., Desai V.V., Hlondo L.R., Kailas S., Ganesan S., Nayak B.K., Saxena A., (2017), “Measurements of neutron capture cross sections on  ${}^{70}\text{Zn}$  at 0.96 and 1.69 MeV”, *Phys. Rev. C*, **95**, 024619.
4. Lalremruata B., Punte L.R.M., Otuka N., **Pachua R.**, Iwamoto Y., Suryanarayana S.V., Nayak B.K., Satheesh B., Thanga H.H., Danu L.S., Desai V.V., Hlondo L.R., Ganesan S., Saxena A., (March, 2017), “Measurements of neutron capture cross sections on  ${}^{70}\text{Zn}$  at 0.96 and 1.69 MeV”, INDC(IND)-**0049**, International Atomic Energy Agency.
5. Hlondo L.R., Lalremruata B., Punte L. R. M., **Rebecca L.**, Lalnunthari J., and Thanga H.H., (2016), “A revisit to self-excited push pull vacuum tube radio frequency oscillator for ion sources and power measurements”, *Rev. Sci. Instrum.* **87**, 045101.

## Conference Proceedings

1. **Pachua R.**, Lalremruata B., Otuka N., Hlondo L.R., Punte L.R.M., Thanga H.H., (2017), “A tool for calculation of  ${}^7\text{Li}(p, n){}^7\text{Be}$  neutron source spectra below the three body break-up reaction threshold”, *Proceedings of the DAE-BRNS Symp. on Nucl. Phys*, **61**, 430-431.
2. **Pachua R.**, Lalremruata B., Otuka N., Hlondo L.R., Punte L.R.M., and Thanga H.H., (2016), “A tool for calculation of  ${}^7\text{Li}(p, n){}^7\text{Be}$  neutron source spectra below the three body break-up reaction threshold”, *EPJ Web of Conferences* **146**, 12016-12019.
3. Oral presentation at National Workshop on Error Propagation in Nuclear Reaction Data Measurement-2017 (EPNRDM-2017), MZU, Aizawl, 13<sup>th</sup> – 14<sup>th</sup> March, 2017.

## **Conferences/Workshops/Seminar Attended**

1. Sixth DAE-BRNS Workshop cum Theme meeting on EXFOR compilation, Bangalore University, Bangalore, *20<sup>th</sup> - 24<sup>th</sup> January, 2015.*
2. International Conference on Nuclear Data for Science and Technology, Brugges, Belgium, *11<sup>th</sup> - 16<sup>th</sup> September, 2016.*
3. NDPCI-BRNS School on Nuclear Reactions and Measurements, BARC, *Mumbai, 2<sup>nd</sup> - 11<sup>th</sup> November, 2016.*
4. 61<sup>st</sup> DAE Symposium on Nuclear Physics, SINP, Kolkata, *5<sup>th</sup> - 9<sup>th</sup> December, 2016.*
5. 7th DAE-BRNS Workshop on Compilation of Experimental Nuclear Data (EXFOR-2017), NEHU, Shillong, *6<sup>th</sup> - 10<sup>th</sup> March, 2017.*
6. Two days National Workshop on Error Propagation in Nuclear Reaction Data Measurement, Mizoram University, Aizawl, *13<sup>th</sup> - 14<sup>th</sup> March, 2017.*